OUKA
The University of Osaka
Institutional Knowledge Archive

Title	Resonance Raman Studies on Structure of Novel Rhodopsins
Author(s)	大友, 章裕
Citation	大阪大学, 2019, 博士論文
Version Type	VoR
URL	https://doi.org/10.18910/73516
rights	
Note	

The University of Osaka Institutional Knowledge Archive : OUKA

https://ir.library.osaka-u.ac.jp/

The University of Osaka

Resonance Raman Studies on Structure of Novel Rhodopsins

共鳴ラマン分光法による新規ロドプシンの構造化学研究

Akihiro OTOMO

Department of Chemistry, Graduate School of Science,
Osaka University

Aug. 2019

CONTENTS

CHAPTER 1. Introduction

Living organisms utilize sunlight as a source of energy conversion or signal transduction to adapt the environmental changes. Representative examples of life phenomena using light are photosynthesis in plants and vision in animals. Such light-responsive biological phenomena usually occur via “Photoreceptor proteins”. A schematic view of various functions by photoreceptor proteins are shown in Figure 1-1. Photoreceptor proteins generally consist of protein moiety and the prosthetic group as a chromophore, which can respond to light through any photochemical reactions. This response of chromophores associated with light absorption drives global conformational changes of protein structure, then photoreceptor proteins turn the active (inactive) state from the inactive (active) state. Since the function of photoreceptor proteins can be switched by light, they have been the targets of studies for elucidation the relationship between protein structure and function.

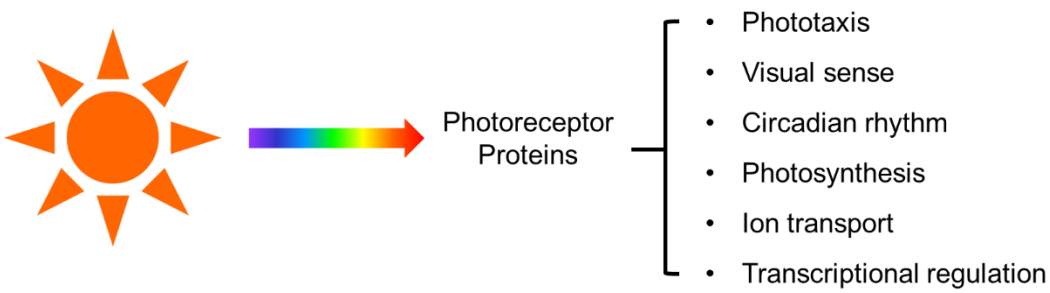

Figure 1-1. Conceptual diagram of various life phenomena using sunlight by photoreceptor proteins.

"Rhodopsin" is one of the most abundant photoreceptor proteins in the world. They are discovered not only in animals but also in archaea, bacteria, and eukarya and categorized into three types; microbial rhodopsins (type-1), animal rhodopsins (type-2), and heliorhodopsins (type-3) as shown in Figure 1-2. All types of rhodopsins possess a retinal molecule as a chromophore in common inside a protein moiety composed of a heptahelical transmembrane motif called "opsin". The retinal chromophore is covalently bound to the lysine residue of the opsin forming Schiff base (retinal Schiff base, RSB). When the chromophore absorbs light, it shows the photoisomerization in a sub-picosecond time scale. Due to the retinal chromophore is well packed by bulky amino acid residues, the photoisomerization induces a sequence of protein structural changes, which generate some biological functions such as ion transport, phototaxis, signal transduction, and more. The abstruse functional mechanisms of rhodopsins, where photoisomerization of retinal chromophore generate various functions as a common trigger, keeps fascinating researchers in diverse fields.

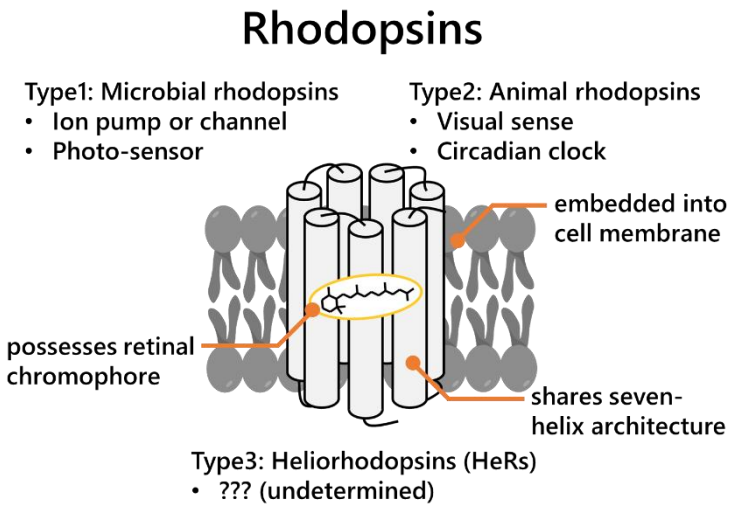

Figure 1-2. Diagram of rhodopsins. Rhodopsins have common features, that is, they are embedded into the cell membrane, possess the retinal molecule as a chromophore, and share the seven α-helical transmembrane architecture. The representative functions of each type of rhodopsin are described.

This chapter describes the general properties of microbial rhodopsins at first. I will then briefly explain the fundamental nature of other rhodopsins, animal rhodopsins, and heliorhodopsins. Next, I will describe the targeted proteins in detail. After that, the principle of resonance Raman spectroscopy used in this study and some marker bands will be described. Finally, I will state the aims of this theses. In this thesis, "rhodopsin(s)" basically refers to microbial rhodopsin.

1.1. Microbial Rhodopsins

Among microbial rhodopsins, bacteriorhodopsin (BR) was first discovered from the purple membrane of *Halobacterium halobium* in 1971.[1] BR functions as a light-driven outward proton pump to generate the electrochemical proton gradient across the cell membrane, which is used for the energy source of ATP synthase.[2, 3] Not only BR has been studied in detail for its ion transport mechanisms, but it has also played important roles as a model for membrane protein researches. The development of BR research has always been with the development of physicochemical methods of membrane proteins such as crystal structure analysis and folding study.[4-7]

The fundamental properties of BR have been almost established since it was discovered. BR exists in a stable dark-adapted form with the absorption maximum wavelength (λ_{max}) at 548 nm (BR_{548}) and a metastable light-adapted form with λ_{max} at 568 nm (BR_{568}).[8] They are able to convert by light or thermal energy. The geometric conformation of the retinal chromophore of BR_{548} and BR_{568} is 13-*cis*/15-*syn* and all-*trans*/15-*anti*, respectively as shown in Figure 1-3. Absorption of a photon by the retinal chromophore in BR_{568} induces the cyclic photochemical reaction followed by thermal processes through some photointermediates, K, L, M, N, and O, which is the name of retinal chromophore in each photointermediate. This series reaction is called "photocycle" and takes about ten milliseconds until complete. During the photocycle, BR actively

transports proton across the cell membrane.

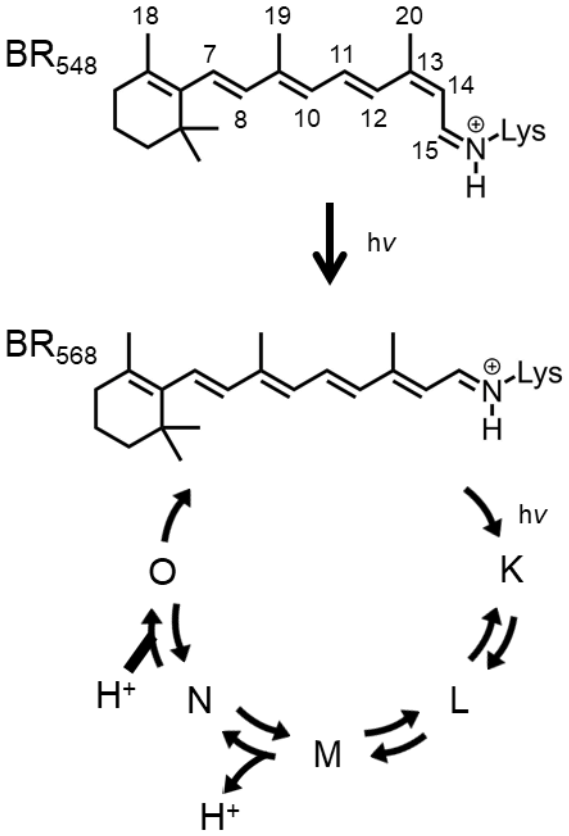

Figure 1-3. Configurations and atom numbering of the chromophore of BR_{548} and BR_{568}. BR_{548} has a 11-*cis*/15-*syn* retinal and BR_{568} has an all-*trans*/15-*anti* retinal. BR_{568} shows a series of cyclic reaction through some photointermediates, K, L, M, N, and O, which is the name of retinal chromophore in each photointermediate.

The unidirectional proton transport in BR is generally described by the Grotthuss mechanism that utilizes several charged amino acid residues and water molecules.[9] Briefly, proton transfers from the protonated Schiff base to the proton acceptor Asp85. Then, a proton is released to the extracellular fluid from the proton-releasing group at the extracellular side. In the N intermediate, the Schiff base is reprotonated from the proton donor Asp96. And then, reprotonation of Asp96 from the cytoplasmic fluid occur. Finally, proton transfers from Asp85 to the proton-releasing group. The p*K*a value of the amino acid residues is artfully adjusted by the protein conformational change to achieve unidirectional proton transport. Figure 1-4 represents the proton pathway. From the above, the retinal Schiff base (RSB) plays an important role in proton transport.

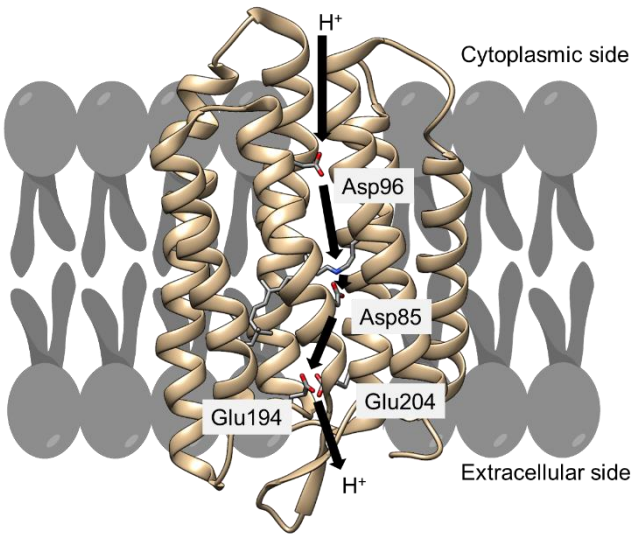

Figure 1-4. Proton transport pathway in BR. Asp85 and Asp96 is proton acceptor and proton donor, respectively. Glu194 and Glu204 form the proton-release group. PDB: 1fbb.

Following the discovery of BR, halorhodopsin (HR, light-driven inward chloride ion pump) in 1977,[10] sensory rhodopsin I (SRI, both attractant and repellent phototaxis sensor) in 1982,[11] and sensory rhodopsin II (SRII, repellent phototaxis sensor) in 1985,[12] were discovered. The photocycle of SRI and SRII is several orders of magnitude slower than that of ion-pumping rhodopsins, suggesting that a long-lived photoproduct can efficiently activate their signal transducers, which finally control the rotary direction of the flagella. Anyway, it is noteworthy that all of these different functions are driven by the photoisomerization of the retinal chromophore and the resulting changes in protein structure as shown in Figure 1-5.

The diversity of microbial rhodopsin has been further demonstrated by advances in genomic science. Starting with proteorhodopsin (PR) being first discovered in marine eubacteria, it has been reported that rhodopsin exists in various organisms.[13-15] The advances in genomic science also led to the discovery of light-driven ion channelrhodopsin, opened a new way of the applicability of microbial rhodopsins to optogenetics.[16-18] Furthermore, very recently, rhodopsin having new functions that could not be considered in the conventional sense, such as an outward sodium ion pump,[19] an inward proton pump,[20] and enzymatic rhodopsin,[21] has discovered. These facts imply that living organisms are utilizing sunlight in more diverse ways than previously considered.

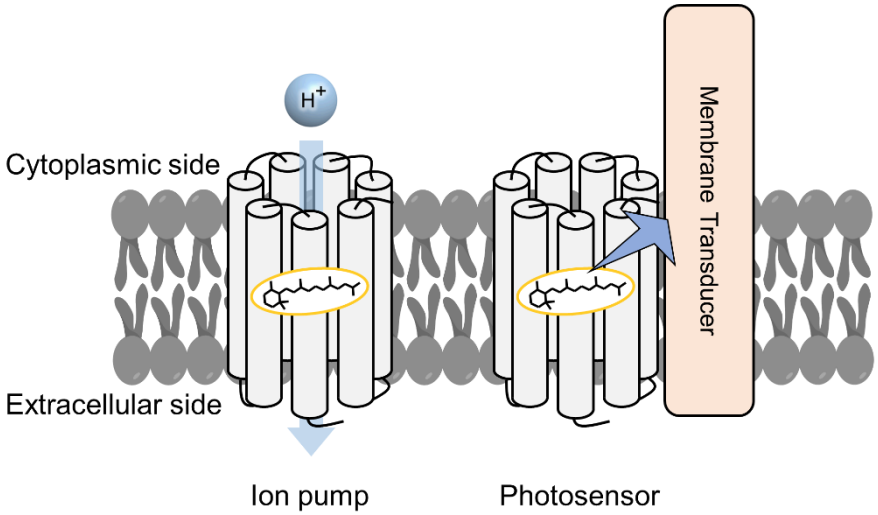

Figure 1-5. Schematic representation of the rhodopsins function as an ion pump and photosensor.

The molecular mechanisms of microbial rhodopsins have been investigated in detail, focusing on BR. However, with regard to the light-driven ion pump performed by microbial rhodopsin, there still remain challenging issues in molecular science. That is, microbial rhodopsins can selectively transport various types of ions, with the photoisomerization of retinal chromophores as a common trigger. Also, although photoisomerization is just a trigger of function and the essence of ion transport function is a structural change of protein moiety, there is no research which systematically revealed the structural change of protein moiety. These matters will be described in detail later.

1.2. Other Rhodopsins

In this section, we describe animal rhodopsin, mainly involved in vision, and recently newly discovered heliorhodopsins, focusing on differences from microbial rhodopsins.

1.2.1. Animal Rhodopsins

Animal rhodopsins have a longer history of research than microbial rhodopsins. Just as microbial rhodopsins exhibit diverse functions such as ion pumps, ion channels, or signal transduction, animal rhodopsins also exhibit diverse functions such as vision, circadian rhythm, body-color change, and more.[22, 23] The schematic diagram is shown in Figure 1-6. On the other hand, the configuration of the retinal chromophore between them is different. In animal rhodopsins, 11-*cis*/15-*anti* retinal is embedded into the opsin as an unphotolyzed state and when this chromophore absorbs a photon it isomerized to all-*trans*/15-*anti*. The crystal structure of the representative animal rhodopsin, bovine rhodopsin is shown in Figure 1-7. They then go through several intermediates containing functional states interact with guanine nucleotide-binding proteins, G protein or arrestins. Therefore, the animal rhodopsins are categorized to G protein-coupled receptors (GPCRs).

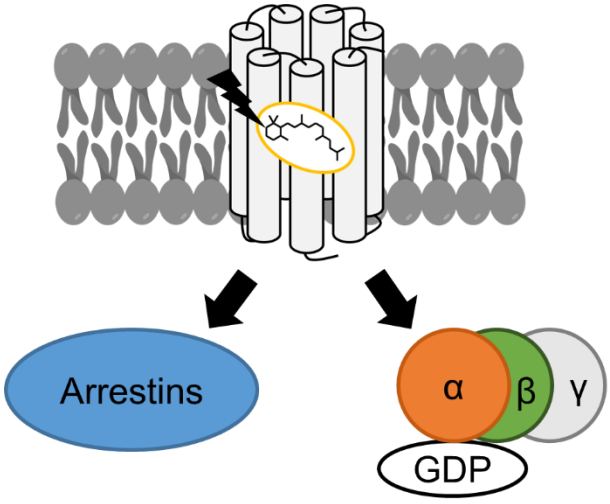

Figure 1-6. Schematic diagram of the function of animal rhodopsin. It activates the arrestins or G-proteins by light irradiation.

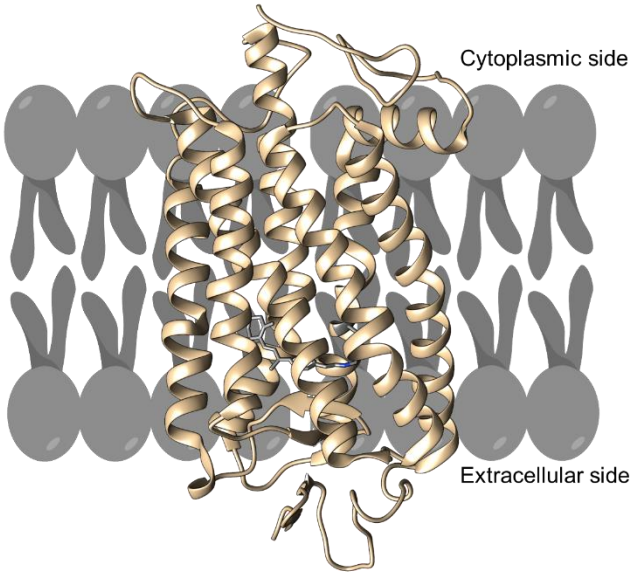

Figure 1-7. Crystal structure of bovine rhodopsin. PDB: 1U19.

The reaction pathway of typical animal rhodopsin, bovine rhodopsin, is shown in Figure 1-8.[9, 24] Importantly, after interacting with G protein in Meta II state, animal rhodopsins release the retinal chromophore in contrast to microbial rhodopsins where the retinal chromophore demonstrates the photocycle. The released all-*trans* retinal is then recombined with *apo*-opsin through reduction to the 11-*cis* retinol and then oxidation to 11-*cis* retinal via some oxidoreductase. This a series of reaction is called rhodopsin regeneration.[24, 25] Thus, the retinal molecule can be considered as an inverse agonist or an agonist. As shown above, the functional mechanisms among microbial rhodopsins and animal rhodopsins differ in some aspects, despite their primitive reaction trigger is the photoisomerization of the retinal chromophore and they share a similar protein secondary structure. The similarity of amino acids sequence among microbial rhodopsins and animal rhodopsins is quite low. Although it is not certain whether microbial rhodopsins and animal rhodopsins have a common ancestry, the general view is that they have undergone different evolutions.[9]

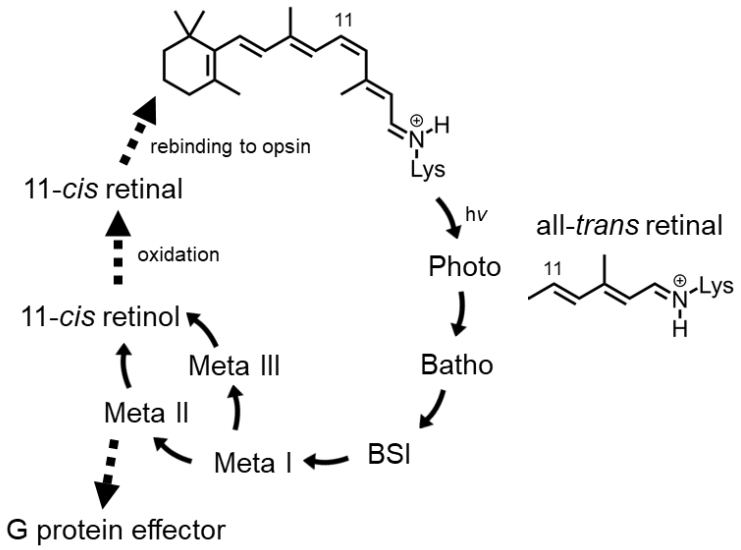

Figure 1-8. Configurations of the retinal chromophore in bovine rhodopsins. In the dark state, the chromophore forms 11-cis/15-anti retinal. When it absorbs a photon, the photoisomerization from 11-cis/15-anti to all-trans/15-anti occurs. The photoactivated bovine rhodopsin shows the photocycle. Unlike the photocycle of microbial rhodopsins, animal rhodopsins require to be mediated by oxidoreductase, etc. in order to return to the original state.

1.2.2. Heliorhodopsions

Rhodopsins are currently classified into the two distinct types as I mentioned above, namely microbial rhodopsin (type-1) and animal rhodopsin (type-2), for about half a century since the study of rhodopsin began. However, Pushkarev et al. conducted a comprehensive genetic analysis of microorganisms inhabiting Galilee Lake in Israel, and discovered a new family of rhodopsin different from type-1 and -2, named "Heliorhodopsin" (HeR) in 2018.[26] These newly discovered rhodopsins have a distinctly different amino acid sequence from any other type of rhodopsins demonstrated lower identity less than 15%. They are abundant and distributed globally, detected in archaea, bacteria, eukarya and even in viruses. The structural and functional features of the revealed HeRs are as follows; (1) the orientation of HeRs in the cell membrane is opposite to that of microbial rhodopsins or animal rhodopsins, with the N-terminus facing the cell cytoplasm as shown in Figure 1-9. (2) HeRs have all-*trans* retinal in the dark, which isomerized to 13-*cis* retinal by absorption of a photon. (3) HeRs have no ion-transport activity upon light illumination. (4) HeRs show photocycle longer than 1 second. In particular, feature 3 and 4 suggest that HeRs function as a photosensor transmits intracellular signal. However, the signal transducer like a HrtI for SRI or HrtII for SR2 has not been found in the gene encodes heliorhodopsin, therefore, further investigations are required for determination of the HeRs function.

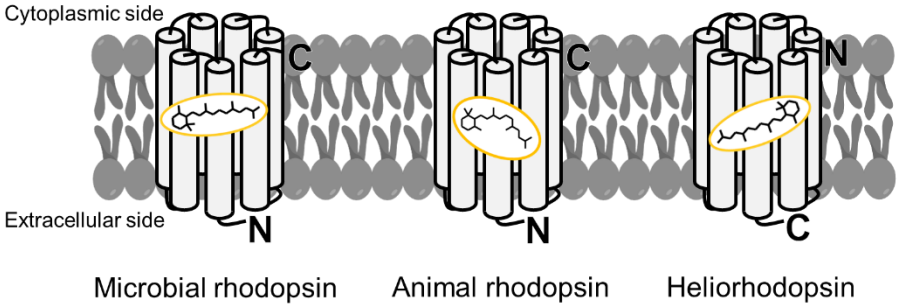

Figure 1-9. Schematic representation of the structures of three types rhodopsins. Microbial rhodopsin and animal rhodopsin are embedded in the cell membrane so that the N terminus is on the extracellular side and the C terminus is on the cytoplasmic side, but in the case of heliorhodopsin, the directions are reversed.

1.3. Target Proteins of This Thesis

As we have seen in the previous section, an enormous number of rhodopsins regardless of type1, 2, and 3 have been discovered with the recent remarkable development of genome science. In the continuous growing of the rhodopsin study, understanding the general molecular mechanism of rhodopsins is significantly important. Namely, it is required to investigate what kind of protein structural change, which is induced by a common reaction trigger, results in the functional divergence of rhodopsins. Additionally, it is also important to predict the function of rhodopsins whose function is unknown from the molecular properties of the fine structural environments of the retinal chromophore or protein moiety that are hidden in similar structures. In this study, to clarify the mechanism of the functional determination in ion pump rhodopsins and the chromophore structure of the novel rhodopsin, we used KR2 and Heliorhodopsins from two species. The following will describe the basic properties of the rhodopsins targeted in this thesis based on previous studies.

1.3.1. Basic Properties of *Krokinobacter* Rhodopsin 2

In 2013, newly microbial rhodopsins were discovered from marine flavobacterium, *Krokinobacter eikastus* by Inoue et al.[19] They were named to KR1 and KR2. The functional analysis revealed that KR1 and KR2 works as light-driven an outward proton pump and an outward sodium ion pump, respectively. The discovery of KR2 has excited the rhodopsin research, as it was thought that there were no light-driven cation pumps other than proton pump. The reason why is, in order to transport cations in rhodopsin, the electrostatic repulsion arises between the protonated Schiff base and the transport cations. Another significant feature of KR2 is that the function is switched depending on the coexisting cation species. Namely, KR2 acts as a sodium ion pump in the presence of a sufficient sodium ion but works as a proton pump in the presence of larger monovalent cations, such as potassium ion, rubidium ion, and cesium ion instead of

sodium ion.[19] KR2 has been energetically studied since its discovery due to its seemingly incomprehensible sodium ion transport function and functional conversion ability.[18]

Structural Fatures of KR2

The crystal structure of KR2 was reported by two distinct groups in 2015.[27, 28] KR2 possesses the retinal chromophore surrounded by tightly packed seven-transmembrane α-helices, named A – G helix, embedded into the cell membrane. The structural features of KR2 revealed by the crystallographic studies are shown below. (1) There are no ion binding sites inside the protein unlike the HR, possesses a chloride ion binding site at the protonated Schiff base. On the other hand, the sodium ion binding site is identified on the surface of the extracellular side.[27, 29] This binding sodium ion is thought to not be necessary for its sodium ion transport function but mainly plays a role to stabilize the protein structure.[28] The ion binding site is composed of Tyr25 side chain and Thr83 and Phe86 backbone oxygen of one protomer and Asp102 side chain provided from the neighbor protomer.[27] A crystal structure of KR2 and its binding site are shown in Figure 1-10. (2) KR2 forms pentameric structure in the neutrality condition and sufficiently in the presence of sodium ion.[27, 30] At each subunit interface, the sodium ion binding site mentioned above is located (Fig. 1-10 (B)). Later, it was directly observed that KR2 formed a pentameric structure in the lipid bilayer using the high-speed AFM experiment and CD spectroscopy.[31] However, because these experiments were conducted under conditions where KR2 was expressed in *E. coli.* or artificial lipid bilayer, it has not been clear whether KR2 keeps the pentameric structure or not under the physiological environment. (3) The ion pump rhodopsins can often be classified by three amino acid residues in helix C which play a crucial role in ion-transport, called "motif". KR2 was classified as NDQ motif implies that Asn112, Asp116, and Gln123 are involved in the sodium ion transport.[32] Especially, Asp116 is very important in understanding the ion transport mechanism of KR2 so that it acts as a counterion and the proton donor of the protonated

Schiff base. Kato et al. proposed a sodium ion transport mechanism avoiding the electrostatic repulsion between the protonated Schiff base and sodium ion based on the crystal structure which was crystallized by soaking an acidic buffer.[28] First, after the photoisomerization of the retinal chromophore, proton transfer occurs from the protonated Schiff base to Asp116 in the K-to-M transition. Then, protonated Asp116 flips away from the Schiff base, reduces the electrostatic repulsion so that sodium ion can transport across the Schiff base. After that, the direction of Asp116 returns to the original state, preventing the backward of sodium ion in O intermediate. Finally, the proton returns to the Schiff base. However, as this reaction model was established based on the static and under the undesirable pH condition, the direct observation of the protein structural changes using time-resolved spectroscopy in solution should be conducted for understanding the sodium ion transport mechanism.

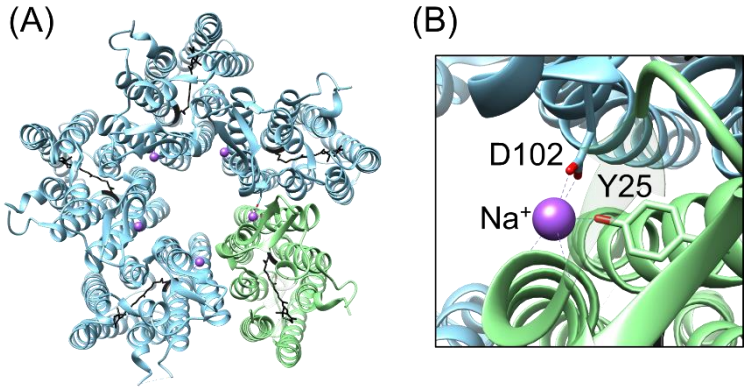

Figure 1-10. Crystallographic structure of KR2 (PDB: 4XTN). (A) Pentameric structure of KR2 viewed from the extracellular side. The light green chain represents one protomer and the cyan chains represent the other four protomers. The black sticks and purple spheres show the retinal chromophore and sodium ion, respectively. (B) Expanded view of the sodium ion binding site of KR2. Tyr25 and Asp102 constitute the binding site and are provided from two protomers adjacent to each other.

Ion Selectivity in KR2

In contrast to the elucidation of the sodium ion transport mechanism in KR2, the mechanism of the functional conversion of KR2 has been little known. Kato et al. examined the kinetics of the M and O intermediate under the wide range of sodium ion and proton concentration to understand the ion selectivity of KR2.[33] They revealed that the kinetics of proton uptake was much larger than that of sodium ion uptake and KR2 pumps proton in the environment where the proton and sodium ion concentrations are similar. These results indicated that KR2 competes for the proton-pumping and sodium ion-pumping state and it works as a sodium ion pump in the physiological environment where the proton is much less than sodium ion.[33] However, it cannot be explained how KR2 recognize the transport ion. The mechanisms of ion recognition in KR2 has been controversial. In the first paper of KR2, the authors concluded that the chromophore structure was independent on the cation species because the absorption properties did not change among in the presence of different monovalent cations.[19] Ono et al. showed that the early photointermediate structure was the almost same between in the presence of sodium ion and potassium ion using the low-temperature difference FTIR spectroscopy.[34] Hontani et al. also demonstrated that the structural changes in the retinal chromophore were largely unaffected by transport ion using femto- to submillisecond stimulated Raman spectroscopy.[35] On the other hand, in 2015, de Sliva et al. demonstrated the cation-dependent conformational change in KR2 using EPR spin-spin dipolar coupling.[36] In their model, the helix F and G move when sodium ion replaces to potassium ion in the unphotolyzed state with the shift of absorption maximum wavelength.[19] The solid-state NMR study demonstrated that the structure of the retinal Schiff base differs between in the presence of 100 mM of sodium ion and potassium ion, rubidium ion, and cesium ion.[37] This could be explained the long-distance conformational change between the retinal Schiff base and the ion binding site.[37, 38] The relationship between the function and the

retinal Schiff base structure was also examined by ultrafast spectroscopy. Tahara et al. demonstrated the efficiency of the isomerization of the retinal chromophore relates to the protonation state of Asp116, which is the counter ion of the protonated Schiff base.[39] Further studies are needed in order to investigate the relationship between the structure of ion binding site and the structure of the retinal chromophore.

Artificial rhodopsins with various functions have been designed on the basis of KR2. Inoue et al. found that the H30A mutant transports only sodium ion.[19] Recent solid-state NMR studies revealed that His30, locates on the subunit interface affects the interaction between the Schiff base and Asp116.[37, 38] The light-induced potassium ion pump and cesium ion pump were created by introducing the mutation at the cytoplasmic surface.[27, 28, 40] The hydrogen-bonding network in the cytoplasmic region, which includes Gln123, Lys255, and internal water molecules.[41] Since Lys255 forms the Schiff base with the retinal molecule, these results suggested that the selectivity of the transporting ion is related to the structure of the chromophore. Furthermore, the functional conversion by amino acid replacement other than at the cytoplasmic side has also been reported. The motif-based mutagenesis (NTQ/F72G/D102N) in KR2 enables the functional conversion from outward sodium ion pump to inward chloride ion pump.[42] KR2 converts to the light-induced potassium ion channel by the introduction of the R109Q mutation.[43] As we have seen above, KR2 can convert its function with minor mutations. These facts may suggest that KR2 has a flexible structure for the transport of various ions.

Here, I have described the previous functional/structural studies of KR2. However, the comprehensive understanding has not been achieved what structural properties determine the function of KR2. To reveal the functional determinants of KR2, further studies are needed to investigate the structural relationship between the ion binding site and the retinal chromophore of KR2.

Protein Dynamics of KR2 During Ion Transport

In order to elucidate the mechanism of ion transport in KR2, it is important to observe the protein structural changes during the function. KR2, like other ion-pumping rhodopsins, shows the photocycle after photoisomerization of the retinal chromophore as shown in Figure 1-11.[19] Because KR2 does not possess the sodium ion binding site other than that at the extracellular side, the uptake of sodium ion should occur during the photocycle. The sodium ion concentration dependence on the kinetics of each photointermediate and simulation study suggested that the ion-uptake occurs in the decay of the M intermediate, where proton transfers from the Schiff base to Asp116, and the ion-release events in the decay of the O intermediate, respectively.[19, 33, 44] The chromophore structure of each photointermediate was studied using resonance Raman spectroscopy.[45, 46] The results indicate the importance of the hydrogen bond strength between the Schiff base and its counterion, Asp116, and the distortion of the polyene chain of the chromophore. The structural changes of the chromophore were also investigated by the time-resolved FTIR spectroscopy.[47, 48] These results using time-resolved spectroscopy could explain the structural changes around the retinal chromophore that have already been proposed by the crystallographic studies. [18, 28]

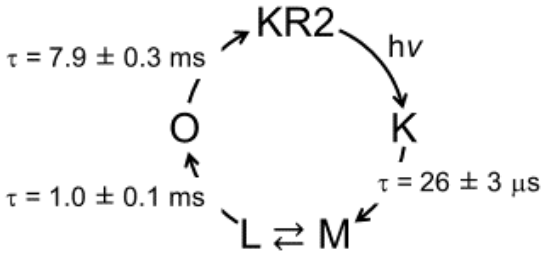

Figure 1-11. Photocycle of KR2 during sodium ion transport. The time constant of each photointermediate was estimated by flash photolysis experiments.

In contrast, the structural changes of the protein moiety during ion transport have been less understood. The NMR and IR studies can provide the structural information of KR2 but the assignments of the amino acid residues are difficult.[38, 47] Therefore, the selective observation of the protein structure is an urgent challenging to elucidate the molecular mechanisms of ion transport in KR2.

1.3.2. Basic Properties of Heliorhodopsins

Heliorhodopsins are a new category of rhodopsins discovered in 2018.[26] Some of the structural features are similar to microbial rhodopsin i.e. they have an all-*trans* retinal as a chromophore in the dark, which is isomerized to 13-*cis* by light illumination and they share a heptahelical transmembrane structure. Even though several experimental results suggest that HeRs function as not an ion pump but a photosensor as we have seen in 1.2.2., at this point, little is known about the structural and functional properties of HeRs. Transient absorption spectroscopy revealed the longer photocycle of HeRs.[26] During the photocycle, proton transfer from the Schiff base to a proton-accepting group composed of His23 and His80 in K-to-M transition without release out from the protein.[26] Singh et al. applied Ala scanning to HeR 48C12 and demonstrated the importance of His80 for the absorption shift.[49] The ultrafast absorption spectroscopy demonstrated the kinetics of the photoisomerization in HeRs were the almost same that of microbial rhodopsins.[50] Recently, HeR was also discovered from gram-negative eubacterium and its characteristics were investigated, but the function has not been elucidated yet.[51]

Research on Heliorhodopsin is just beginning. Under such circumstances, it is important to compare the chromophore structure of HeRs with that of microbial rhodopsins because they exhibit various functions, as we have seen above.

1.4. Raman Spectroscopy

I conducted resonance Raman spectroscopy to investigate the chromophore and protein structure of KR2 and HeRs. This method is a powerful tool for investigating the protein structure because of the selective observation enabled by the resonance effects. This section will describe the principle of resonance Raman spectroscopy and the useful marker bands for studying the rhodopsins.

1.4.1. Principle of Resonance Raman Spectroscopy

Raman Scattering

When the molecule is irradiated by an intense laser beam in the UV-visible region (ν_0), there are two types of scattered light. One, called Rayleigh scattering, has the same frequency as the incident beam (ν_0). The other, called Raman scattering, has frequencies $\nu_0 - \nu_m$ (Stokes) and $\nu_0 + \nu_m$ (anti-Stokes), where ν_m is a vibrational frequency of the molecule. Therefore, the vibrational frequency of the molecule is obtained as a shift from the incident beam frequency. The energy diagram is shown in Figure 1-12.

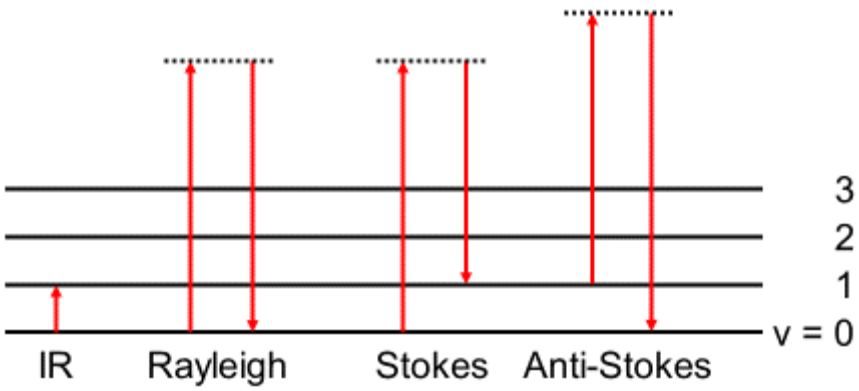

Figure 1-12. Schematic energy diagram of IR, Rayleigh, and Raman scattering. The dotted line represents the virtual state.

In the classical theory, an electric dipole moment P is derived from the electric field strength of the light source (E), the nuclear displacement (q), and the polarizability of the molecule, which is the 2nd rank tensor.

$$P = \alpha_0 E_0 \cos 2\pi\nu_0 t + \frac{1}{2}\left(\frac{\partial\alpha}{\partial q}\right) q_0 E_0 [\cos\{2\pi(\nu_0 + \nu_m)t\} + \cos\{2\pi(\nu_0 - \nu_m)t\}]$$

As we can see this equation, to be Raman-active, $(\partial\alpha/\partial q)$ must not be zero. It means the rate of change of polarizability with the vibration must be nonzero. On the other hand, the Rayleigh scattering always occurs.

Resonance Raman Scattering

When the molecule in the vibrational state m is exited to the virtual state and then relax to a vibrational state n, the resonance Raman scattering intensity I can be described as follows,

$$I = \text{constant} \cdot (\nu_0 - \nu_{mn})^4 \cdot I_0 \sum_{\rho\sigma} \left|(\alpha_{\rho\sigma})_{mn}\right|^2$$

where $(\alpha_{\rho\sigma})_{mn}$ represents the change in polarizability tensor. This can be described by the Kramer–Heisenberg–Dirac (KHD) dispersion formula as follows,

$$(\alpha_{\rho\sigma})_{mn} = {}^1/_h \sum_e \left(\frac{M_{me}M_{en}}{\nu_{mn} - \nu_0 + i\Gamma_e} + \frac{M_{me}M_{en}}{\nu_{mn} + \nu_0 + i\Gamma_e}\right)$$

where ν_{em} and ν_{en} represent the frequencies corresponding to the energy differences between the initial and virtual state and virtual and final state, respectively and h is Planck's constant. M_{me} and M_{en} are the electric transition moments,

$$M_{me} = \int \Psi_m^* \mu_\sigma \Psi_e d\tau$$

$$M_{en} = \int \Psi_e^* \mu_\sigma \Psi_n d\tau$$

where μ_σ is the σ component of the electric dipole moment. Γ_e is the bandwidth and the $i\Gamma_e$ is called the damping factor. As we can see the KHD dispersion formula, there is a resonance term $(\nu_{mn} - \nu_0)$ in the denominator. Namely, when the incident beam frequency is close to the energy

of the electric transition, the Raman scattering will be enhanced by a factor of 10^4 to 10^6. This phenomenon is called resonance Raman scattering.

By taking advantage of resonance Raman scattering, the selective observation of the particular chromophore molecules becomes possible. Figure 1-13 shows the absorption spectrum of KR2. The absorbance peak at the visible region and the UV region is due to the retinal chromophore and the aromatic amino acid residues, such as tryptophan (Trp), tyrosine (Tyr) and phenylalanine (Phe), respectively. In this study, 532 nm and 233 nm laser was used for obtaining the resonance Raman spectra of the retinal chromophore and Trp and Tyr residues, respectively.

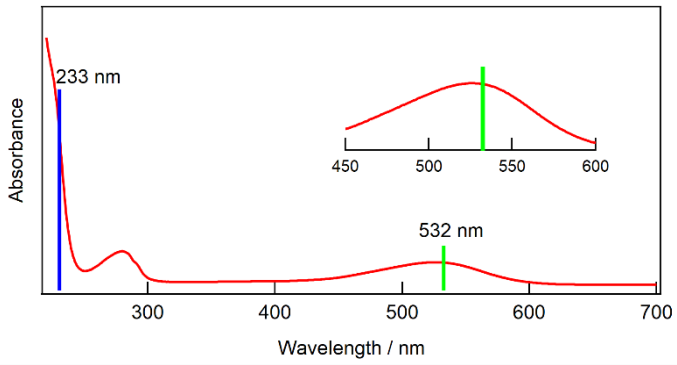

Figure 1-13. Absorption spectrum of KR2 measured at 220 – 700 nm. Inset represent the enlarged view at 450 – 600 nm. The green and blue line represents the wavelength of the laser used.

1.4.2. Marker Bands of Retinal Chromophore

Since Resonance Raman spectroscopy is a powerful tool for studying the chromoprotein structure, there are many examples of the application of resonance Raman spectroscopy to the retinal chromophore in rhodopsins. In this section, I will describe some Raman bands that can be marker bands in order to discuss the structure of the retinal chromophore. Figure 1-14 shows a 532-nm excited resonance Raman spectrum of the retinal chromophore in KR2.

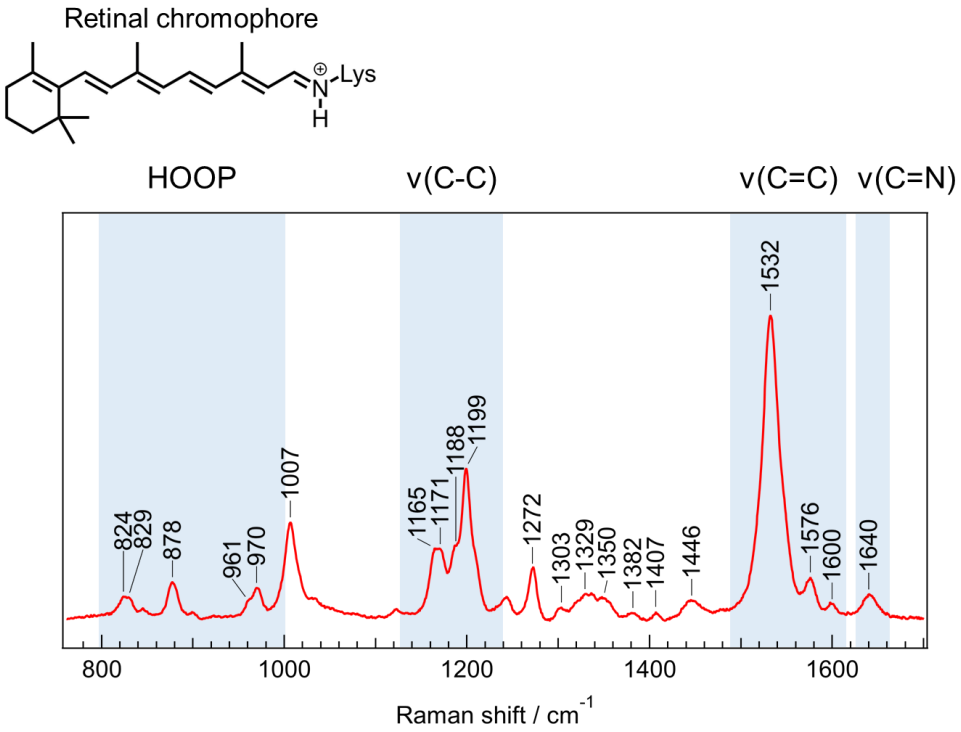

Figure 1-14. RR spectrum of KR2. The blue regions represent the marker bands; hydrogen out-of-plane (HOOP), C-C stretching mode (v(C-C)), C=C stretching mode (v(C=C)), C=N stretching mode (v(C=N)). The assignments of these marker bands were based on the detailed analysis in BR.

Hydrogen out-of-plane (HOOP)

The band observed at 800-1000 cm^{-1} is assigned to the hydrogen out-of-plane bending vibration (HOOP) mode. Since the intensity of a resonance Raman transition depends on Franck-Condon factors, the local HOOP modes will be enhanced when the displacement of chain hydrogen out of the plane occurs between the ground state and the excited state. Thus, the resonance enhancement of HOOP modes could be achieved by the distortion of the polyene chain of the retinal chromophore. [52, 53]

C-C stretching mode (ν(C-C))

Based on the experiment using the isotopic label of ^2H, it was found that C-C stretching vibration modes are strongly coupled with the CCH in-plane rocking mode.[53, 54] These coupled vibration modes are observed at 1100-1300 cm^{-1} and known to useful for considering the configuration of the retinal chromophore. Furthermore, because the C_{14}-C_{15} stretching vibration mode is coupled with the N-H rocking mode, this deuteration shift of this band can be used to determine the configuration of the C=N bond in Schiff base.[8, 54]

C=C stretching mode (ν(C=C))

The C=C stretching vibration modes are observed in the 1500-1600 cm^{-1} region. Due to the energy coupling of the individual C=C stretching, they are mixed in the normal mode.[53] Therefore, the strongest peak at 1532 nm in Figure 1-9 contains totally three kinds of C=C stretching modes. Since the intensity of ν(C=C) bands is related to the bond length, it can be used the change of geometry of the retinal chromophore upon excitation.[53] The frequency of these bands directly reflects the bond order of each C=C double bond so that it can be provided information about the localization of the conjugated π electron.[53, 55, 56] Consequently, the ν(C=C) frequency shows the inverse relationship with the absorbance maximum wavelength.

C=N stretching mode (ν(C=N))

The band appearing around 1640 cm^{-1} is derived from the C=N stretching vibrational mode. This band can be a good marker to discuss the strength of the hydrogen bonding is formed in the protonated Schiff base because this vibrational mode is strongly coupled with the C=N-H bending vibration.[55-57] The schematic diagram is shown in Figure 1-15. Since the C=N-H bending mode is directly affected by the hydrogen bond strength in the protonated Schiff base, the stronger hydrogen bond strength pushes up the frequency of the coupled C=N stretching mode than its pure level. When the hydrogen atom is replaced with the deuterium atom, the pure C=N stretching vibration is observed due to the decoupling between C=N stretching mode and C=N-D bending mode. Therefore, the larger deuteration shift, the stronger the hydrogen bond strength. The hydrogen bond strength in the protonated Schiff base is significantly important for the rhodopsin function because the proton transfer from the protonated Schiff base to its counterion or water is the key reaction. Therefore, the hydrogen bond strength has been discussed in many rhodopsins using this marker band.[45, 46, 53, 58-60]

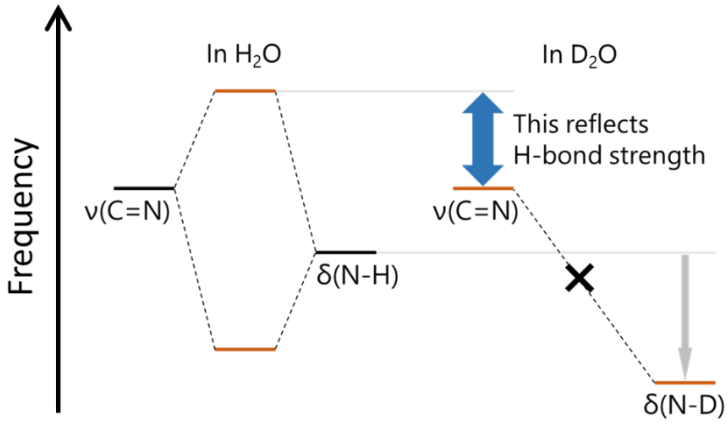

Figure 1-15. Energy diagram of the C=N stretching mode and N-H bending mode. The deuteration shift reflects the hydrogen bond strength in the protonated Schiff base.

The bandwidth of this band can also provide us the important information of the Schiff base. The energy level between the C=N stretching mode and the H-O-H bending mode of a water molecule is similar to each other. Therefore, if the proton acceptor of the Schiff base is a water molecule, resonance vibrational energy transfer occurs and it broadens the bandwidth of ν(C=N) band only when the protein is dissolved in H_2O buffer. Since the band broadening does not occur in D_2O buffer, we can investigate whether the hydrogen bond acceptor is a water molecule or not.[45, 61, 62]

1.4.3. Marker Bands of Aromatic Amino Acids Residues

Ultraviolet resonance Raman (UVRR) spectroscopy is used for studying the protein structure because of some strong π–π* electric transitions in the UV region by aromatic amino acid side chains. In this study, 233 nm wavelength laser was used as a probe light, where mainly vibrational modes of Trp and Tyr residues are selectively observed as shown in Figure 1-16. The following describes the major marker bands used to discuss the structure and environment of Trp and Tyr residues.

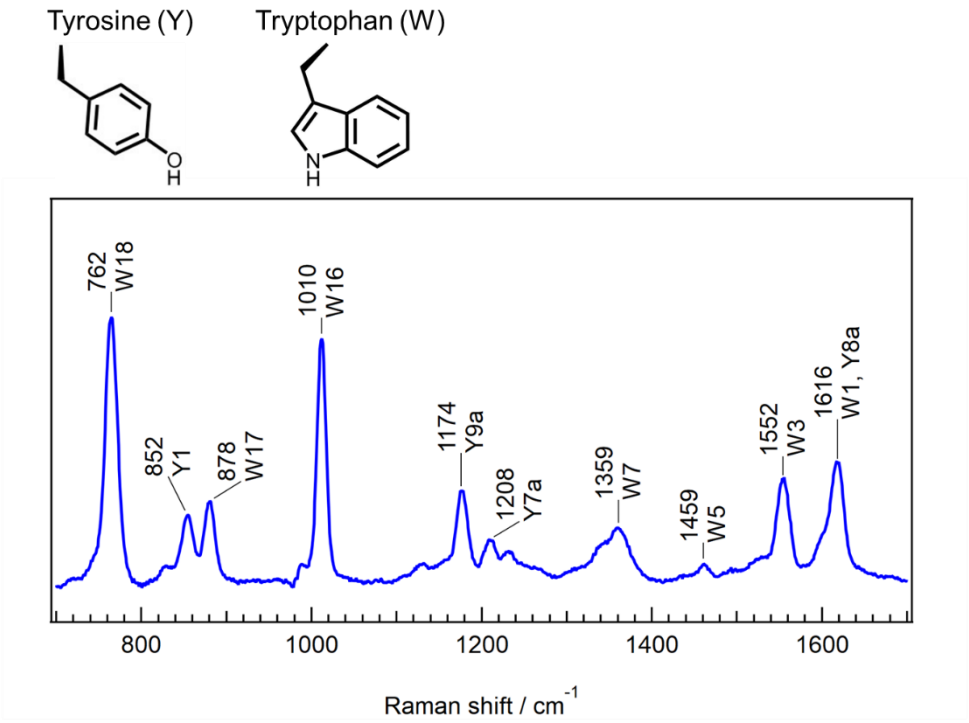

Figure 1-16. UVRR spectrum of KR2 excited at 233 nm. The bands mainly arise from Trp and Tyr side chain vibrations as denoted labels W and Y, respectively.

Tryptophan Residue

Tryptophan (Trp) residue has the nonpolar surface area which is polarizable, an N-H moiety can be donated to the forming a hydrogen bond, and the conjugated π electron for cation-π interactions. As can be seen from these properties, Trp residue plays an important function, especially in membrane proteins.[63] The indole ring of tryptophan (Trp) residue has the strongest absorption peak around 220 nm due to the B_b transition and two weak bands around 270 nm due to the L_a and L_b transitions.[64] Since the excitation wavelength in this study is 233 nm, we obtained the vibrational modes of Trp residue mainly came from the B_b transition.

W3 band

The band at 1552 cm^{-1} is assigned to W3 mode, mainly attributed to C_2=C_3 stretching mode. This band can be used to a marker of the dihedral angle ($\chi^{2,1}$) of the C_2-C_3-C_β-C_α linkage (Fig. 1-17).[65-68] The relationship between the frequency of W3 band and $\chi^{2,1}$ was investigated and can be described as follows.

$$\nu(\mathrm{W3}) = 1542 + 6.7 \cdot (\cos(3|\chi^{2,1}|) + 1)^{1.2}$$

This correlation is observed in the 60-120º range of $|\chi^{2,1}|$. The frequency is also the marker for bond order of the pyrrole ring of the radical.[69]

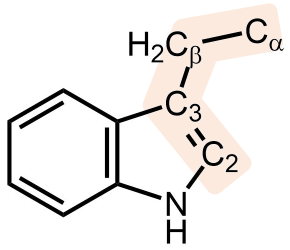

Figure 1-17. Molecular structure of Trp residue. The orange colored region shows the C_2-C_3-C_α-C_β linkage.

W7 band

The doublet band observed around 1350 cm^{-1} is attributed to the pyrrole ring vibration, W7.[68, 70] This band usually shows doublet or triplet due to the Fermi resonance between a fundamental N-C stretching mode and combinations of out-of-plane bending vibration of the indole ring.[71, 72] The doublet intensity ratio I_{1360}/I_{1340} increases when the hydrophobicity increases around the Trp side chain so that it can be used as a marker of the environment to which Trp is exposed.[63, 68] With excitation at a wavelength of 230 nm, the ratio I_{1360}/I_{1340} shows the correlation with the solvent polarity.[63] Therefore, it may be utilized as a marker of the solvent polarity.

W16, 18 bands

The strongest bands at 1010 and 762 cm^{-1} are assigned as the breathing mode of the indole ring (W16) and the breathing mode of the benzene ring (W18), respectively.[68] The Raman intensity of these bands is strongly affected by the solvent environments which can be parameterized by Kamlet–Taft solvatochromic equation.[73, 74] Chi et al. observed the Raman cross section of *N*-acetyltryptophan ethyl ester in the various water–propanol composition and showed the Raman cross section increases as the water concentration decreases, indicating these bands intensity can be utilized as a marker of the solvent exposure and local environment.[74]

Miura et al. found that the frequency of W18 band shows an inverse relationship with that of the N-H stretching band, which reflects the hydrogen bond strength in the indole ring.[65] If the indole ring forms a weak hydrogen bond, the W18 frequency is observed higher position. Because the change in frequency due to the difference in hydrogen bond strength is too small, the overtone of W18 band frequency is often used as a marker of the hydrogen bond strength.[75, 76]

Okuda et al. reported that the cation–π interaction, involved in the Trp side chain affects the intensity of the W16 band.[77] Based on the result, Diana et al. proposed that the intensity ratio of I_{W16}/ I_{W18} can be utilized as a marker of the strength of the cation–π interaction.[63]

W17 band

The band observed at 878 cm^{-1} is assigned to W17 band which is a mixture of the modes of the benzene ring and the N-H in-plane deformation.[68, 71] Since the N-H stretching mode is indistinguishable due to the many amide bands and O-H stretching vibration, W17 band is a good probe to investigate the environment of the hydrogen bond forms in Trp side chain. The W17 frequency decreases with the increase of the strength of the hydrogen bond.[78] The W17 frequency shows the range from 871 cm^{-1} to 883 cm^{-1} depending on the hydrogen bond strength.[79]

Tyrosine Residue

Since tyrosine (Tyr) residue has a hydroxyl group, it can act as a hydrogen bond acceptor or donor. The benzene ring of Try side chain can form cation–π interaction or π–π stacking interaction they are important for the protein folding. Furthermore, tyrosine phosphorylation is involved in various neurotransmissions. Thus, Tyr residues are key factors for biological events. The absorption spectrum of Tyr shows a strong band at 225 nm a weak band at 275 nm, derived from the L_b and L_a electronic transition.[74] The absorption spectra of *N*-acetyltryrosine ethyl ester in the various water–propanol composition demonstrated the L_b band redshifts as the composition of water decreases.[74] Thus, the resonance Raman band of Tyr with excitation at a wavelength of 233 nm, where I used in my study, can be affected by the solvent environment.

Y1 band

The in-plane vibration mode of the phenyl ring of Tyr (Y1) observed at ~850 cm^{-1}. Frequently, the doublet band at 850/830 cm^{-1}, which arises from a Fermi resonance between Y1 band and the overtone of an out-of-plane ring vibration.[79] The intensity ratio I_{850}/I_{830} can be used as a marker of the hydrogen bond strength because the hydrogen bonding may alter the Fermi resonance resulting in a change of this ratio. This ratio becomes large when the hydroxyl group of Tyr acts as the hydrogen acceptor. If Tyr does not form any hydrogen bond, the singlet band is observed instead of the doublet band.

Y7a band

The C-C stretching vibration of the phenyl ring, observed at 1208 cm^{-1} is Y7a band. Takeuchi et al. demonstrated that based on the Raman spectra of the crystalline tyrosine and its derivatives, the Y7a frequency depends on the state of hydrogen bonding. Namely, the observed frequency was 1205 and 1210 cm^{-1} in the proton-donating state and the proton-accepting state, respectively.[80] Thus, the Y7a band is used as a marker of the state

of hydrogen bonding in the Tyr side chain.

Y8a band

Y8a band observed at 1617 cm^{-1} is attributed to mainly the in-plane stretching mode of the phenyl ring. The Y8a frequency downshifts by 15 cm^{-1} when the phenolic OH group is deprotonated due to the delocalization of the negative charge of oxygen to the benzene ring with the redshift of the electronic transition.[79, 81] As well as W16 and W18, the Raman cross section of Y8a band is also sensitive to the hydrophobic environment.[74] Namely, the intensity of Y8a band increases as the water concentration decreases so that the intensity change can be used to discuss the environment of Tyr residues.

Y9a band

The band observed at 1175 cm^{-1} is Y9a band which can be attributed to the C-H bending mode of Tyr.[80] In contrast to the frequency of Y7a band, the Y9a frequency does not simply reflect the state of hydrogen bonding. Takeuchi et al. observed the Raman spectra of $_L$-tyrosine (Tyr) and $_L$-tyrosine ethyl ester (TyrEE) and compared their Y9a frequency.[80] Even though the state of hydrogen bonding is similar between them, the observed frequency was different by 6 $cm^{-1.}$ They proposed that the Y9a frequency is affected by the dihedral angle formed between the hydroxyl group and the benzene plane. If the dihedral angle is small, the van der Waals contact between hydrogen atoms of the hydroxyl group and the benzene ring arises and push up the Y9a frequency. The use of crystallography with known the dihedral angles ensured the validity of this proposal. Therefore, the Y9a frequency is used as a marker of the direction of the hydroxyl group toward the benzene ring. Furthermore, the deprotonation of the hydroxyl group of Tyr causes the downshift of the Y9a frequency because of the disappearance of repulsion between hydrogen atoms and delocalization of the lone pair on oxygen atom.[80]

1.5. Aim of This Thesis

The aim of this thesis is to reveal the universal mechanism of rhodopsins showing a wide variety of functions from the viewpoint of the molecular chemical structure. The resonance Raman spectroscopy allows selective observation of the molecular structure, which plays a key role in the protein function. Here, I used a light-driven sodium/proton pump rhodopsin, KR2, and Heliorhodopsins whose functions are still unknown discovered from two distinct bacteria. KR2 is a good probe to investigate how rhodopsins determine the function because KR2 shows the functional conversion depending on the coexisting ion species. I observed the chromophore structure of KR2 under various solution conditions using resonance Raman spectroscopy and proposed a new model for the ion recognition mechanisms in KR2 (Chapter 3). Since much of the research on the ion transport mechanism of KR2 observes the retinal chromophore, it is an important and challenging issue to reveal structural changes in the protein moiety during the ion transport in KR. I succeeded in observing the protein structural changes in sodium ion transport process using time-resolved ultraviolet resonance Raman spectroscopy, for the first time (Chapter 4). Heliorhodopsin is a newly discovered group of rhodopsin, but its function is unknown. I conducted the resonance Raman spectroscopy to Heliorhodopsin in order to reveal the chromophore structure and its environment, and compared them with that of microbial rhodopsin. I could suggest that Heliorhodopsins function as a photosensor on the basis of the spectroscopic features (Chapter 5).

1.6. Conclusion

In this chapter, I described the general introduction of the study of rhodopsins and the basic principle of resonance Raman spectroscopy. The features of my study are the elucidation of the relationship between the structure and function of proteins from the observation of the molecular structures, which are the “key” to generate protein functions. Application of the advanced vibrational spectroscopy to the biomolecule in this study will provide us the new knowledge of life science.

1.7. References

[1] Oesterhelt, D., and Stoeckenius, W. (1971) Rhodopsin-Like Protein from the Purple Membrane of *Halobacterium Halobium*, *Nature New Biology 233*, 149-152.

[2] Birge, R. R. (1981) Photophysics of Light Transduction in Rhodopsin and Bacteriorhodopsin, *Annu. Rev. Biophys. Bioeng. 10*, 315-354.

[3] Stoeckenius, W., and Bogomolni, R. A. (1982) Bacteriorhodopsin and Related Pigments of *Halobacteria*, *Annu. Rev. Biochem 51*, 587-616.

[4] Luecke, H., Schobert, B., Richter, H.-T., Cartailler, J.-P., and Lanyi, J. K. (1999) Structure of Bacteriorhodopsin at 1.55 Å Resolution 11Edited by D. C. Rees, *J. Mol. Biol. 291*, 899-911.

[5] Henderson, R., Baldwin, J. M., Ceska, T. A., Zemlin, F., Beckmann, E., and Downing, K. H. (1990) Model for the Structure of Bacteriorhodopsin Based on High-Resolution Electron Cryo-Microscopy, *J. Mol. Biol. 213*, 899-929.

[6] Oesterhelt, F., Oesterhelt, D., Pfeiffer, M., Engel, A., Gaub, H. E., and Müller, D. J. (2000) Unfolding Pathways of Individual Bacteriorhodopsins, *Science 288*, 143.

[7] Nango, E., Royant, A., Kubo, M., Nakane, T., Wickstrand, C., Kimura, T., Tanaka, T., Tono, K., Song, C., Tanaka, R., Arima, T., Yamashita, A., Kobayashi, J., Hosaka, T., Mizohata, E., Nogly, P., Sugahara, M., Nam, D., Nomura, T., Shimamura, T., Im, D., Fujiwara, T., Yamanaka, Y., Jeon, B., Nishizawa, T., Oda, K., Fukuda, M., Andersson, R., Båth, P., Dods, R., Davidsson, J., Matsuoka, S., Kawatake, S., Murata, M., Nureki, O., Owada, S., Kameshima, T., Hatsui, T., Joti, Y., Schertler, G., Yabashi, M., Bondar, A.-N., Standfuss, J., Neutze, R., and Iwata, S. (2016) A Three-Dimensional Movie of Structural Changes in Bacteriorhodopsin, *Science 354*, 1552.

[8] Smith, S. O., Lugtenburg, J., and Mathies, R. A. (1985) Determination of Retinal Chromophore Structure in Bacteriorhodopsin with Resonance Raman Spectroscopy, *J. Membr. Biol. 85*, 95-109.

[9] Ernst, O. P., Lodowski, D. T., Elstner, M., Hegemann, P., Brown, L. S., and Kandori, H. (2014) Microbial and Animal Rhodopsins: Structures, Functions, and Molecular Mechanisms, *Chem. Rev. 114*, 126-163.

[10] Matsuno-Yagi, A., and Mukohata, Y. (1977) Two Possible Roles of Bacteriorhodopsin; A Comparative Study of Strains of *Halobacterium Halobium* Differing in Pigmentation, *Biochem. Biophys. Res. Commun. 78*, 237-243.

[11] Bogomolni, R. A., and Spudich, J. L. (1982) Identification of a Third Rhodopsin-Like Pigment in Phototactic *Halobacterium Halobium*, *Proc. Natl. Acad. Sci. U. S. A. 79*, 6250.

[12] Takahashi, T., Tomioka, H., Kamo, N., and Kobatake, Y. (1985) A Photosystem Other Than PS370 Also Mediates the Negative Phototaxis of *Halobacterium Halobium*, *FEMS*

Microbiol. Lett. 28, 161-164.

[13] Venter, J. C., Remington, K., Heidelberg, J. F., Halpern, A. L., Rusch, D., Eisen, J. A., Wu, D., Paulsen, I., Nelson, K. E., Nelson, W., Fouts, D. E., Levy, S., Knap, A. H., Lomas, M. W., Nealson, K., White, O., Peterson, J., Hoffman, J., Parsons, R., Baden-Tillson, H., Pfannkoch, C., Rogers, Y. H., and Smith, H. O. (2004) Environmental Genome Shotgun Sequencing of the Sargasso Sea, *Science 304*, 66-74.

[14] Beja, O., Aravind, L., Koonin, E. V., Suzuki, M. T., Hadd, A., Nguyen, L. P., Jovanovich, S. B., Gates, C. M., Feldman, R. A., Spudich, J. L., Spudich, E. N., and DeLong, E. F. (2000) Bacterial Rhodopsin: Evidence for a New Type of Phototrophy in the Sea, *Science 289*, 1902-1906.

[15] Jung, K. H., Trivedi, V. D., and Spudich, J. L. (2003) Demonstration of a Sensory Rhodopsin in Eubacteria, *Mol. Microbiol. 47*, 1513-1522.

[16] Nagel, G., Ollig, D., Fuhrmann, M., Kateriya, S., Musti, A. M., Bamberg, E., and Hegemann, P. (2002) Channelrhodopsin-1: A Light-gated Proton Channel in Green Algae, *Science 296*, 2395-2398.

[17] Schneider, F., Grimm, C., and Hegemann, P. (2015) Biophysics of Channelrhodopsin, *Annu Rev Biophys 44*, 167-186.

[18] Kandori, H., Inoue, K., and Tsunoda, S. P. (2018) Light-Driven Sodium-Pumping Rhodopsin: A New Concept of Active Transport, *Chem. Rev. 118*, 10646-10658.

[19] Inoue, K., Ono, H., Abe-Yoshizumi, R., Yoshizawa, S., Ito, H., Kogure, K., and Kandori, H. (2013) A Light-Driven Sodium Ion Pump in Marine Bacteria, *Nat. Commun. 4*, 1678.

[20] Inoue, K., Ito, S., Kato, Y., Nomura, Y., Shibata, M., Uchihashi, T., Tsunoda, S. P., and Kandori, H. (2016) A Natural Light-driven Inward Proton Pump, *Nat. Commun. 7*, 13415.

[21] Scheib, U., Stehfest, K., Gee, C. E., Körschen, H. G., Fudim, R., Oertner, T. G., and Hegemann, P. (2015) The Rhodopsin–Guanylyl Cyclase of the Aquatic Fungus *Blastocladiella emersonii* Enables Fast Optical Control of cGMP Signaling, *Science Signaling 8*, rs8-rs8.

[22] Shichida, Y., and Matsuyama, T. (2009) Evolution of Opsins and Phototransduction, *Philos. Trans. R. Soc. Lond. B Biol. Sci. 364*, 2881-2895.

[23] Schmidt, T. M., Chen, S. K., and Hattar, S. (2011) Intrinsically Photosensitive Retinal Ganglion Cells: Many Subtypes, Diverse Functions, *Trends Neurosci. 34*, 572-580.

[24] Kiser, P. D., Golczak, M., and Palczewski, K. (2014) Chemistry of the Retinoid (visual) Cycle, *Chem. Rev. 114*, 194-232.

[25] Lamb, T. D., and Pugh, E. N., Jr. (2006) Phototransduction, Dark Adaptation, and Rhodopsin Regeneration The Proctor Lecture, *Invest. Ophthalmol. Vis. Sci. 47*, 5138-5152.

[26] Pushkarev, A., Inoue, K., Larom, S., Flores-Uribe, J., Singh, M., Konno, M., Tomida, S., Ito,

S., Nakamura, R., Tsunoda, S. P., Philosof, A., Sharon, I., Yutin, N., Koonin, E. V., Kandori, H., and Beja, O. (2018) A Distinct Abundant Group of Microbial Rhodopsins Discovered Using Functional Metagenomics, *Nature 558*, 595-599.

[27] Gushchin, I., Shevchenko, V., Polovinkin, V., Kovalev, K., Alekseev, A., Round, E., Borshchevskiy, V., Balandin, T., Popov, A., Gensch, T., Fahlke, C., Bamann, C., Willbold, D., Buldt, G., Bamberg, E., and Gordeliy, V. (2015) Crystal Structure of a Light-Driven Sodium Pump, *Nat. Struct. Mol. Biol. 22*, 390-395.

[28] Kato, H. E., Inoue, K., Abe-Yoshizumi, R., Kato, Y., Ono, H., Konno, M., Hososhima, S., Ishizuka, T., Hoque, M. R., Kunitomo, H., Ito, J., Yoshizawa, S., Yamashita, K., Takemoto, M., Nishizawa, T., Taniguchi, R., Kogure, K., Maturana, A. D., Iino, Y., Yawo, H., Ishitani, R., Kandori, H., and Nureki, O. (2015) Structural Basis for Na^+ Transport Mechanism by a Light-driven Na^+ Pump, *Nature 521*, 48-53.

[29] Gushchin, I., Shevchenko, V., Polovinkin, V., Borshchevskiy, V., Buslaev, P., Bamberg, E., and Gordeliy, V. (2016) Structure of the Light-driven Sodium Pump KR2 and Its Implications for Optogenetics, *The FEBS Journal 283*, 1232-1238.

[30] Kovalev, K., Polovinkin, V., Gushchin, I., Alekseev, A., Shevchenko, V., Borshchevskiy, V., Astashkin, R., Balandin, T., Bratanov, D., Vaganova, S., Popov, A., Chupin, V., Buldt, G., Bamberg, E., and Gordeliy, V. (2019) Structure and Mechanisms of Sodium-Pumping KR2 Rhodopsin, *Sci Adv 5*, eaav2671.

[31] Shibata, M., Inoue, K., Ikeda, K., Konno, M., Singh, M., Kataoka, C., Abe-Yoshizumi, R., Kandori, H., and Uchihashi, T. (2018) Oligomeric States of Microbial Rhodopsins Determined by High-Speed Atomic Force Microscopy and Circular Dichroic Spectroscopy, *Sci. Rep. 8*, 8262.

[32] Inoue, K., Konno, M., Abe-Yoshizumi, R., and Kandori, H. (2015) The Role of the NDQ Motif in Sodium-Pumping Rhodopsins, *Angew. Chem. Int. Ed. Engl. 54*, 11536-11539.

[33] Kato, Y., Inoue, K., and Kandori, H. (2015) Kinetic Analysis of H^+-Na^+ Selectivity in a Light-Driven Na^+-Pumping Rhodopsin, *J. Phys. Chem. Lett. 6*, 5111-5115.

[34] Ono, H., Inoue, K., Abe-Yoshizumi, R., and Kandori, H. (2014) FTIR Spectroscopy of a Light-Driven Compatible Sodium Ion-proton Pumping Rhodopsin at 77 K, *J. Phys. Chem. B 118*, 4784-4792.

[35] Hontani, Y., Inoue, K., Kloz, M., Kato, Y., Kandori, H., and Kennis, J. T. (2016) The Photochemistry of Sodium Ion Pump Rhodopsin Observed by Watermarked Femto- to Submillisecond Stimulated Raman Spectroscopy, *Phys. Chem. Chem. Phys. 18*, 24729-24736.

[36] da Silva, G. F., Goblirsch, B. R., Tsai, A. L., and Spudich, J. L. (2015) Cation-Specific Conformations in a Dual-Function Ion-Pumping Microbial Rhodopsin, *Biochemistry 54*,

3950-3959.

[37] Shigeta, A., Ito, S., Kaneko, R., Tomida, S., Inoue, K., Kandori, H., and Kawamura, I. (2018) Long-Distance Perturbation on Schiff Base-counterion Interactions by His30 and the Extracellular Na^+-Binding Site in *Krokinobacter* Rhodopsin 2, *Phys. Chem. Chem. Phys. 20*, 8450-8455.

[38] Kaur, J., Kriebel, C. N., Eberhardt, P., Jakdetchai, O., Leeder, A. J., Weber, I., Brown, L. J., Brown, R. C. D., Becker-Baldus, J., Bamann, C., Wachtveitl, J., and Glaubitz, C. (2018) Solid-State NMR Analysis of the Sodium Pump *Krokinobacter* Rhodopsin 2 and Its H30A Mutant, *J. Struct. Biol. 206*, 55-65.

[39] Tahara, S., Takeuchi, S., Abe-Yoshizumi, R., Inoue, K., Ohtani, H., Kandori, H., and Tahara, T. (2018) Origin of the Reactive and Nonreactive Excited States in the Primary Reaction of Rhodopsins: pH Dependence of Femtosecond Absorption of Light-Driven Sodium Ion Pump Rhodopsin KR2, *J. Phys. Chem. B 122*, 4784-4792.

[40] Konno, M., Kato, Y., Kato, H. E., Inoue, K., Nureki, O., and Kandori, H. (2016) Mutant of a Light-Driven Sodium Ion Pump Can Transport Cesium Ions, *J. Phys. Chem. Lett. 7*, 51-55.

[41] Tomida, S., Ito, S., Inoue, K., and Kandori, H. (2018) Hydrogen-bonding Network at the Cytoplasmic Region of a Light-Driven Sodium Pump Rhodopsin KR2, *Biochim. Biophys. Acta 1859*, 684-691.

[42] Inoue, K., Nomura, Y., and Kandori, H. (2016) Asymmetric Functional Conversion of Eubacterial Light-Driven Ion Pumps, *J. Biol. Chem. 291*, 9883-9893.

[43] Vogt, A., Silapetere, A., Grimm, C., Heiser, F., Ancina Moller, M., and Hegemann, P. (2019) Engineered Passive Potassium Conductance in the KR2 Sodium Pump, *Biophys. J. 116*, 1941-1951.

[44] Suomivuori, C. M., Gamiz-Hernandez, A. P., Sundholm, D., and Kaila, V. R. I. (2017) Energetics and Dynamics of a Light-Driven Sodium-pumping Rhodopsin, *Proc. Natl. Acad. Sci. U. S. A. 114*, 7043-7048.

[45] Nishimura, N., Mizuno, M., Kandori, H., and Mizutani, Y. (2019) Distortion and a Strong Hydrogen Bond in the Retinal Chromophore Enable Sodium-Ion Transport by the Sodium-Ion Pump KR2, *J. Phys. Chem. B 123*, 3430-3440.

[46] Kajimoto, K., Kikukawa, T., Nakashima, H., Yamaryo, H., Saito, Y., Fujisawa, T., Demura, M., and Unno, M. (2017) Transient Resonance Raman Spectroscopy of a Light-Driven Sodium-Ion-Pump Rhodopsin from *Indibacter alkaliphilus*, *J. Phys. Chem. B 121*, 4431-4437.

[47] Asido, M., Eberhardt, P., Kriebel, C. N., Braun, M., Glaubitz, C., and Wachtveitl, J. (2019) Time-resolved IR Spectroscopy Reveals Mechanistic Details of Ion Transport in the

Sodium Pump *Krokinobacter eikastus* rhodopsin 2, *Phys. Chem. Chem. Phys. 21*, 4461-4471.

[48] Chen, H. F., Inoue, K., Ono, H., Abe-Yoshizumi, R., Wada, A., and Kandori, H. (2018) Time-resolved FTIR Study of Light-Driven Sodium Pump Rhodopsins, *Phys. Chem. Chem. Phys. 20*, 17694-17704.

[49] Singh, M., Inoue, K., Pushkarev, A., Béjà, O., and Kandori, H. (2018) Mutation Study of Heliorhodopsin 48C12, *Biochemistry 57*, 5041-5049.

[50] Tahara, S., Singh, M., Kuramochi, H., Shihoya, W., Inoue, K., Nureki, O., Béjà, O., Mizutani, Y., Kandori, H., and Tahara, T. (2019) Ultrafast Dynamics of Heliorhodopsins, *J. Phys. Chem. B 123*, 2507-2512.

[51] Shibukawa, A., Kojima, K., Nakajima, Y., Nishimura, Y., Yoshizawa, S., and Sudo, Y. (2019) Photochemical Characterization of a New Heliorhodopsin from the Gram-Negative Eubacterium Bellilinea caldifistulae (BcHeR) and Comparison with Heliorhodopsin-48C12, *Biochemistry 58*, 2934-2943.

[52] Eyring, G., Curry, B., Mathies, R., Fransen, R., Palings, I., and Lugtenburg, J. (1980) Interpretation of the Resonance Raman Spectrum of Bathorhodopsin Based on Visual Pigment Analogues, *Biochemistry 19*, 2410-2418.

[53] Smith, S. O., Braiman, M. S., Myers, A. B., Pardoen, J. A., Courtin, J. M. L., Winkel, C., Lugtenburg, J., and Mathies, R. A. (1987) Vibrational Analysis of the All-T*rans*-Retinal Chromophore in Light-Adapted Bacteriorhodopsin, *J. Am. Chem. Soc. 109*, 3108-3125.

[54] Smith, S. O., Myers, A. B., Pardoen, J. A., Winkel, C., Mulder, P. P., Lugtenburg, J., and Mathies, R. (1984) Determination of Retinal Schiff Base Configuration in Bacteriorhodopsin, *Proc. Natl. Acad. Sci. U. S. A. 81*, 2055-2059.

[55] Baasov, T., Friedman, N., and Sheves, M. (1987) Factors Affecting the C=N Stretching in Protonated Retinal Schiff Base: A Model Study for Bacteriorhodopsin and Visual Pigments, *Biochemistry 26*, 3210-3217.

[56] Gilson, H. S., Honig, B. H., Croteau, A., Zarrilli, G., and Nakanishi, K. (1988) Analysis of the Factors that Influence the C=N Stretching Frequency of Polyene Schiff Bases. Implications for Bacteriorhodopsin and Rhodopsin, *Biophys. J. 53*, 261-269.

[57] Deng, H., and Callender, R. H. (1987) A Study of the Schiff Base Mode in Bovine Rhodopsin and Bathorhodopsin, *Biochemistry 26*, 7418-7426.

[58] Gellini, C., Luttenberg, B., Sydor, J., Engelhard, M., and Hildebrandt, P. (2000) Resonance Raman Spectroscopy of Sensory Rhodopsin II from *Natronobacterium pharaonis*, *FEBS Lett. 472*, 263-266.

[59] Mizuno, M., Nakajima, A., Kandori, H., and Mizutani, Y. (2018) Structural Evolution of a Retinal Chromophore in the Photocycle of Halorhodopsin from *Natronobacterium*

pharaonis, *J. Phys. Chem. A 122*, 2411-2423.

[60] Maeda, A., Ogurusu, T., Yoshizawa, T., and Kitagawa, T. (1985) Resonance Raman Study on Binding of Chloride to the Chromophore of Halorhodopsin, *Biochemistry 24*, 2517-2521.

[61] Hildebrandt, P., and Stockburger, M. (1984) Role of Water in Bacteriorhodopsin's Chromophore: Resonance Raman Study, *Biochemistry 23*, 5539-5548.

[62] Otomo, A., Mizuno, M., Singh, M., Shihoya, W., Inoue, K., Nureki, O., Beja, O., Kandori, H., and Mizutani, Y. (2018) Resonance Raman Investigation of the Chromophore Structure of Heliorhodopsins, *J. Phys. Chem. Lett. 9*, 6431-6436.

[63] Schlamadinger, D. E., Gable, J. E., and Kim, J. E. (2009) Hydrogen Bonding and Solvent Polarity Markers in the UV Resonance Raman Spectrum of Tryptophan: Application to Membrane Proteins, *J. Phys. Chem. B 113*, 14769-14778.

[64] Matsuno, M., and Takeuchi, H. (1998) Effects of Hydrogen Bonding and Hydrophobic Interactions on the Ultraviolet Resonance Raman Intensities of Indole Ring Vibrations, *Bull. Chem. Soc. Jpn. 71*, 851-857.

[65] Miura, T., Takeuchi, H., and Harada, I. (1989) Tryptophan Raman Bands Sensitive to Hydrogen Bonding and Side-Chain Conformation, *J. Raman Spectrosc. 20*, 667-671.

[66] Maruyama, T., and Takeuchi, H. (1995) Effects of Hydrogen Bonding and Side-Chain Conformation on the Raman Bands of Tryptophan-2,4,5,6,7-d5, *J. Raman Spectrosc. 26*, 319-324.

[67] Juszczak, L. J., and Desamero, R. Z. B. (2009) Extension of the Tryptophan $\chi^{2,1}$ Dihedral Angle−W3 Band Frequency Relationship to a Full Rotation: Correlations and Caveats, *Biochemistry 48*, 2777-2787.

[68] Takeuchi, H., and Harada, I. (1986) Normal Coordinate Analysis of the Indole Ring, *Spectrochim. Acta, Pt. A: Mol. Spectrosc. 42*, 1069-1078.

[69] Shafaat, H. S., Leigh, B. S., Tauber, M. J., and Kim, J. E. (2009) Resonance Raman Characterization of a Stable Tryptophan Radical in an Azurin Mutant, *J. Phys. Chem. B 113*, 382-388.

[70] Hirakawa, A. Y., Nishimura, Y., Matsumoto, T., Nakanishi, M., and Tsuboi, M. (1978) Characterization of a Few Raman Lines of Tryptophan, *J. Raman Spectrosc. 7*, 282-287.

[71] Sweeney, J. A., and Asher, S. A. (1990) Tryptophan UV Resonance Raman Excitation Profiles, *J. Phys. Chem. 94*, 4784-4791.

[72] Harada, I., Miura, T., and Takeuchi, H. (1986) Origin of the Doublet at 1360 and 1340 cm^{-1} in the Raman Spectra of Tryptophan and Related Compounds, *Spectrochim. Acta, Pt. A: Mol. Spectrosc. 42*, 307-312.

[73] Kamlet, M. J., Abboud, J. L., and Taft, R. W. (1977) The Solvatochromic Comparison Method. 6. The π* Scale of Solvent Polarities, *J. Am. Chem. Soc. 99*, 6027-6038.

[74] Chi, Z., and Asher, S. A. (1998) UV Raman Determination of the Environment and Solvent Exposure of Tyr and Trp Residues, *J. Phys. Chem. B 102*, 9595-9602.

[75] Rodgers, K. R., Su, C., Subramaniam, S., and Spiro, T. G. (1992) Hemoglobin R→T Structural Dynamics from Simultaneous Monitoring of Tyrosine and Tryptophan Time-resolved UV Resonance Raman Signals, *J. Am. Chem. Soc. 114*, 3697-3709.

[76] Huang, J., Juszczak, L. J., Peterson, E. S., Shannon, C. F., Yang, M., Huang, S., Vidugiris, G. V. A., and Friedman, J. M. (1999) The Conformational and Dynamic Basis for Ligand Binding Reactivity in Hemoglobin Ypsilanti (β99 Asp→Tyr): Origin of the Quaternary Enhancement Effect, *Biochemistry 38*, 4514-4525.

[77] Okada, A., Miura, T., and Takeuchi, H. (2001) Protonation of Histidine and Histidine−Tryptophan Interaction in the Activation of the M2 Ion Channel from Influenza A Virus, *Biochemistry 40*, 6053-6060.

[78] Miura, T., Takeuchi, H., and Harada, I. (1988) Characterization of Individual Tryptophan Side Chains in Proteins Using Raman Spectroscopy and Hydrogen-deuterium Exchange Kinetics, *Biochemistry 27*, 88-94.

[79] Takeuchi, H. (2011) UV Raman Markers for Structural Analysis of Aromatic Side Chains in Proteins, *Anal. Sci. 27*, 1077-1086.

[80] Takeuchi, H., Watanabe, N., Satoh, Y., and Harada, I. (1989) Effects of Hydrogen Bonding on the Tyrosine Raman Bands in the 1300–1150 cm^{-1} Region, *J. Raman Spectrosc. 20*, 233-237.

[81] Ludwig, M., and Asher, S. A. (1988) Ultraviolet Resonance Raman Excitation Profiles of Tyrosine: Dependence of Raman Cross Sections on Excited-State Intermediates, *J. Am. Chem. Soc. 110*, 1005-1011.

CHAPTER 2. Materials and Methods

2.1 Protein Preparation

This section describes how to prepare the protein sample mainly about KR2 because purified HeRs were provided by Dr. Manish Singh in the laboratory of Prof. Hideki Kandori.[1] For the preparation of HeRs, see 5-3. Some mutants were used for a variety of reasons in my research, all of them were designed using the WT KR2 plasmid as a template. Thus, basic manipulation of protein preparations described below was the same among WT and mutants. In addition, I used nanodisc-reconstituted KR2, which mimics the physiological environment for the membrane proteins. The preparation of membrane scaffold protein (MSP), is a component of nanodiscs, and the reconstitution of KR2 into the nanodisc will be described in 2.1.5.

2.1.1 Plasmids

The codon-optimized DNA fragment of WT KR2, inserted into the pET21a plasmid vector, was provided by Prof. Hideki Kandori.[2] At the C terminus of KR2 fragment, a 6×His-tag is introduced for affinity purification. The plasmid also contains an ampicillin resistance gene and *lac* operon at the upstream of KR2. The former stands for a selection of plasmids after transformation and the latter are utilized for induction of the translation of KR2. The mutant plasmids of Y25F, S70A, D102N, Y154A, and F72G/D102N/D116T mutants were provided by Dr. Rei-Abe Yoshizumi in the laboratory of Prof. Hideki Kandori.[3-5] and plasmids of W82F, Y154F, W215F, Y218F, Y222F mutants were developed by myself using the Prime STAR MAX DNA polymerase methods (Takara Bio). The synthesize of W113F plasmid was ordered in GeneScript Biotech Corporation because the polymerase chain reaction (PCR) reaction did not work.

Site-directed mutagenesis was performed followed as the protocol of PrimeSTAR Mutagenesis Basal Kit provided by Takara Bio Incorporated. Briefly, the forward and reverse

primer consists of 27 bases, 15 bases were overlapped on the target codon and 12 bases were added on 3' terminal side, was designed for substitutions of the desired codon sequence. The synthesis of these primers was ordered in Thermo Fisher Scientific K.K. Then, for the PCR method, the pre-mixed DNA polymerase and designed primers, template DNA, and distilled water were mixed as shown in Table 2-1. The PCR method was carried out with the thermal cycler (Applied Biosystems, 2720). The annealing temperature was estimated by each melting temperature (Tm) value, depends on guanine-cytosine content and the extension reaction time was calculated to be 32 seconds by the gene size of pET21a contains KR2. The scheme of the PCR method was shown in Figure 2-1. After the PCR reaction, the PCR products were transformed into the *Escherichia coli* (*E. coli*) strain DH5α competent cell. The transformed plasmids were purified using the QIAprep Spin Miniprep Kit (QIAGEN) followed as the protocol provided by QIAGEN. To confirm the DNA sequence, I ordered the sequence analysis in Eurofins Genomics. The T7 promoter and T7 terminator primers, provided by Eurofins Genomics were used for the sequence analysis.

Table 2-1. Component of the PCR reaction.

			volume / μL	
			mutagenesis reaction	negative control
PrimeSTAR MAX Premix			25	25
Primer (forward)	10	pmol / μmol	1	0
Primer (reverse)	10	pmol / μmol	1	0
Template DNA	10 - 100	pg / μL	1	1
Sterillized water			22	24

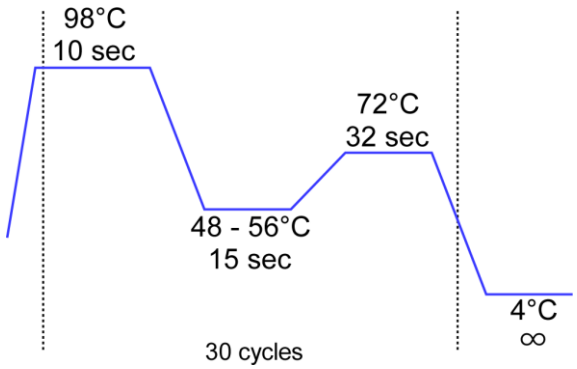

Figure 2-1. PCR conditions. The annealing temperature was in the range of 48 – 56Cº determined by the Tm value of designed primers.

2.1.2 Transformation

KR2 and was expressed in the *E. coli* strain C41 (DE3) (Lucigen Corporation), using the heat shock method. Namely, added 1 μL of DNA to the competent cells. Incubated culture tube containing cells and DNA on ice for 30 minutes. Then, heat shocked cells by placing the culture tube in a 42°C heat block (Eppendorf, Thermomixer compact) for 45 seconds. After that, returned it to the ice for 2 minutes and added 950 μL of recovery medium to the tubes. Shaken it at 250 rpm for 1 hour at 37°C using a shaker incubator (Taitec, Bio Shaker BR-22FH). Finally, spread all into the LB agar plates containing 50 mg/L ampicillin for KR2 and incubate the plates at 37°C in an incubator (SANYO, MIR-162).

2.1.3 Cultivation

A fresh colony of KR2 was added to 100 mL 2×YT medium contains 50 mg/L ampicillin and shaken overnight at 180 rpm at 37°C as pre-cultivation using a shaker incubator (Taitec, Bio Shaker BR-22FH). The pre-cultured medium was added to the 4 L 2×YT medium contains 50 mg/L ampicillin and a few milliliters of defoamer (Merck, Extrain AP31) and incubated at 37°C with air intake using ball filter in an incubator (New Brunswick Scientific, Innova43). Optical density at 600 nm (OD_{600}) was monitored using spectrophotometer (GE Healthcare, Gene Quant 100). When OD_{600} reached 0.6 – 0.8, all-*trans* retinal (Toronto Research Chemicals) and isopropyl-β-thiogalactopyranoside (IPTG) were added to a final concentration of 10 μM and 1 mM, respectively. Four hours after addition, the cells were collected by centrifugation at 8000 rpm for 5 minutes at 4°C using centrifuge (Hitachi, himac CR 20G II). Red- or purple-colored pellets were collected to a 50 mL tube and stored at -80°C until use.

2.1.4 Protein Purification

The stored pellets expressed KR2 were thawed on the ice after adding 40 mL suspension buffer (50 mM Tris-HCl, pH 8.0) containing 5 mM $MgCl_2$. The thawed cells were disrupted by

ultrasonication using an ultrasonic machine (Taitec, VP-30S, φ = 12 mm horn HNN-0200). The output control set to 4.5 and the pellets were sonicated them for 90 seconds for 10 times with 3 minutes' interval on ice. After the disruption, the membrane fraction was collected by centrifugation (12,000 rpm, 20 minutes, 4°C). The supernatant was collected, and it was ultracentrifuged using the ultracentrifuge (Hitachi, himac CS 150 GXII) (36,000 rpm, 60 minutes, 4°C). The precipitate was suspended with buffer (20 mM MES, pH 6.5) containing 300 mM NaCl and 5 mM imidazole and homogenized using homogenizer (AS ONE Corporation, HK-1), set at foot switch variable mode. For solubilization, *n*-dodecyl-β-$_D$-maltoside (DDM) was added to the homogenized solution to the final concentration of 1.5% (w/v) and stir them overnight at 4°C. Then, the solubilized fraction was collected by ultracentrifugation (Hitachi, himac CS 150 GXII) (36,000 rpm, 60 minutes, 4°C). The solubilized KR2 solution was loaded on prepacked Co^{2+}-NTA affinity column (GE Healthcare, Talon crude 5 mL), the sample was washed extensively with buffer (20 mM MES pH 6.5) containing 300 mM NaCl, 50 mM imidazole, and 0.1% DDM to remove non-specifically bound proteins. The sample was then eluted with elution buffer (20 mM MES pH 7.5) containing 500 mM imidazole and 0.1 % DDM. The colored fractions were collected and loaded on an anion exchange column (GE Healthcare, HiTrap Q HP 5 mL) and eluted using a gradient of wash buffer (50 mM Tris-HCl, pH 8.0) containing 0.1% DDM and elution buffer (50 mM Tris-HCl, pH 8.0) containing 1 M NaCl and 0.1% DDM. The protein purification was carried out using a chromatography apparatus (AKTA pure, GE Healthcare) and the protein existence was monitored by the UV absorption at 280 nm.

2.1.5 Nanodiscs Manipulation

For spectroscopic studies of the membrane proteins, the solubilization by detergent, such as DDM is often used. However, the environment of micelles and that of lipid bilayers differ in several respects.[6-8] Nanodiscs have been developed for membrane proteins reconstitution in a membranous environment.[9, 10] Here, the preparation of the MSP and the manipulation of nanodisc sample will be described.

Plasmid of MSP

The synthesized plasmid of MSP (pMSP1E3D1) was ordered in Addgene. The plasmid is inserted into pET28a, containing Kanamycin resistance gene. The 7×His-tag is introduced at N-terminal of the gene of MSP, which is inserted at the downstream of *lac* operon for IPTG induction.

Transformation

MSP was expressed in the *E. coli* strain BL21 (Nippon GENE CO., LTD.), using the heat shock method. Namely, added 1 μL of DNA to the competent cells. Incubated culture tube containing cells and DNA on ice for 30 minutes. Then, heat shocked cells by placing the culture tube in a 42°C heat block (Eppendorf, Thermomixer compact) for 45 seconds. After that, returned it to the ice for 2 minutes and added 950 μL of recovery medium to the tubes. Shaken it at 250 rpm for 1 hour at 37°C. Finally, spread all into the LB agar plates containing 100 mg/L kanamycin and incubate the plates at 37°C in an incubator (SANYO, MIR-162).

Cultivation

For MSP cultivation, the basic manipulation was almost the same as KR2. Namely, a fresh colony of BL21 transformed pMSP1E3D1 was added to 100 mM LB medium contains 100 mg/L Kanamycin and shaken at 180 rpm for 4 hours at 37°C as pre-cultivation using a shaker incubator (Taitec, Bio Shaker BR-22FH), then incubated at 4°C overnight. The pre-cultured

medium was added to the 2 L TB medium contains 100 mg/L Kanamycin and shaken at 180 rpm at 37℃ in the incubator. When the OD_{600} exceeded 2, the induction of expression was started by adding IPTG to the medium to the final concentration of 1 mM and cultured at 37℃ for 1 hour. After that, set the incubation temperature to 28℃ and cultured for 4 hours. The cells were collected by centrifugation at 8000 rpm for 5 minutes at 4℃ using centrifuge (Hitachi, himac CR 20G II) and the colorless pellets were harvested to a 50 mL tube and stored at -80℃ until use.

Protein Purification

For MSP purification, the stored pellets expressed MSP were thawed on the ice after adding 40 mL suspension buffer (20 mM sodium phosphate, pH 7.4) containing 1mM phenylmethylsulfonyl fluoride. The thawed cells were disrupted by ultrasonication, the output control is set to 3.0 and the pellets were sonicated them for 10 seconds for 6 times with 3 min. interval on ice. After the disruption, the MSP solution was ultracentrifuged (30,000 rpm, 1 hour, 4℃). Unlike the case of KR2, MSP was divided into soluble fraction because MSP is expressed as a soluble protein. The supernatant was collected and directly loaded on Ni^{2+}-NTA affinity column (GE Healthcare, HisTrap HP, 5 mL), equilibrated with buffer (40 mM Tris-HCl, pH 8.0) containing 300 mM NaCl. The adsorbed protein was washed with the following sufficient volume of four buffers (40 mM Tris-HCl, pH 8.0), containing (1) 300 mM NaCl and 1% (w/v) Triton X-100 (2) 300 mM NaCl and 50 mM Sodium cholate (3) 300 mM NaCl (4) 300 mM NaCl and 50 mM imidazole). After the column wash, the sample was eluted with elution buffer (40 mM Tris-HCl, pH8.0) containing 1 M imidazole. This assay was carried out using AKTA so that I could collect the fractions containing MSP protein by monitoring the UV absorption at 280 nm. After that, the extra imidazole was removed by buffer exchange using dialysis tube (Spectrum Laboratories, Inc., Spectra/Por 1 Dialysis Membrane Standard RC Tubing MWCO: 6 – 8kD) to 10 mM Tris-HCl pH 7.6 containing 100 mM NaCl and 2 mM EDTA. The buffer was changed at

least 3 times and the last one was treated overnight.

Reconstitution of KR2 into Nanodiscs

A nanodisc is composed of detergent micelles protein and MSP upon removal of the detergent (Figure 2-2). Their components, provided by Prof. Kandori group were shown in Table 2-2. The diameter of MSP is important for the correct reconstitution of proteins in the membrane. Here, MSP1E3D1 whose diameter of 12.9 nm is fully larger to cover with the size of pentameric KR2 was used for preparing the nanodisc assembly.[11] Before mixing, the phospholipids (Sigma Aldrich, Asolectin from soybean) were washed by three times amount of acetone. The yellow-colored supernatant was discarded and washed by acetone again. This wash process was repeated 10 times, and then lipids were dried overnight. The dried lipids were solubilized in a buffer (50 mM Tris-HCl pH 8.0), containing 100 mM NaCl and 4% DDM. After adding the required proteins in 15 mL tube, they were incubated at 4 ℃ by rotating for 1 hour. Then the acetone-washed detergent absorbent beads (Bio-Rad, Bio-Beads SM-2, Adsorbents) was added in order to remove DDM by rotating for 4 hours. The beads were removed by filtration. The absorption spectrum of the obtained sample was shown in Figure 2-3. Since the nanodisc-reconstituted solution was turbid, the background due to the light scattering was increased.

Table 2-2. Composition ratio for assembling of nanodisc-reconstituted KR2.

	mg / mL
DDM-solubilized KR2	0.64
MSP	2.0
Lipid	2.4

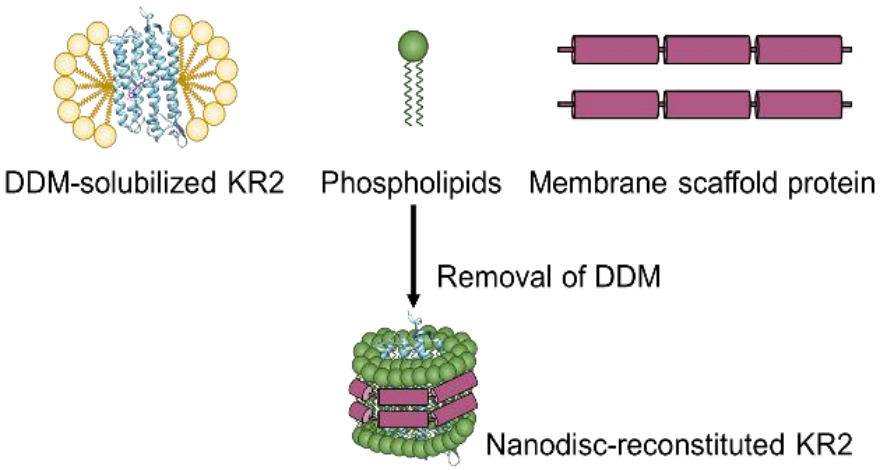

Figure 2-2. Schematic figure of assembly of nanodisc-reconstituted KR2.

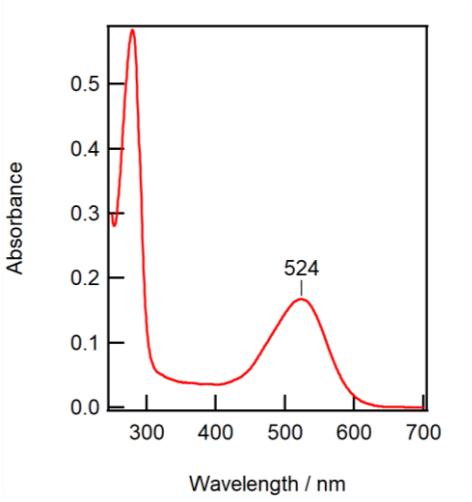

Figure 2-3. Absorption spectrum of nanodisc-reconstituted KR2 in 50 mM Tris-HCl (pH8.0), 100 mM NaCl.

2.2 SDS Polyacrylamide Gel Electrophoresis (SDS-PAGE)

The protein purity was confirmed by SDS-PAGE electrophoresis. The gel for this assay was prepared for 10% polyacrylamide concentration for both separation and stacking gel. For preprocessing, samples were heated at 95℃ for 3 minutes after adding sample buffer with reducing reagent (6×) (Nacalai tesque INC.) to 10 μL of the sample solution. Electrophoresis was carried out at voltage was constant at 200 V at room temperature using electrophoresis tank (Bio-Rad, Powerpac Basic) with a migration buffer solution (Nacalai tesque INC.). The exceed SDS were removed by wash the gel with distilled water then the gel was immersed by Coomassie brilliant blue (Nacalai tesque INC., CBB Stain One Super) dye with shaking 1 hour. Thereafter, the gel was discolored by distilled water at least 3 times and photographed with an imager (Bio-Rad, ChemiDoc XRS+). The electrophoresis results of KR2 and MSP were shown in Figure 2-4. Both KR2 and MSP have a molecular weight of about 32,000 Da from the component of amino acid residues.[9, 12] In Figure 2-4, the main band appeared around 25,000 Da, was smaller than the calculation value. However, because KR2 is an intrinsic membrane protein it is difficult to sufficiently denature using only SDS and heat treatment. Although the apparent molecular weight was small probably due to insufficient denaturation, there was no problem to check the purity, and this main band was determined to be KR2. In both cases, there were bands other than the main band, but it seemed that their amounts were negligibly small. It indicated that both KR2 and MSP had very high purity. The concentration of MSP was adjusted to 2.4 mg/mL and 1 mL of MSP was dispensed into 1.5 mL tube, then stored at -80℃.

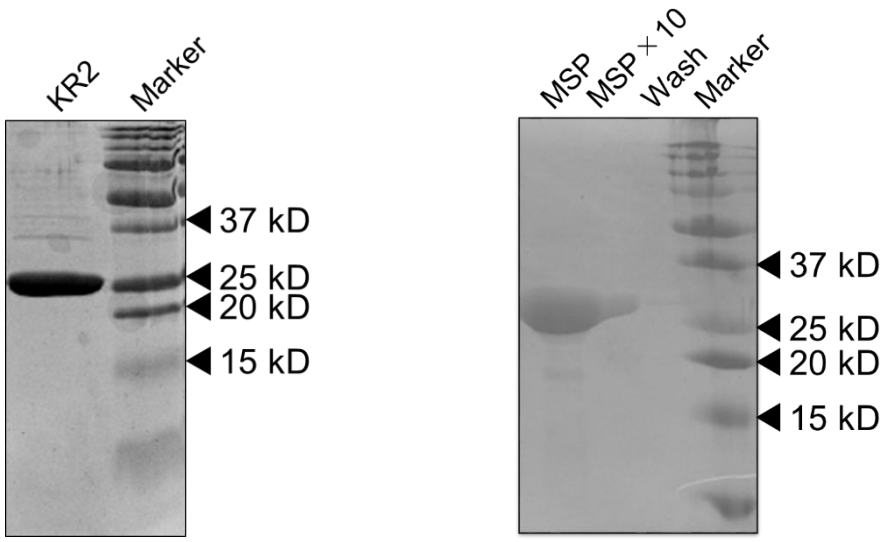

Figure 2-4. SDS-PAGE results of KR2 (left) and MSP (right).

2.3 UV-Visible Absorption Spectrum Measurement

To determine the sample concentration or and analyze the effects of cation concentration on the structure of the retinal chromophore, a spectrophotometer (Shimadzu Corporation, UV-3150) was used to measure UV-vis absorption spectra of KR2 or HeRs. The quartz cuvette with an optical path length of 2 or 10 mm was used as the sample cell. An optical slit was set as 2 nm. In measurement, the cell length was changed or the sample was diluted properly in order to avoid saturation of transmitted light intensity so that the maximum value of absorbance became less than 1.0. The measured spectrum of KR2 was shown in the left panel of Figure 2-5. The main band around 525 nm and a weak band around 400 nm are due to the retinal chromophore and the band at 280 nm is derived from the aromatic amino acid residues. The protein concentration was estimated using the molecular extinction coefficient of KR2 (51,000 $M^{-1}cm^{-1}$).[12] Basically, the yield of KR2 was 1 μmol from 4 L culture. The right panel of Figure 2-5 showed the absorption spectrum of MSP. Since MSP does not possess the visible chromophore, there was only a peak at 280 nm due to the aromatic amino acid residues. From the molecular extinction coefficient of MSP (29,900 $M^{-1}cm^{-1}$),[9] the sample concentration was determined and the yield of MSP was estimated to be 1 μmol form 2 L culture.

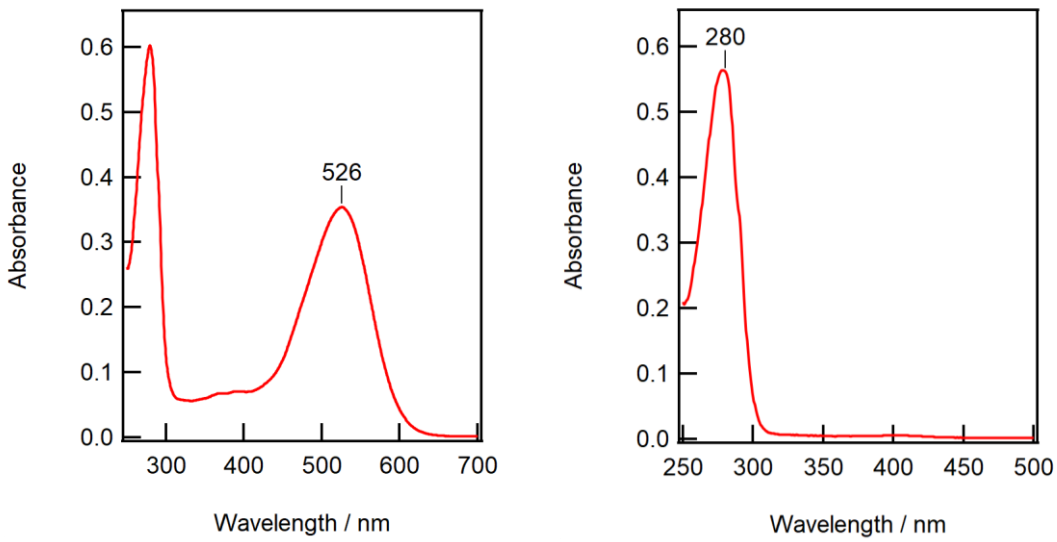

Figure 2-5. Absorption spectrum of KR2 in 50 mM Tris-HCl (pH 8.0), 100 mM NaCl, and 0.1% DDM (left), and MSP in 10 mM Tris-HCl (pH 8.0), 100 mM NaCl and 1 mM EDTA (right).

2.4 Circular Dichroism (CD) Measurement

Although CD spectroscopy is very sensitive to the secondary structure of proteins, here it was used to estimate the oligomeric assembly of KR2. There have been many types of research of applying the CD spectrum to investigate the rhodopsin assembly state.[11, 13, 14] Theoretically, it is explained that when the rhodopsin forms oligomer, the bilobe shape in the visible wavelength region that has been attributed to exaction coupling between the retinal chromophore is observed. On the other hand, an intrinsic positive band is evident in disassembling of the rhodopsin due to the increasing intermolecular distance of chromophores. Recently, the CD spectra of KR2 was reported by Shibata et al.[11]

The CD spectra were obtained in the region of 380-700 nm at 25 ℃ using a circular dichroism spectrometer (JASCO, J-720W). The quartz cuvette with an optical path length of 2 mm was used as the sample cell. Samples were solutions of about 15 μM nanodisc-reconstituted KR2 and 0.1% DDM-solubilized KR2 containing 100 mM NaCl or choline chloride.

2.5 Size Exclusion Chromatography (SEC)

Many of the membrane proteins function efficiently by forming oligomer under its physiological conditions. One of the most convenient methods to study the number of protein assembly is SEC. In SEC experiments, molecules having different molecular weight are separated according to elution time as a sample solution passes through a pored gel. Well defined protein standards are used to calculate the molecular weight. There are some studies which investigated the number of assembly of rhodopsins.[7, 15, 16] However when rhodopsins are solubilized by the detergents, the obtained molecular weight does not directly reflect the number of associations, as rhodopsins forms complex with the detergent. Therefore, it should be noted that SEC results of rhodopsins are just semi-quantitative.

In this study, about 20 μM KR2 in 50 mM Tris-HCl (pH 8.0) containing 0.1% DDM and 100 mM NaCl, KCl, or choline chloride were used for SEC experiments. Samples were applied to a gel filtration column (GE Healthcare, HiPrep 26/60 Sephacryl S-300 HR, Superdex 200 Increase 10/300 GL). The flow rate was 1.5 or 0.75 mM/min for HiPrep 26/60 column or Superdex 200 Increase column, respectively. All SEC experiments were carried out at 4°C on an FPLC instrument (GE Healthcare, Akta). To make a calibration curve, two gel filtration calibration kits were used (GE Healthcare, Gel Filtration Calibration Kit HMW, Bio-Rad, Gel Filtration Standard, 1511901). They cover molecular weights ranging from 1,350 to 669,000. Figure 2-6 represents the calibration curves using Hiprep 26/60 column (A) and Superdex 200 Increase (B).

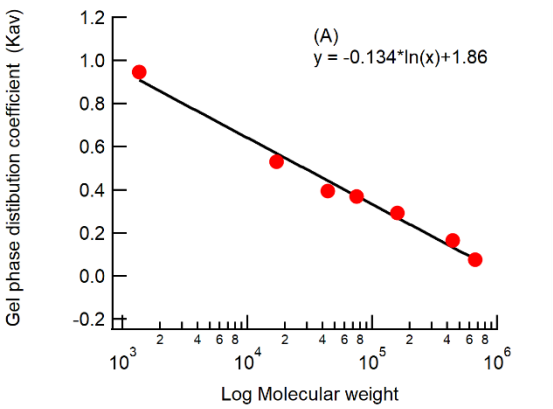

Figure 2-6. Calibration curves for the standard proteins on HiPrep 26/60 Sephacryl S-300 HR (A) and Superdex 200 Increase (B). In (A), Vitamin B12 (Mw = 1,350), Myoglobin horse (17,000), Ovalbumin chicken (44,000), Conalbumin (75,000), Aldorase (158,000), Ferritin (440,000), and Thyroglobulin (669,000) were used. In (B), Myoglobin horse (17,000), Ovalbumin chicken (44,000), Conalbumin (75,000), Aldorase (158,000), Ferritin (440,000), and Thyroglobulin (669,000) were used.

2.6 Measurement of Light-Driven Ion Transport in *E.coli.*

In order to evaluate the light-driven ion transport activity of KR2 and some mutants, an ion transport assay was carried out. In this assay, the light-induced pH changes were measured. When KR2 works as an outward sodium ion pump, the pH increases because the proton motive force is generated. This behavior about the changing pH is enhanced by adding the protonophore carbonyl cyanide 3-chlorophenylhydrazone (CCCP).[12] In contrast, when KR2 pumps proton outwardly, the pH decreases and pH change is canceled after adding CCCP.[12]

For ion transport assay, 4 mL of the KR2-expressed *E. coli* (C41) culture medium, whose OD_{600} is about 4 were collected into the 15 mL tube. They were washed three times with 10 mM NaCl or KCl, 300 mM Na_2SO_4 or K_2SO_4, and 5% (w/v) sucrose solution by centrifugation (7,000 rpm, 2 minutes, 20ºC) and then suspended in the same solution. The cell suspension (7.5 mL) in a glass sample cell connecting to the thermostatic chamber (EYELA, UC-55N) was illuminated using Xe lump (Asahi Spectra Co., Ltd. MAX-303) through a band-pass filter (Opto Sigma, Y48) and cold filter (Opto Sigma, CLDF-50S) at 20℃ for 2.5 minutes. The light-induced pH changes were monitored with a pH meter (Horiba, F-72). A picture of an apparatus is shown in Figure 2-7. After illuminating Xe lump, the sample was incubated in darkness for 10 minutes until the pH fluctuation stabilizes. Then 2.5 μL of 30 mM CCCP dissolved in dimethyl sulfoxide was added and measurements were repeated under the same conditions.

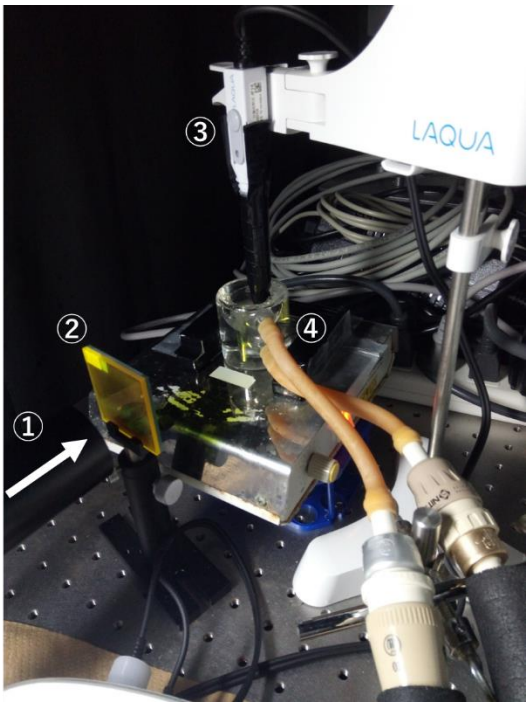

Figure 2-7. An apparatus for the pump activity measurement. 1; the light source, 2; the band-pass filter and the cold filter, 3; the pH meter whose electrode was wrapped by black plastic tape, 4; the sample cell connected to the thermostatic chamber.

2.7 Laser-Flash Photolysis Measurement

Illumination of the short-pulsed light to rhodopsins induces the photoisomerization of the retinal chromophore, triggering a cyclic reaction called the "photocycle". In order to trace each photointermediate of rhodopsins, such as the K, L, M, and O, the laser-flash photolysis measurements have been typically used. The character of these photointermediates is derived from the well-studied bacteriorhodopsin.[17]

In this study, to obtain the time-resolved absorption spectra, 532 nm pulse beam and continuous white light were utilized as a pump and probe light, respectively. A layout of the measurement system is illustrated in Figure 2-8. The pump pulse was the second harmonics of the Nd: YAG laser (Continuum, Minilite) with 7 ns pulse width. The repetition frequency of the pump pulse was adjusted in the range between 0.5 and 10 Hz in response to the lifetime of the photocycle of the samples. The continuous white light was generated by a Xe lamp (Hamamatsu Photonics, L8004-01) and the emission line from the lamp was cut by a correction filter (Asahi Spectra Co., Ltd. Light source correction filter). The pump and probe lights were focused on the sample cell and detected by the multichannel spectrophotometer with an image intensifier (Hamamatsu Photonics, PMA-12 C1002901) behind the sample cell. The intensity of the pump pulse was adjusted by a half-wave plate and a polarized beam splitter, and that of the probe light was adjusted by an iris. In order to generate the delay times, the gate trigger of the detector, which can electrically control the opening and closing, and the oscillation of the pump pulse were synchronized by the delay-generator (Stanford Research Systems, DG535).

Here, about 20 μM of KR2 was circulated by the peristaltic pump (ATTO, Bio-Minipump AC-2120). The sample volume was about 15 mL. For the sample cell, a rectangular-shaped quartz cell having a cross-sectional area of 4 mm^2 (1 mm × 4 mm) was used. The flow rate was carefully adjusted by considering both the lifetime of the photocycle and the repetition

frequency of the pump pulse, to avoid the multiphoton excitation of the protein by the pump pulse.

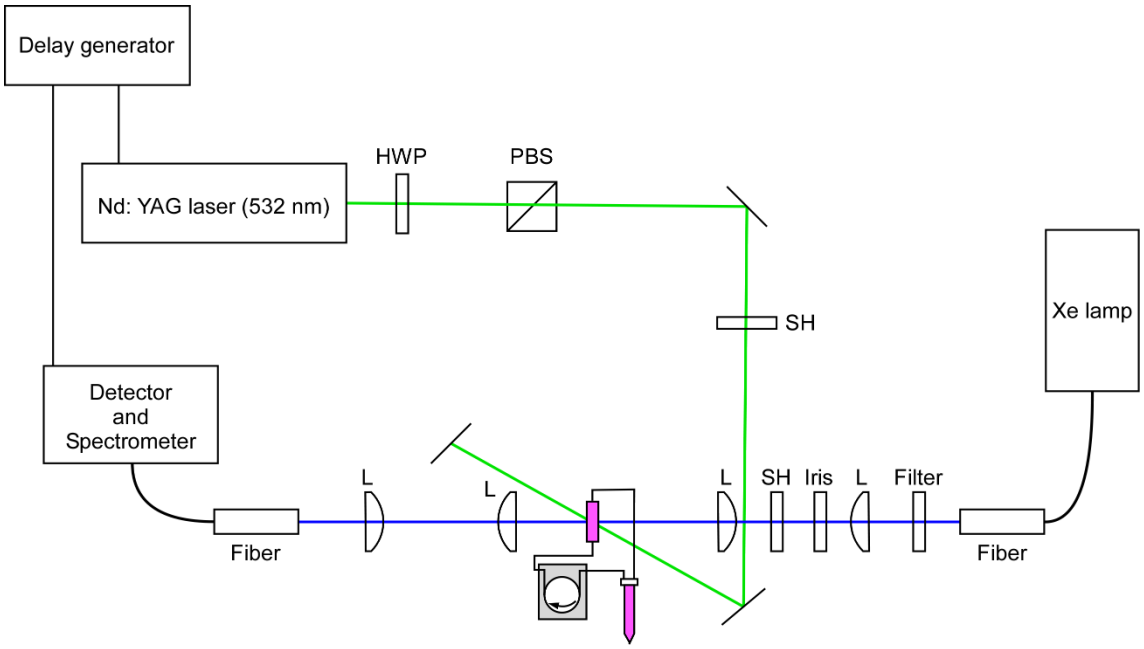

Figure 2-8. Layout of the laser-flash photolysis measurement system. The green and blue line represents the pump pulse and probe light, respectively. HWP = half wave plate, PBS = polarized beam splitter, L = lens, SH = mechanical shutter. The purple-colored figure is the sample rotating using peristaltic pump.

2.8 Visible Resonance Raman Measurement

In this study, the 532-nm excited resonance Raman (RR) measurements were carried out in order to investigate the structure of the retinal chromophore of KR2 or HeRs. The 532-nm probe light was the output of a single frequency CW diode pumped laser (Cobolt, 04-01 Samba). A layout of the measurement system is illustrated in Figure 2-9. For RR measurements, the sample solutions were circulated through a 1.5-mmϕ quartz flow cell with the flow rate of 15 mL/min on ice using the peristaltic pump or spun at 750 rpm using 10-mmϕ glass NMR tube at room temperature. The former is suitable to measure the sample having a long-lived photocycle such as HeRs but it needs a lot of sample solutions in order to circulate them. For the latter, although a sample volume of 1 mL is enough the spinning speed and the intensity of probe light should be carefully determined to avoid the photolyzed species. For the detailed conditions, see the experimental section in each protein.[1] The 90º Raman scattered light was collected and focused onto the entrance slit of a single spectrograph (HORIBA Jobin Yvon, iHR320). The spectrograph was equipped with an 1800-grooves/mm, 400-nm blazed grating. A short-cut dielectric filter (Asahi Spectra, LV0550) was set in front of the entrance slit of the spectrograph to eliminate the Rayleigh scattering and the reflection of the 532-nm probe light on the surface of the sample cell. The dispersed light was detected with a liquid nitrogen-cooled CCD camera (Roper Scientific, PyLoN: 400B_eXelon VISAR). In this apparatus, the spectral dispersion was 0.7 - 0.9 cm^{-1}/pixel on a liquid-nitrogen-cooled CCD camera. The spectrum of the buffer and emission background were subtracted from each RR spectrum. Figure 2-10 represents how the background emission was subtracted. Raman shifts were calibrated Raman bands of 2-propanol, ethanol, and acetone for the flow cell system and cyclohexane, toluene, and acetone for the spinning cell system. The calibration error was within 1 cm^{-1}.

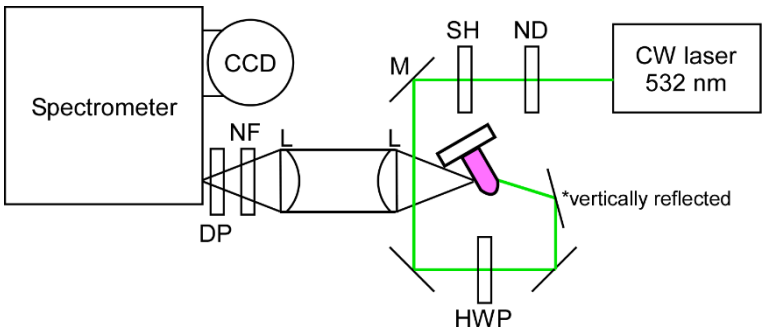

Figure 2-9. Layout of the visible RR measurement system. The green line represents the probe light. ND = neutral-density filter, SH = mechanical shatter, M = mirror, HWP = half wave plate, L = lens, NF = notch filter, DP = depolarizer. The purple-colored figure is the spinning sample cell. This spinning cell was replaced with the flow cell when HeRs were measured.

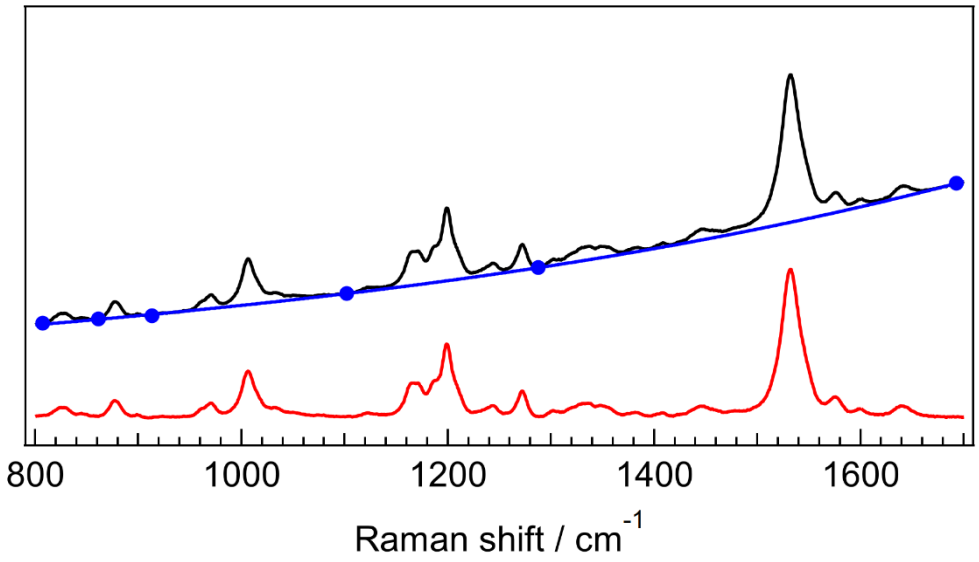

Figure 2-10. Baseline correction of the RR spectrum. Black trace represents the difference spectrum of DDM-solubilized KR2 with 100 mM NaCl. The blue circles are arbitrarily selected position where the Raman band is not observed. Blue trace is the baseline curve obtained by fitting with the 5th-degree polynomials function based on the selected coordinates. By subtracting the baseline curve from the black trance, we can obtain the baseline-corrected spectrum (red).

2.9 UV Resonance Raman Measurement

To obtain the structures and environments of aromatic amino acid side chains in proteins, the UV resonance Raman (UVRR) spectroscopy is one of the most useful technique. Here, a UV probe pulse at 233 nm (40 ns, 1 kHz) was used to measure the UVRR spectra of aromatic amino acids residues in KR2 and its mutant. The 233-nm probe pulse was the fourth harmonic of the output of an Nd: YLF-pumped Ti: sapphire laser (Photonics Industries, TU-L). The 135º Raman backscattered light from the sample was detected with a liquid nitrogen-cooled CCD camera (Roper Scientific, Spec-10: 400B/LN-SN-U) equipped with a single spectrograph (HORIBA Jobin Yvon, iHR550) with a 2400-grooves/mm, 400-nm blazed grating. To effectively remove the Rayleigh scattering light, the prism prefilter was constructed before the spectrograph. For UVRR measurement, the sample solution was circulated in a rectangular-shaped quartz cell having a cross-sectional area of 4 mm^2 (1 mm × 4 mm) using liquid transfer pump (Cole-Parmer Instrument Company, Masterflex Peristaltic Pump 6-600 RPM) and Teflon tube (Cole- Parmer Instrument Company, Masterflex L.S Peroxide-Cured Silicone Tubing, L/S 16, 25 ft). The circulated sample solution was chilled on ice in order to moderate damage by motor heat or UV irradiation. The flow rate was controlled by a speed controller and set to about 150 mL/min. Raman shifts were calibrated Raman bands of 2-propanol, ethanol, and acetone and the calibration error was within 1 cm^{-1}.

2.10 Time-Resolved UVRR Measurement

To study the conformational changes during light-induced ion pump by KR2, time-resolved UVRR measurements were carried out. Here, the 532-nm continuous light, which was the output of a single frequency CW diode pumped laser (Cobolt, 04-01 Samba) was combined as a pump beam to the above mentioned UVRR apparatus. The UV probe pulse and 532-nm pump beam were focused onto the rectangular-shaped quartz cell having a cross-sectional area of 4 mm^2 (1 mm × 4 mm). An actuator controllable by a stage controller (Opto Sigma, Mini-5D Actuator Controller) was installed to change the spatial irradiation position of the pump beam. A layout of the measurement system is illustrated in Figure 2-11. In this system, the delay times were determined by the distance between the UV probe pulse and the pump beam. A schematic diagram is shown in Figure 2-12 and 2-13. The time-resolution was determined by the flow rate and focused beamwidth. The beamwidth of the 532-nm pump beam was 200 μm (FWHM). When the flow rate was 150 mL/min and the rectangular-shaped quartz cell having a cross-sectional area of 4 mm^2 was used, the time-resolution could be calculated as 330 μs.

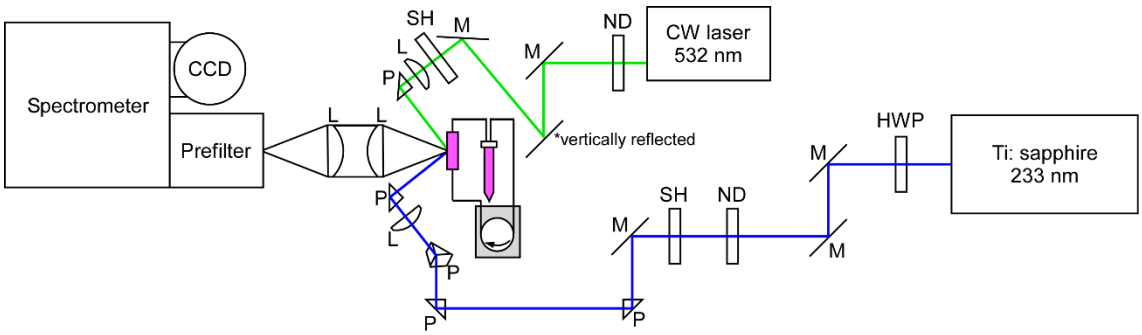

Figure 2-11. Layout of the time-resolved UVRR measurement system. The purple-colored figure is the sample rotating using peristaltic pump. HWP = half wave plate, M = mirror, SH = mechanical shutter, ND = neutral-density filter, P = prism.

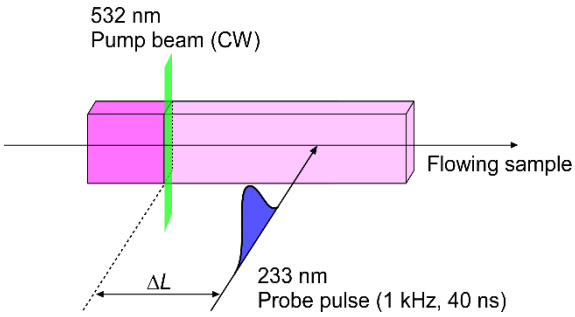

Figure 2-12. Rapid flow method for time-resolved measurement. The delay times were generated by changing the focused position of pump beam (green) using the actuator stage. The sample flow rate was set to be ~150 mL/min.

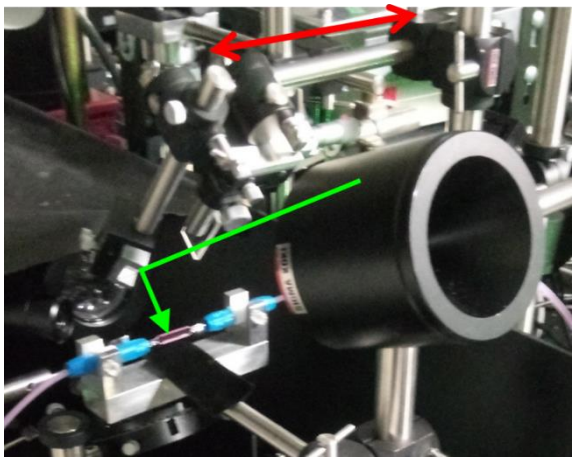

Figure 2-13. Enlarged view of pump beam path around the sample cell. The green arrow represents the pump beam. In this system, the cylindrical lens and the prism move in the red direction by the actuator connecting stage so that the position irradiated with the pump beam changes.

The delay times were set to -0.5, -0.1, 0.1, 0.2, 0.5, 1, 2, 3, 4, and 5 ms. Raman signals were collected for three 20 second exposures. The sequence of delay times was chosen to be random in each scan. In addition to the time-resolved spectra (pump-probe spectra), pump-only, probe-only, and dark spectra were collected. In order to analyze the spectral components of the photoproducts, the pump-only spectrum was subtracted from the pump-probe spectrum of each delay time and the dark spectrum was subtracted from the probe-only spectrum, obtaining the "probe-with-photolysis" and the "probe-without-photolysis", respectively. After that, the probe-without-photolysis spectrum was subtracted from the probe-with-photolysis spectrum of each delay time so that we obtain the difference spectrum. For calculating the difference spectrum, the Raman intensity of the ~980 cm^{-1} band of sulfate ion was used as the internal intensity standard. By normalizing the Raman intensity of this band, we could correct the effects of self-absorption.

2.11 References

[1] Otomo, A., Mizuno, M., Singh, M., Shihoya, W., Inoue, K., Nureki, O., Beja, O., Kandori, H., and Mizutani, Y. (2018) Resonance Raman Investigation of the Chromophore Structure of Heliorhodopsins, *J. Phys. Chem. Lett. 9*, 6431-6436.

[2] Ono, H., Inoue, K., Abe-Yoshizumi, R., and Kandori, H. (2014) FTIR Spectroscopy of a Light-Driven Compatible Sodium Ion-proton Pumping Rhodopsin at 77 K, *J. Phys. Chem. B 118*, 4784-4792.

[3] Ito, S., Iwaki, M., Sugita, S., Abe-Yoshizumi, R., Iwata, T., Inoue, K., and Kandori, H. (2018) Unique Hydrogen Bonds in Membrane Protein Monitored by Whole Mid-IR ATR Spectroscopy in Aqueous Solution, *J. Phys. Chem. B 122*, 165-170.

[4] Kato, H. E., Inoue, K., Abe-Yoshizumi, R., Kato, Y., Ono, H., Konno, M., Hososhima, S., Ishizuka, T., Hoque, M. R., Kunitomo, H., Ito, J., Yoshizawa, S., Yamashita, K., Takemoto, M., Nishizawa, T., Taniguchi, R., Kogure, K., Maturana, A. D., Iino, Y., Yawo, H., Ishitani, R., Kandori, H., and Nureki, O. (2015) Structural Basis for Na^+ Transport Mechanism by a Light-Driven Na^+ Pump, *Nature 521*, 48-53.

[5] Inoue, K., Nomura, Y., and Kandori, H. (2016) Asymmetric Functional Conversion of Eubacterial Light-Driven Ion Pumps, *J. Biol. Chem. 291*, 9883-9893.

[6] Shionoya, T., Mizuno, M., Tsukamoto, T., Ikeda, K., Seki, H., Kojima, K., Shibata, M., Kawamura, I., Sudo, Y., and Mizutani, Y. (2018) High Thermal Stability of Oligomeric Assemblies of Thermophilic Rhodopsin in a Lipid Environment, *J. Phys. Chem. B 122*, 6945-6953.

[7] Hussain, S., Kinnebrew, M., Schonenbach, N. S., Aye, E., and Han, S. (2015) Functional Consequences of the Oligomeric Assembly of Proteorhodopsin, *J. Mol. Biol. 427*, 1278-1290.

[8] Dencher, N. A., and Heyn, M. P. (1978) Formation and Properties of Bacteriorhodopsin Monomers in the Non-ionic Detergents Octyl-β-$_D$-glucoside and Triton X-100, *FEBS Lett. 96*, 322-326.

[9] Ritchie, T. K., Grinkova, Y. V., Bayburt, T. H., Denisov, I. G., Zolnerciks, J. K., Atkins, W. M., and Sligar, S. G. (2009) Chapter 11 - Reconstitution of Membrane Proteins in Phospholipid Bilayer Nanodiscs, *Methods Enzymol. 464*, 211-231.

[10] Bayburt, T. H., and Sligar, S. G. (2010) Membrane Protein Assembly into Nanodiscs, *FEBS Lett. 584*, 1721-1727.

[11] Shibata, M., Inoue, K., Ikeda, K., Konno, M., Singh, M., Kataoka, C., Abe-Yoshizumi, R., Kandori, H., and Uchihashi, T. (2018) Oligomeric States of Microbial Rhodopsins Determined by High-speed Atomic Force Microscopy and Circular Dichroic Spectroscopy, *Sci. Rep. 8*, 8262.

[12] Inoue, K., Ono, H., Abe-Yoshizumi, R., Yoshizawa, S., Ito, H., Kogure, K., and Kandori, H. (2013) A light-Driven Sodium Ion Pump in Marine Bacteria, *Nat. Commun. 4*, 1678.

[13] Hasselbacher, C. A., Spudich, J. L., and Dewey, T. G. (1988) Circular Dichroism of Halorhodopsin: Comparison with Bacteriorhodopsin and Sensory Rhodopsin I, *Biochemistry 27*, 2540-2546.

[14] Muccio, D. D., and Cassim, J. Y. (1979) Interpretations of the Effects of pH on the Spectra of Purple Membrane, *J. Mol. Biol. 135*, 595-609.

[15] Tsukamoto, T., Kikukawa, T., Kurata, T., Jung, K. H., Kamo, N., and Demura, M. (2013) Salt Bridge in the Conserved His-Asp Cluster in Gloeobacter Rhodopsin Contributes to Trimer Formation, *FEBS Lett. 587*, 322-327.

[16] Kovalev, K., Polovinkin, V., Gushchin, I., Alekseev, A., Shevchenko, V., Borshchevskiy, V., Astashkin, R., Balandin, T., Bratanov, D., Vaganova, S., Popov, A., Chupin, V., Buldt, G., Bamberg, E., and Gordeliy, V. (2019) Structure and Mechanisms of Sodium-Pumping KR2 Rhodopsin, *Sci Adv 5*, eaav2671.

[17] Lozier, R. H., Bogomolni, R. A., and Stoeckenius, W. (1975) Bacteriorhodopsin: A Light-Driven Proton Pump in *Halobacterium Halobium*, *Biophys. J. 15*, 955-962.

CHAPTER 3. Allosteric Communication to the Retinal Chromophore upon Ion Binding in KR2

3.1 Abstract

Krokinobacter rhodopsin 2 (KR2) serves as a light-driven sodium ion pump in the presence of sodium ion and works as a proton pump in the presence of larger monovalent cations such as potassium ion, rubidium ion, and cesium ion. Recent crystallographic studies revealed that KR2 forms a pentamer and possesses an ion binding site at the subunit interface. It is assumed that sodium ion bound at this site is not transported but contributes to oligomeric stability. Since KR2 can convert its function in response to co-existing cation species, this ion binding site is likely to be involved in ion transport selectively. How sodium ion binding affects the structure of the retinal chromophore, which plays a crucial role in ion transport, remains poorly understood. Here, we observed the structure of the retinal chromophore under a wide range of cation concentrations using absorption and resonance Raman spectroscopy. The spectroscopic character of the retinal chromophore showed that not only sodium ion but also potassium ion binds to the ion binding site. We found that the conjugated π electron of the chromophore became delocalized or localized by sodium ion or potassium ion binding, respectively. In addition, the strength of the hydrogen bond formed between the Schiff base of the retinal chromophore and its counter-ion, Asp116, decreases upon both sodium ion and potassium ion binding. This effect was more pronounced in sodium ion. These results suggested that the cation binding at ion binding site induces the conformational change around the Schiff base. This allosteric communication between the Schiff base and ion binding site at the subunit interface likely increases the efficiency of sodium ion transport. The present study demonstrates the significance of sodium ion binding: even though sodium ion is not transported, binding regulates the structure around the Schiff base.

3.2 Introduction

Microbial rhodopsins use light energy to enable various biological functions, such as active[1-4] and passive[5] transport of ions and signal transduction[6-10] in microorganisms. An outstanding feature of microbial rhodopsins is their diverse functions, despite the fact that they share a heptahelical transmembrane motif and a retinal chromophore that acts as a photoreceptor. In all rhodopsins, the chromophore covalently binds to a conserved lysine residue in the seventh transmembrane helix (helix G) by forming a Schiff base. These commonalities mean that fine differences in structure and interactions on the common framework determine the specific function,[11] although a comprehensive understanding of the structure-function relationship of rhodopsins remains elusive, despite many studies.

Krokinobacter rhodopsin 2 (KR2) is distinctive in this respect.[12] KR2 works as a light-driven outward sodium ion pump in the presence of sodium ion. Interestingly, in the absence of sodium ion or lithium ion, KR2 pumps protons outwardly. This makes KR2 a good model for studying the structure-function relationship of microbial rhodopsins because we can examine how structural changes resulting from ion binding and/or changes of the solution environment convert its pumping function. To this end, the sodium ion-pumping and proton-pumping states of KR2 were characterized structurally and functionally using mutagenesis analysis,[13, 14] ultrafast spectroscopy,[15] FTIR,[16, 17] resonance Raman spectroscopy,[18] EPR spectroscopy,[19] solid-state NMR,[20, 21] and MD simulation.[22] Moreover, KR2 is attracting attention as an optogenetics tool,[23] further intensifying interest in understanding the molecular mechanism underlying ion pumping and functional conversion. However, the comprehensive understanding of the functional conversion has not been achieved.

X-ray crystallographic studies of KR2 provided novel insights into the protein structure.[23, 24] KR2 comprises seven transmembrane helices and a covalently bound retinal

chromophore and forms a pentameric structure in the lipid bilayer (Figure 3-1A). The retinal chromophore of KR2 forms a Schiff base with Lys255. Crystallographic and sequence data showed that Asp116 in the third transmembrane helix (helix C) is the counter-ion of the Schiff base, suggesting that Asp116 forms a hydrogen bond with the Schiff base in the unphotolyzed state. A structure of the photointermediate in sodium ion pumping was proposed following analysis of the crystal structure under acidic conditions which showed that the side chain of protonated Asp116 is flipped in the intermediate.[23] This structural change is likely indispensable for sodium ion pumping because the D116N mutant lacks proton pumping activity.[12] Moreover, recent solid-state NMR studies revealed that the mutation of His30 to Ala perturbs the interaction between the Schiff base and Asp116 and inhibits proton pumping activity.[20, 21] Consequently, it is highly possible that the interaction between the Schiff base and Asp116 is key to the ion pumping mechanism of KR2.

Another feature of KR2 revealed by the crystallographic study is the presence of ion binding site at the subunit interface (Figure 3-1B).[24] This binding site is composed of the Tyr25 side chain, the Thr83 and Phe86 backbone oxygens of one protomer, and the Asp102 side chain of the neighboring protomer. The functional analysis of D102N mutant, which lacks the ion binding ability, found that the biding sodium ion is not transportable.[23] And the fact that D102N also pumps sodium ion suggests that this binding sodium ion contributes to the thermal stability of the pentameric structure rather than the ion transport.[12, 23]

The effects of sodium ion binding on the KR2 structure have been investigated to date[20, 25, 26] but less is understood regarding the structural correlation between the ion binding site and the retinal chromophore, which is a key part of the ion pumping mechanism. In the present study, we investigated the structure of the retinal chromophore of KR2 under a wide range of cation concentrations, both under nanodisc-reconstituted and DDM-solubilized conditions, using visible

absorption spectroscopy and resonance Raman (RR) spectroscopy. RR spectra of microbial rhodopsins selectively probe the vibrational modes of the retinal chromophore and thus provide detailed structural information on the chromophore.[27-33] Firstly, we found that the solubilization of KR2 by DDM leads to the destabilization of the protein assembly at low cation concentration. And the spectroscopic feature clearly demonstrated not only sodium ion but also potassium ion binds to KR2. The conjugated π electron of the chromophore became delocalized or localized by sodium ion or potassium ion binding, respectively. Furthermore, the strength of the hydrogen bond formed between the Schiff base of the retinal chromophore and Asp116, decreases upon both sodium ion and potassium ion binding. This effect was more pronounced in sodium ion. These results suggested the cation binding induces the conformational change around the retinal chromophore, depending on the cation size. The binding of sodium ion or potassium ion likely affects the chromophore structure around the Schiff base region or the ionone ring region, respectively. This allosteric communication between the Schiff base and the ion binding site by binding of sodium ion probably increases the efficiency of sodium ion transport. Our results demonstrate the cation binding properties in KR2 and significant of sodium ion binding; even though sodium ion is not transported, binding regulates the structure around the Schiff base.

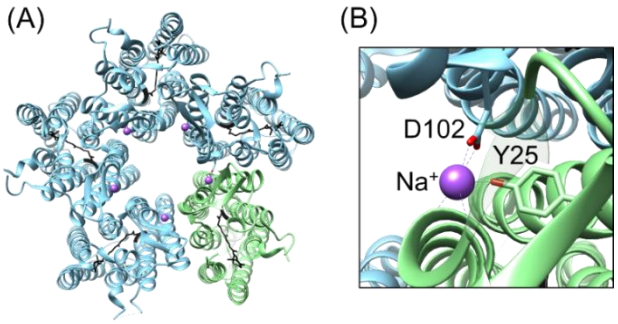

Figure 3-1. Crystallographic structure of KR2 (PDB: 4XTN). (A) Pentameric structure of KR2 viewed from the extracellular side. The light green chain represents one protomer and the cyan chains represent the other four protomers. The black sticks and purple spheres show the retinal chromophore and sodium ion, respectively. (B) Expanded view of the sodium ion binding site of KR2. Tyr25 and Asp102 constitute the binding site and are provided from two protomers adjacent to each other.

3.3 Materials and Methods

Sample Preparation

The wild-type KR2 and some KR2 mutants were prepared using the same method, as described in Chapter 2. Briefly, KR2 from *Krokinobacter eikastus* with a 6×His-tag at the C terminus was expressed in *Escherichia coli* C41 (DE3) strain, then induced with 1.0 mM isopropyl β-D-thiogalactopyranoside (IPTG) and supplemented with 10 μM all-*trans*-retinal (Toronto Research Chemicals, R240003) for 3 h at 37°C. The cells were disrupted by ultrasonication and the membrane fraction was collected by ultracentrifugation (109,000 × g, 1 h at 4°C). After homogenizing the pellets, the protein was solubilized with 1.5% *n*-dodecyl-β-$_D$-maltoside (DDM) (Dojindo, D316) in buffer containing 20 mM MES (pH 6.5), 300 mM NaCl, and 5 mM imidazole. The solution was loaded on a Co^{2+}-affinity column (GE Healthcare, HiTrap Talon) then eluted using a gradient of wash buffer (20 mM MES, pH 6.5) containing 300 mM NaCl, 50 mM imidazole, and 0.1% DDM and elution buffer (20 mM MES, pH 7.5) containing 500 mM imidazole and 0.1% DDM. The colored fractions were collected and loaded on an anion exchange column (GE Healthcare, HiTrap Q HP) and eluted using a gradient of wash buffer (50 mM Tris-HCl, pH 8.0) containing 0.1% DDM and elution buffer (50 mM Tris-HCl, pH 8.0) containing 1 M NaCl and 0.1% DDM.

In addition to the DDM-solubilized KR2, the nanodisc-reconstituted KR2 was used in this study. The manipulation of nanodisc-reconstituted KR2 is described in Chapter 2. Briefly, a mixture of phospholipids (asolectin from soybeans; Sigma-Aldrich, 10186987) and membrane scaffolding proteins (Sigma-Aldrich, MSP1E3D1) was used for reconstitution. Solubilized KR2 (0.6 mg) was mixed with 2.0 mg asolectin and 2.4 mg MSP1E3D1 by inverting at 4°C, then 50 mg Bio-beads SM-2 (Bio-Rad, 152-3920) were added to remove DDM from the sample.

Size Exclusion Chromatography (SEC)

About 20 μM KR2 in 50 mM Tris-HCl (pH 8.0) containing 0.1% DDM and 100 mM NaCl, KCl, or choline chloride were used for SEC experiments. Choline chloride was used to adjust the ionic strength of the solution. Samples were applied to a gel filtration column (GE Healthcare, HiPrep 26/60 Sephacryl S-300 HR). The flow rate was 1.5 mL/min. All SEC experiments were carried out at 4°C on an FPLC instrument (Akta, GE Healthcare). The concentration of the protein was monitored by absorbance at 280 nm.

Absorption and Circular Dichroism (CD) Spectroscopy

The methodology of absorption and CD spectroscopy was described in Chapter 2. Briefly, absorption spectra were obtained in the region of 250-700 nm at room temperature using a spectrophotometer (SHIMADZU, UV-3150). Samples were solutions of about 15 μM KR2 suspended in 50 mM Tris-HCl (pH 8.0) buffer containing 0.1% DDM and 0.05 - 1000 mM NaCl or KCl. The CD spectra were obtained in the region of 380-700 nm at 25 °C using a circular dichroism spectrometer (JASCO, J-720W). The quartz cuvette with an optical path length of 2 mm was used as the sample cell. Samples were solutions of about 15 μM nanodisc-reconstituted KR2 and 0.1% DDM-solubilized KR2 containing 100 mM NaCl or choline chloride.

Resonance Raman Spectroscopy

For RR measurements, the sample solutions containing 20 μM heliorhodopsins (HeR) in 50 mM Tris-HCl buffer at pH 8.0 with 10 mM NaCl, 300 mM Na_2SO_4, and 0.05% DDM were used. RR measurements of KR2 were performed as described in Chapter 2. Briefly, the 532-nm probe light from a single frequency CW DPSS laser (Cobolt, 04-01 Samba) was used. RR measurements were conducted by placing the sample solution in a 10 mmϕ glass NMR tube used as a spinning cell. The sample concentration was about 20 μM. The 90° Raman scattering was collected and focused onto the entrance slit of a single spectrograph (HORIBA Jobin Ybon,

iHR320). A short-cut dielectric filter (Asahi Spectra, LV0550) was used to eliminate Rayleigh scattering and reflection of the probe light from the cell surface. The dispersed light was detected with a liquid-nitrogen-cooled CCD camera (PyLon: 400BeX-VISAR, Roper Scientific). The spectrometer was calibrated using the Raman bands of acetone, cyclohexane, and toluene with a calibration error of ± 1 cm^{-1}.

We carefully examined the laser power and spinning rate of the sample cell to prevent spectral contributions due to the accumulation of long-lived intermediates in the laser irradiation volume (Figure S1). A probe laser power of 125 μW and a spinning rate of 750 rpm were found to be optimal.

3.4 Results

Cation Dependence of the Absorption Spectra.

Figure 3-2A shows the absorption maximum wavelength (λ_{max}) of the chromophore in KR2 reconstituted into nanodiscs plotted against cation concentration. An increase in sodium ion or potassium ion concentration above 10 mM resulted in a red and blue shift, respectively. On the other hand, there was no prominent shift was observed with cesium ion concentration. Figure 3-2B shows that the λ_{max} of KR2 solubilized with DDM responded significantly differently to cation concentration compared to nanodisc-reconstituted KR2. Increase in sodium ion concentration in the 1-10 mM range resulted in a blue shift, followed at higher concentrations by the red shift observed with nanodisc-reconstituted KR2. A similar blue shift was observed with potassium ion concentrations in the 1-10 mM range.

Each subunit of KR2 possesses one ion binding site at the subunit interface.[24] The dissociate constant of sodium ion bound to KR2 was estimated to be 11.4 mM.[12] Although the fewer data points in our plots made it difficult to calculate the dissociation constant, we concluded that the red shift or blue shift that occurred above 10 mM of sodium ion or potassium ion was due to the cation binding to ion binding site. The binding sodium ion to KR2 was reported by Inoue et al.[12] and confirmed by the crystal structure,[24] however, the binding ability of potassium ion was less understood.[26] On the other hand, our results clearly indicated that not only sodium ion but also potassium ion can bind to KR2.

The shift of λ_{max} occurred above 10 mM of cation concentration is common in both DDM-solubilized and nanodisc-reconstituted KR2. In contrast, the blue shift observed for 1–10 mM cation was specific to DDM-solubilized KR2, suggesting a difference in cation concentration-dependent structural change between the nanodisc-reconstituted and DDM-solubilized states.

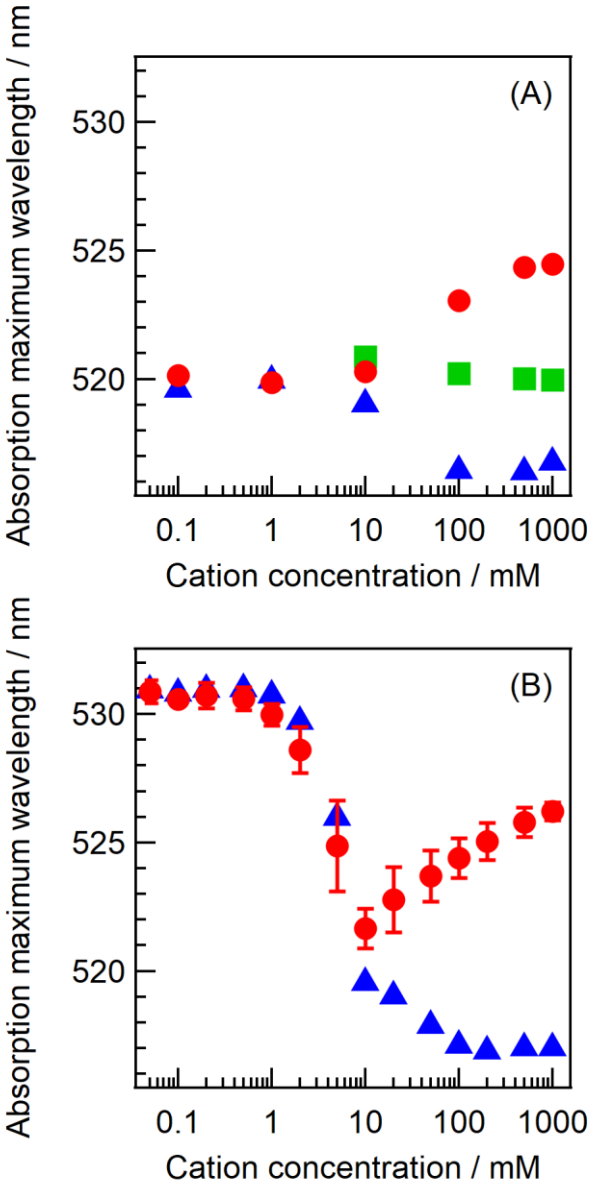

Figure 3-2. Cation concentration dependence of the absorption maximum wavelength of nanodisc-reconstituted KR2 (A) and DDM-solubilized KR2 (B). Red circles, blue triangles, and green square show the Na^+, K^+, and Cs^+ concentration dependence, respectively. The error bars represent the standard deviation. (*n*=3).

Cation Dependence of the Oligomeric State.

Cation concentration changes can affect the assembly states of oligomeric proteins. The molecular weights of protein/detergent assemblies of KR2 solubilized with DDM were examined by SEC measurements. Elution profiles are shown in Figure 3-3 for samples containing 100 mM sodium ion, potassium ion, or choline ion. We measured the SEC profile in the presence of choline ion as a control because choline ion is too bulky to bind to KR2 and only changes the ionic strength of the sample solution. KR2 in buffer containing either sodium ion or potassium ion eluted with a smaller volume of elution buffer than KR2 in buffer containing choline ion, suggesting that the molecular weight of KR2 in the choline-containing buffer is smaller than KR2 in sodium ion or potassium ion-containing buffer.

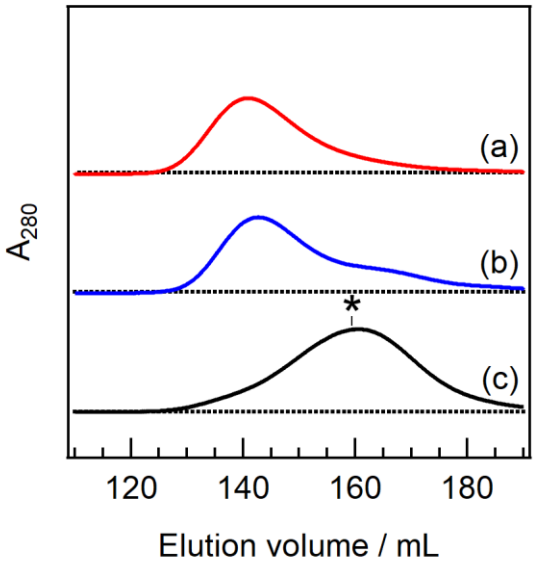

Figure 3-3. SEC chromatograms of DDM-solubilized KR2 at 4°C for samples containing 100 mM Na^+ (trace a), K^+ (trace b), and choline ion (trace c). An asterisk represents the calculated elution volume of *Natronomonas pharaonis* halorhodopsin F150W mutant, which forms a monomer.

We next compared the present results with those of previous studies because it is not straightforward to estimate the molecular weight of solubilized membrane proteins by SEC due to complexation of the protein with detergent. Shibata et al. suggested that DDM-solubilized KR2 forms a pentamer at 50 mM sodium ion, based on high-speed atomic force microscopy and CD spectroscopy data.[34] Thus, KR2 forms a pentamer in the presence of 100 mM sodium ion, as shown in Figure 3-3, trace a. The similarity of trace b to trace a in Figure 3-3 shows that KR2 also forms a pentamer in 100 mM potassium ion. We determined the molecular weight of KR2 in 100 mM choline ion to be 131.4 kD, similar to that of *Natronomonas pharaonis* halorhodopsin F150W mutant (136.2 kD, Figure 3-3, asterisk),[35] which forms a monomer, indicating that KR2 in 100 mM choline ion is monomeric. These results showed that KR2 becomes a monomer in the absence of sodium ion or potassium ion. Therefore, it is highly likely that the red shift observed for DDM-solubilized KR2 in Figure 3-2B results from the oligomeric transition from pentamer to monomer. It was consistent with the results of circular dichroism spectroscopy as shown in Figure S3-2. Importantly, since cation binding to the ion binding site at the subunit interface occurs at cation concentrations over 10 mM, oligomeric transition below 10 mM of cations is not associated with the ion binding site identified previously. It should be noted that the K_d of the oligomeric transition was not estimated because the absorption shift was irreversible.

Cation Dependence of the Resonance Raman Spectra.

We investigated the effects of cation binding on the chromophore structure of KR2 by measuring RR spectra using 532-nm probe light. Figure 3-4A shows RR spectra of nanodisc-reconstituted KR2, where traces a and b are the spectra obtained in the presence of 100 mM sodium ion and potassium ion, respectively. Trace c is the difference spectrum of trace a and trace b. Figure 3-4B shows the RR spectra of DDM-solubilized KR2, where traces a, b and c are the spectra obtained in the presence of 100 mM sodium ion, potassium ion and choline ion, respectively. The DDM-solubilized KR2 RR spectra have higher S/N ratios than the nanodisc-reconstituted KR2 spectra because the nanodisc-reconstituted KR2 samples were slightly turbid. The RR bands in Figure 3-4 were assigned based on the vibrational assignments of the RR bands of the retinal chromophore in *Halobacterium salinarum* bacteriorhodopsin.[36, 37]

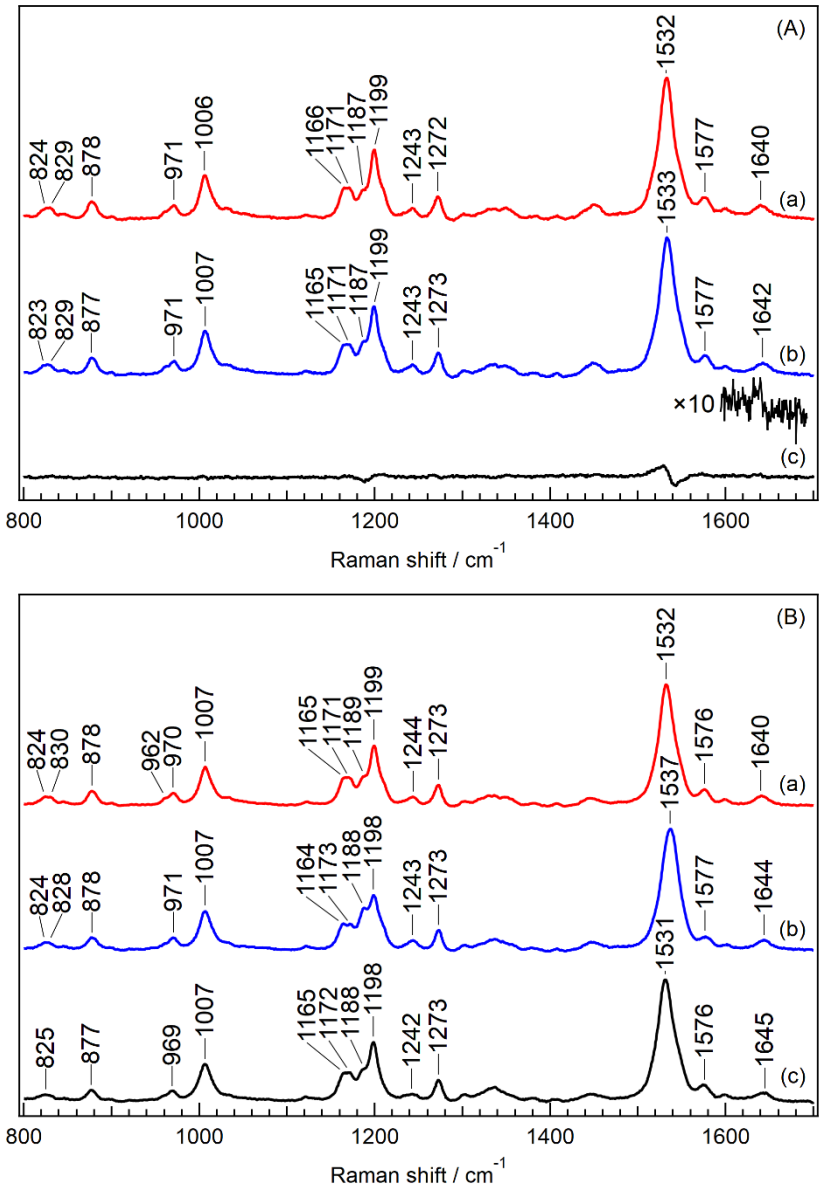

Figure 3-4. RR spectra of nanodisc-reconstituted (A) and DDM-solubilized KR2 (B). In panel A, traces a and b are of samples containing 100 mM Na^+ and K^+, respectively. Trace c is the difference spectrum of traces a and b [(a)-(b)]. In panel B, traces a, b, and c are of samples containing 100 mM Na^+, K^+, and choline ion, respectively. The accumulation time for obtaining each trace was 60 min. The spectrum of the buffer and the emission background were subtracted.

The strongest bands, at 1530–1540 cm^{-1}, in Figure 3-4 are due to the C=C stretching mode [ν(C=C)] of the polyene chain. The ν(C=C) frequency was distinguishable between in the presence of 100 mM sodium ion and potassium ion. The trace c in Figure 3-4A exhibits a derivative-like feature around 1530 cm^{-1}, showing that the ν(C=C) frequencies are different between trace a and b. In Figure 3-5, panels A and B show the cation concentration dependence of the ν(C=C) frequency for nanodisc-reconstituted KR2 and DDM-solubilized KR2, respectively. The frequency of this band is affected by localization of the π electrons on the polyene chain and thus there is an inverse relationship between the frequency and the λ_{max}.[38] For both nanodisc-reconstituted KR2 and DDM-solubilized KR2, the ν(C=C) frequency correlated with the maximum wavelength shown in Figure 3-2. Since the shift in maximum wavelength observed at cation concentrations above 10 mM is due to cation binding, as described above, sodium ion binding or potassium ion binding to the subunit interface caused the ν(C=C) frequency to decrease or increase, respectively. These results suggest that sodium ion binding leads to delocalization of the π electrons on the retinal chromophore. In contrast, the localization of the π electrons was induced by potassium ion binding. Thus, the conformational change of the ion binding site at the subunit interface is coupled with the change in conformation around the retinal chromophore, depending on the cation size.

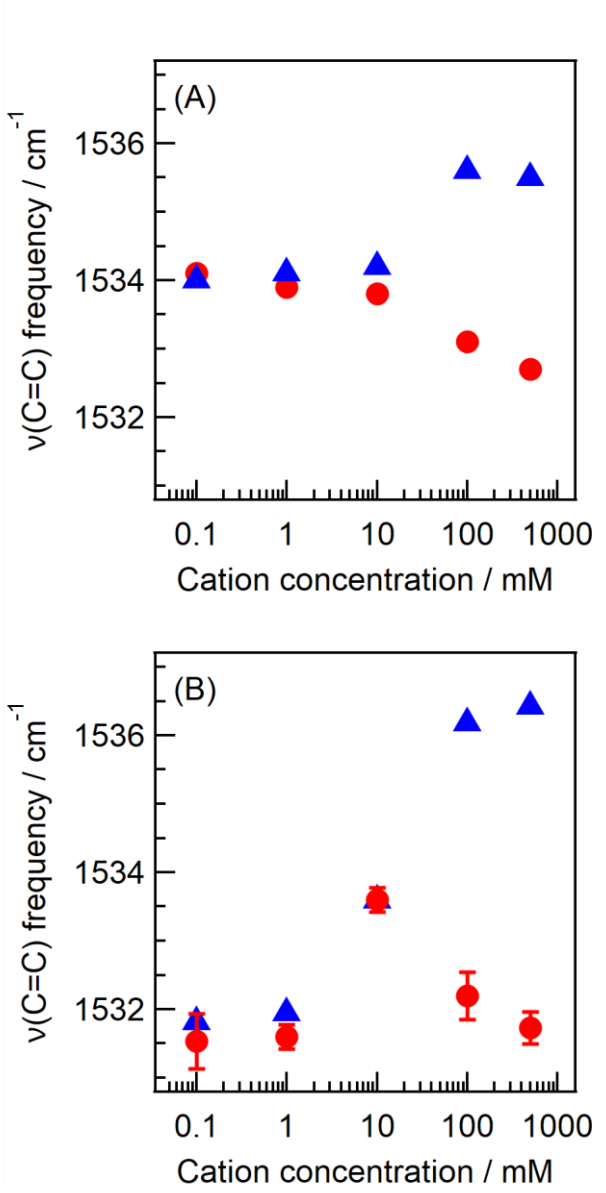

Figure 3-5. Cation concentration dependence of the v(C=C) frequency of nanodisc-reconstituted KR2 (A) and DDM-solubilized KR2 (B). Red circles and blue triangles show the Na^+ and K^+ concentration dependence, respectively. The error bars represent the standard deviation (*n*=3).

The small bands at 1640–1645 cm^{-1} in Figure 3-4 are assigned to the C=N stretching [ν(C=N)] mode. Since the C=N stretching mode is strongly coupled with the N-H rocking mode, the frequency of the ν(C=N) band contains useful information regarding the Schiff base. In Figure 3-6, panels A and B show the cation concentration dependence of the ν(C=N) frequency for nanodisc-reconstituted KR2 and DDM-solubilized KR2, respectively. The frequency decreases as the sodium ion and potassium ion concentrations increase, but the magnitude of the frequency shift is much smaller for potassium ion. Curve fitting the frequency against sodium ion concentration to the Hill equation provided microscopic dissociation constants of 16.5±1.9 and 16.9±6.2 mM for nanodisc-reconstituted and DDM-solubilized KR2, respectively. These values are close to the dissociation constant reported previously (11.4 mM). These results show that the downshift of the ν(C=N) band is due to sodium ion binding to the subunit interface, suggesting that sodium ion binding to KR2 weakens the hydrogen-bond strength of the protonated Schiff base. This interpretation is supported by the sodium ion dependence of the ν(C=C) and ν(C=N) frequencies for D102N mutant (Figure S3-3), which cannot bind sodium ion.[23] In this mutant, neither the ν(C=C) band nor the ν(C=N) band shifted as the sodium ion concentration was increased.

Solubilization of KR2 with DDM affected not only the stability of oligomer formation but also potassium ion binding affinity at the subunit interface. The ν(C=N) frequency was independent of potassium ion concentration in DDM-solubilized KR2 but showed a small downshift upon increasing potassium ion concentration in nanodisc-reconstituted KR2. The fact that the binding of potassium ion resulted in the upshift of the ν(C=C) frequency and the small downshift of the ν(C=N) frequency suggested that the potassium ion binding altered the chromophore structure on the ionone ring side is more responsive than the Schiff base, which is different from the case of sodium ion binding. The addition of cesium ion resulted in no ν(C=N)

frequency shift, as shown in Figure 3-6A, indicating that the binding affinity depends on the size of the ion.

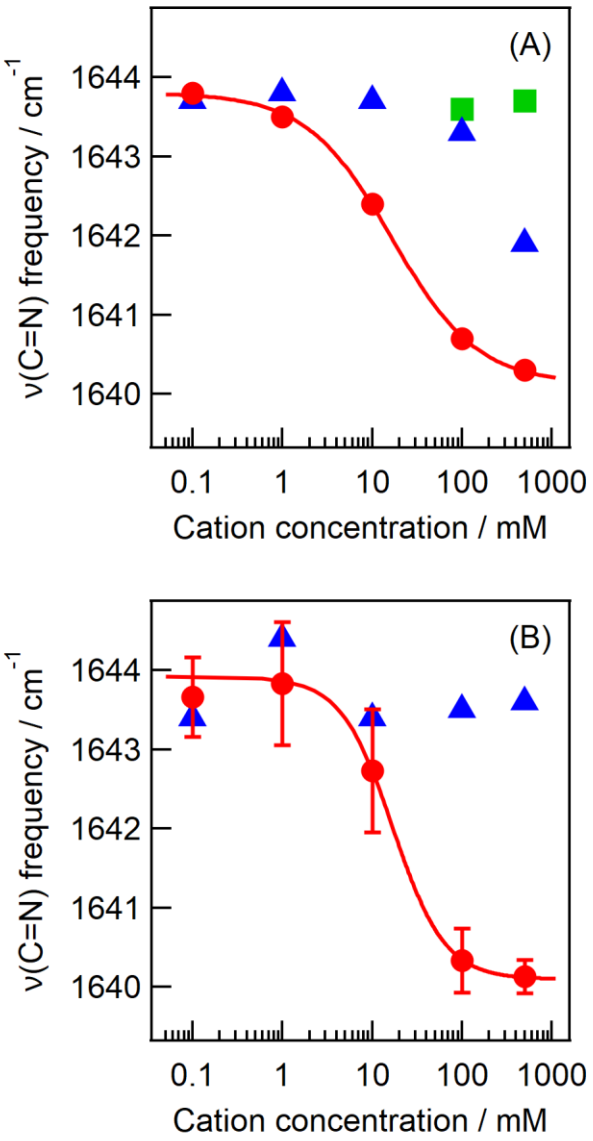

Figure 3-6. Cation concentration dependence of the ν(C=N) frequency of nanodisc-reconstituted KR2 (A) and DDM-solubilized KR2 (B). Red circles, blue triangles, and green squares show the Na^+, K^+, and Cs^+ concentration dependence, respectively. Red lines are the best-fit with the Hill equation for Na^+ (see text). The observed frequencies were well expressed by the following parameters: microscopic dissociation constant, 16.5±1.9 mM (A) and 16.9±6.2 mM (B); Hill coefficient, 0.9±0.1 (A) and 1.5±0.8 (B). The error bars represent the standard deviation (n=3).

Figure 3-7 shows RR spectra of DDM-solubilized KR2 in H_2O and D_2O buffer. Deuteration decreased the ν(C=N) frequency for all conditions, showing that the Schiff base is protonated in unphotolyzed KR2. The magnitude of the deuteration shift of the ν(C=N) band provides information regarding the strength of the hydrogen-bond between the Schiff base and its counter-ion, with a larger deuteration shift indicative of higher hydrogen-bond strength.[39] The magnitudes of the shifts in the presence of sodium ion, potassium ion, and choline ion are 21, 26, and 27 cm^{-1} respectively. Therefore, the hydrogen bond is stronger in the proton pumping condition than in the sodium ion pumping condition, consistent with a recent study using NMR and FTIR spectroscopy.[26]

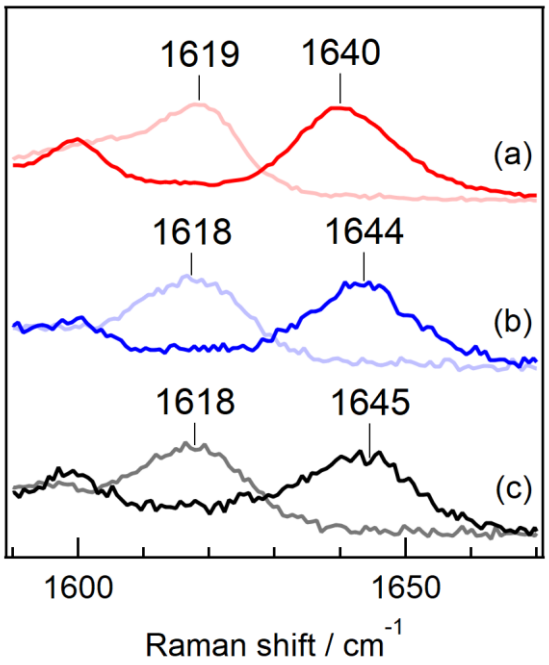

Figure 3-7. Expanded views of RR spectra in the ν(C=N) region (1590–1670 cm^{-1}) of DDM-solubilized KR2. Traces a, b, and c are for samples containing 100 mM Na^+, K^+, and choline ion, respectively. Darker and lighter traces show the spectra obtained in H_2O and in D_2O buffer, respectively.

Hydrogen out-of-plane (HOOP) wagging and methyl group rocking were observed in the 800–1000 cm^{-1} region, as shown in Figure 3-4. The band intensity of the HOOP mode is enhanced when the polyene chain is distorted.[40] The spectral features of the HOOP bands were almost the same in the presence of either 100 mM sodium ion or potassium ion as shown in Figure 3-8, suggesting that the distortion of the retinal chromophore of KR2 is not affected by sodium ion binding at the interface.

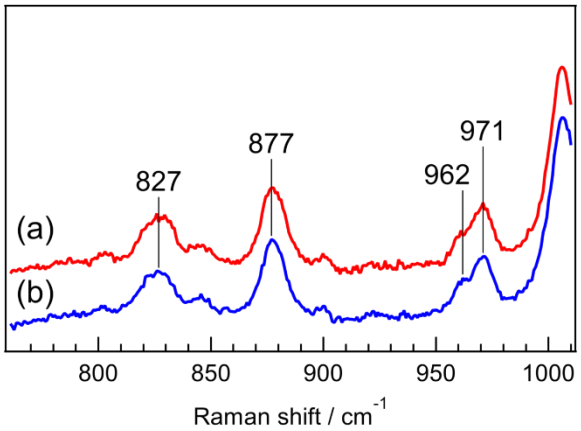

Figure 3-8. Expanded views of the resonance Raman spectra of KR2 in the region of hydrogen out-of-plane wagging vibrations. Traces a and b show spectra of nanodisc-reconstituted KR2 in buffer containing 100 mM Na^+ and K^+, respectively.

3.5 Discussion

Structural Changes in the Retinal Chromophore upon Cation Binding.

To date, although the binding of potassium ion to KR2 has been suggested,[19, 26] there is no conclusive data. Our data clearly indicated that both sodium ion and potassium ion can bind to KR2. The sodium ion binding to the subunit interface induced a red shift in the visible absorption band and a downshift of the ν(C=C) band. In contrast, the potassium ion binding leads to a blue shift in the visible absorption band and an upshift of the ν(C=C) band. These results suggested that the π electrons in the retinal chromophore become more delocalized or localized upon sodium ion binding or potassium ion binding, respectively. This delocalization and localization may be caused by changes in the planarity of the polyene chain and/or its interaction with the surroundings. The protonated Schiff base is the most effective interaction site on the retinal chromophore. The downshift of the ν(C=N) band demonstrated that the hydrogen bond to the Schiff base is weakened upon sodium binding, leading to delocalization of the π electrons due to the destabilization of the positive charge. On the other hand, the ν(C=N) band showed a slight downshift, suggesting that the localization of the π electrons by the binding of potassium ion was likely caused by a mechanism different from the case of sodium ion binding. Namely, the binding of potassium ion may affect the structure of the ionone ring side of the retinal chromophore rather than the Schiff base. The HOOP band is a good indicator of distortion in the polyene chain of the chromophore. Expanded views of the HOOP region of the RR spectra show that the HOOP intensity is essentially independent of the coexisting cation species (Figure 3-8). It is highly likely that delocalization or localization of the π electrons upon sodium ion or potassium ion binding is induced not by the distortion of the polyene chain. Therefore, the cation binding to the subunit interface alters the structure around the retinal chromophore; the binding of sodium ion increases the distance between the protonated Schiff base and its counter-ion, Asp116, and the binding of

potassium ion alters the conformation around not the Schiff base but the ionone ring side.

Allosteric Communication between the Chromophore Schiff Base and the Ion Binding Site.

The protonated Schiff base is 24 Å away from the ion binding site. Interestingly, Asp102 in the ion binding site locates in the B-C loop and is close to the N-terminal edge of helix C, which contains Asp116 (Figure 3-9). Therefore, the binding of sodium ion to the subunit interface can transmit information to the retinal chromophore through structural changes in helix C, such as helix tilting and/or twisting. It has been reported that the presence of sodium ion in the binding site affects the conformation of helix C.[20, 21, 24]

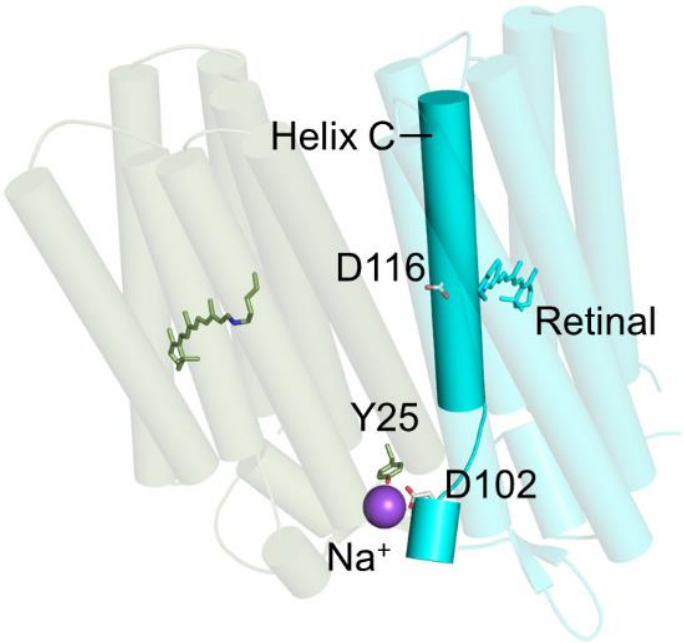

Figure 3-9. The retinal chromophore and the Na^+ binding site in KR2 structure (PDB: 4XTO). Two protomers which form one Na^+ binding site are shown.

Asp102 is provided from the adjoining subunit to form the ion binding site at the interface and thus the formation of the ion binding site requires oligomer formation. Therefore, oligomer formation must induce structural changes at the subunit interface. Previous studies also suggested that changes in the subunit interface affect the chromophore structure.[20, 21, 25] Kaur et al. reported that the interaction between the chromophore and Asp116 changes when His30, which is located close to the ion binding site, is replaced with alanine.[20, 21] The transmission of conformational change between subunits has been reported in other light-driven ion pumping proteins and thus appears to be a common feature of microbial rhodopsins, which generally form oligomers.[35, 41]

The previous study reported that D102N mutant cannot bind sodium but can transport sodium ion, although with lower efficiency than WT.[23] We assumed that the conformational change induced by binding of sodium ion observed in the present study increases pumping efficiency but is not indispensable for sodium ion transport. Since KR2 competes for the sodium ion-pumping and proton-pumping state,[42] the decreased sodium ion pumping efficiency of D102N mutant may be due to an increase in proton pumping efficiency, which can partially cancel the pH change observed in assay measurements. The destination of the proton transferred to Asp116 from the Schiff base is different in the two functional conditions: it returns to the Schiff base in the sodium ion pumping condition but is transferred from the Schiff base to an amino acid residue closer to the extracellular side in the proton pumping state. Thus, KR2 contains a mechanism to switch the destination of the proton, perhaps through a conformational change in helix C. It was previously proposed that flipping of the Asp116 side chain is essential for sodium ion pumping.[23] Replacement of Ser70 with alanine converts the sodium ion pump into a proton pump, probably due to destabilization of the flipped Asp116.[23] Accordingly, when the conformational change in helix C alters the relative position of Asp116 to Ser70 upon sodium ion dissociation from the

binding site, this change likely destabilizes the flipped Asp116 and hence affects sodium ion pumping activity.

The structural changes around the retinal chromophore due to the binding of potassium ion can also be explained by the conformational change in helix C. In helix C, Trp113 residue exists, which forms a retinal binding site composed of some bulky amino acid residues. The surface of Trp113 faces to the middle position of the retinal chromophore as shown in Figure S3-4A. Therefore, the structural change of Trp113 probably affects the π electron on the retinal chromophore. The absorption spectra of W113F mutant did not show the large shift between in the presence of 100 mM sodium ion and potassium ion as shown in Figure S3-4B. It is assumed that the binding of potassium ion to the ion binding site induces structural changes of helix C, involving the structural change of Trp113, different from that of sodium ion due to the ion size. Our data implied that cesium ion cannot bind to KR2 (Figure 3-2A, 3-6A), is consistent with previous research.[12] These results suggest that the ion binding site and its structural changes are affected by the size of the ion and are optimized for the size of sodium ion.

Differences Between the DDM-Solubilized and the Nanodisc-Reconstituted States.

The present data showed that DDM-stabilized KR2 is monomeric at low sodium ion concentrations while nanodisc-reconstituted KR2 is an oligomer. Solubilization of membrane proteins with detergents alters the stability of the protein.[31, 43, 44] DDM-solubilized thermophilus rhodopsin (TR) was reported to be monomerized upon heating but remain oligomeric in lipid-reconstituted conditions.[31] Protein structural changes induced by monomerization affect the chromophore structure although the chromophore is completely surrounded by the helices.

At low cation concentration, both sodium ion and potassium are absent from the binding site but these cations in the vicinity of the binding site can weaken electrostatic repulsion between Asp102 and Tyr25, thus stabilizing the pentamer form. Choline ion is too bulky to approach the

binding site and thus KR2 is in the monomer form even at 100 mM choline ion. It is possible that the negative charge in the head group of the phospholipid can weaken electrostatic repulsion, thereby stabilizing the pentamer form of KR2.

The present data illustrate the need for care when preparing KR2 samples solubilized using DDM, a condition often used for spectroscopic studies of microbial rhodopsins. We discovered that the dissociation of sodium ion or potassium ion from DDM-solubilized KR2 reduces the stability of the pentameric form. It should be pointed out that the sodium ion-free pentamer form is present only in a narrow range of sodium ion concentrations. Consequently, the oligomerization state of detergent-solubilized KR2 may not reflect that of physiological conditions, although detergent solubilization has the advantage of providing optically clear samples.

3.6 Conclusion

The present study revealed allosteric communication between the ion binding site and the retinal chromophore of KR2 using visible absorption and RR spectroscopy. Sodium ion binding in the binding site at the subunit interface resulted in the weakening of the hydrogen bond to the protonated Schiff base and delocalization of π conjugation in the polyene chain of the chromophore. Although the sodium ion binding site at the subunit interface locates 24 Å from the Schiff base of the chromophore, the two sites are allosterically coupled to each other, possibly through the tilting and/or twisting of helix C. The functional significance of this allosteric communication will be elucidated by examining the effect of sodium ion binding on the chromophore structure of the intermediates in the KR2 photocycle. Recently, we succeeded in observing RR spectra of all the intermediates of KR2 and elucidated the structural evolution of the chromophore in the sodium ion-binding state.[45] Further work is ongoing in our laboratory to elucidate the structural evolution of intermediates in the absence of sodium ion. In addition to the sodium ion, our results demonstrated that potassium ion binds to KR2 and induced the structural changes through helix C. However, due to the difference of the ion size, this structural change involves the motion of Trp113 resulted in the conformational change of the chromophore ring rather than the Schiff base, different from that the case of sodium ion. In the present study, we revealed that the oligomeric stability of KR2 is affected by solubilization with DDM, highlighting the need to pay attention to possible changes in the structure and properties of KR2 induced by solubilization. The present study demonstrated the significance of binding of sodium ion to KR2: even though sodium ion is not transported, binding regulates the structure of the Schiff base and stabilizes the oligomeric structure.

3.7 Supporting Information

Dependence of the Probe Power on the RR Intensities of KR2.

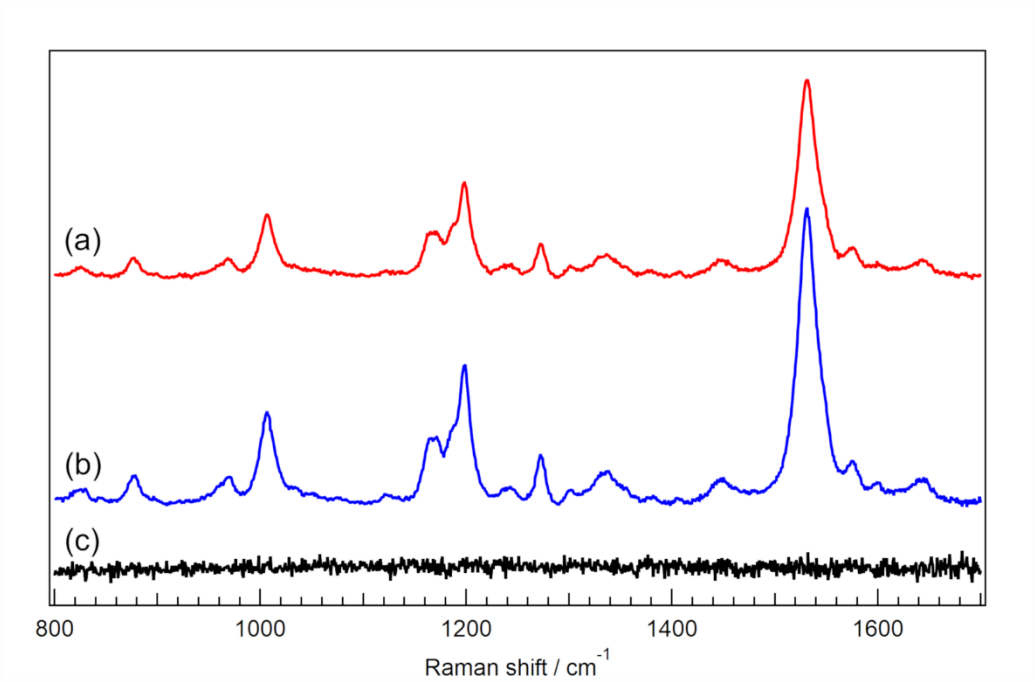

Figure S3-1. Probe power dependence of the resonance Raman spectra of KR2 in the presence of 100 mM Na^+. Traces a and b show the spectra measured using probe powers of 90 and 125 μW, respectively. Trace c shows the difference spectrum obtained by ((trace a) – 0.67) × (trace b). The amplitude of trace c is magnified three times. Since there are no bands in trace c, a probe power of 125 μW is sufficiently weak to prevent contamination of the spectra by undesirable photoproducts.

CD Spectra of DDM-Solubilized and Nanodisc-Reconstituted KR2.

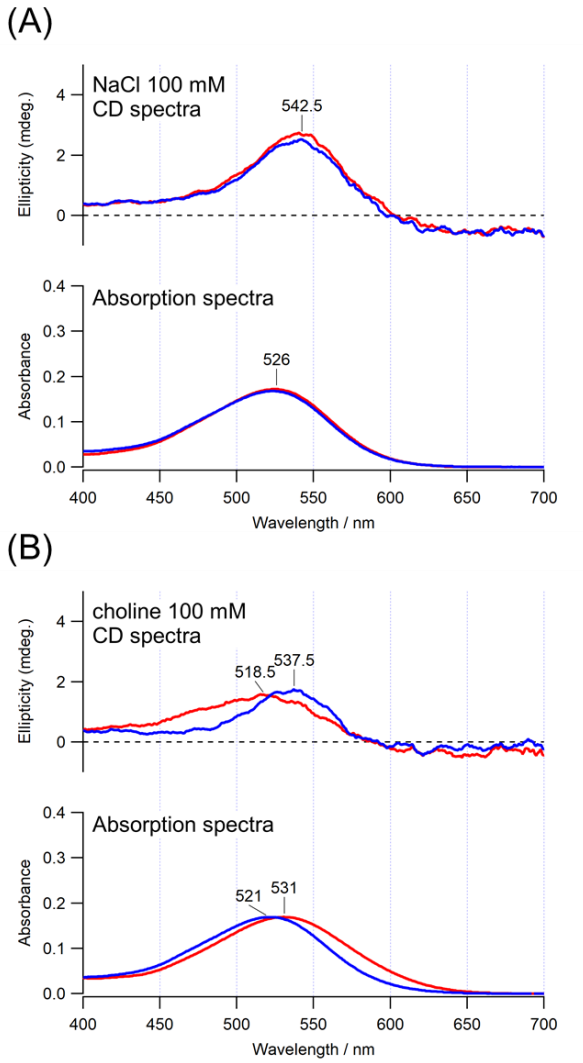

Figure S3-2. CD spectra and absorption spectra of KR2 in the presence of 100 mM Na^+ (A) or 100 mM choline ion (B). Red and blue traces represent the results of DDM-solubilized KR2 and nanodisc-reconstituted KR2, respectively. In the presence of 100 mM Na^+, both CD spectra and absorption spectra were almost the same between DDM-solubilized and nanodisc-reconstituted KR2. The peak position and the bandwidth of CD spectra was higher and narrower than that of absorption spectra. They could be explained the sum of the negative intrinsic band and the split positive band due to the exciton coupling between the chromophores. Thus, these results indicated that KR2 forms pentamer in the presence of 100 mM Na^+ both DDM-solubilized and nanodisc-reconstituted KR2. In the case of 100 mM choline ion, a similar behavior was observed in nanodisc-reconstituted KR2, indicating KR2 forms a pentamer. In contrast, the peak position blue-shifted and the no prominent changes in the bandwidth in DDM-solubilized KR2. It was likely demonstrated that KR2 forms monomer only when it was solubilized with DDM in the absence of Na^+.

Na^+ Concentration Dependence of the *ν*(C=C) and *ν*(C=N) Frequencies of D102N Mutant.

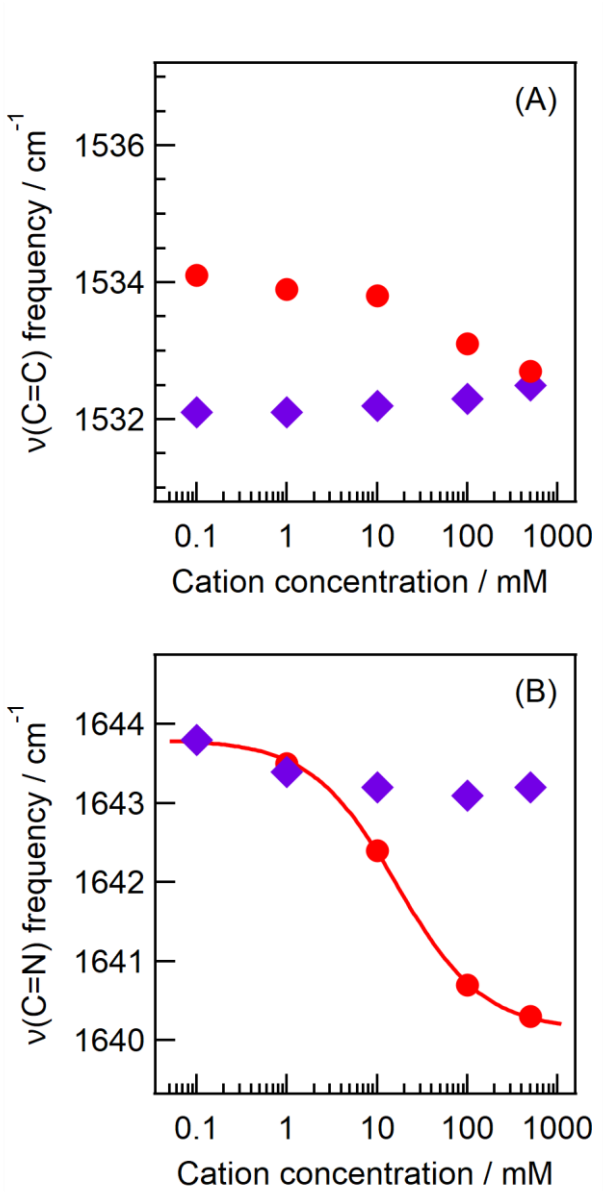

Figure S3-3 Na^+ concentration dependence of the v(C=C) (A) and v(C=N) frequencies (B) of nanodisc-reconstituted KR2. Red circles and purple diamonds show the dependences of wildtype KR2 and the D102N mutant, respectively. The red line is the best-fit with the Na^+ Hill equation (see text). The observed v(C=N) frequency was well expressed by the following parameters: microscopic dissociation constant, 16.5±1.9 mM; Hill coefficient, 0.9±0.1.

Location of Trp113 and Absorption Spectra of W113F Mutant and WT.

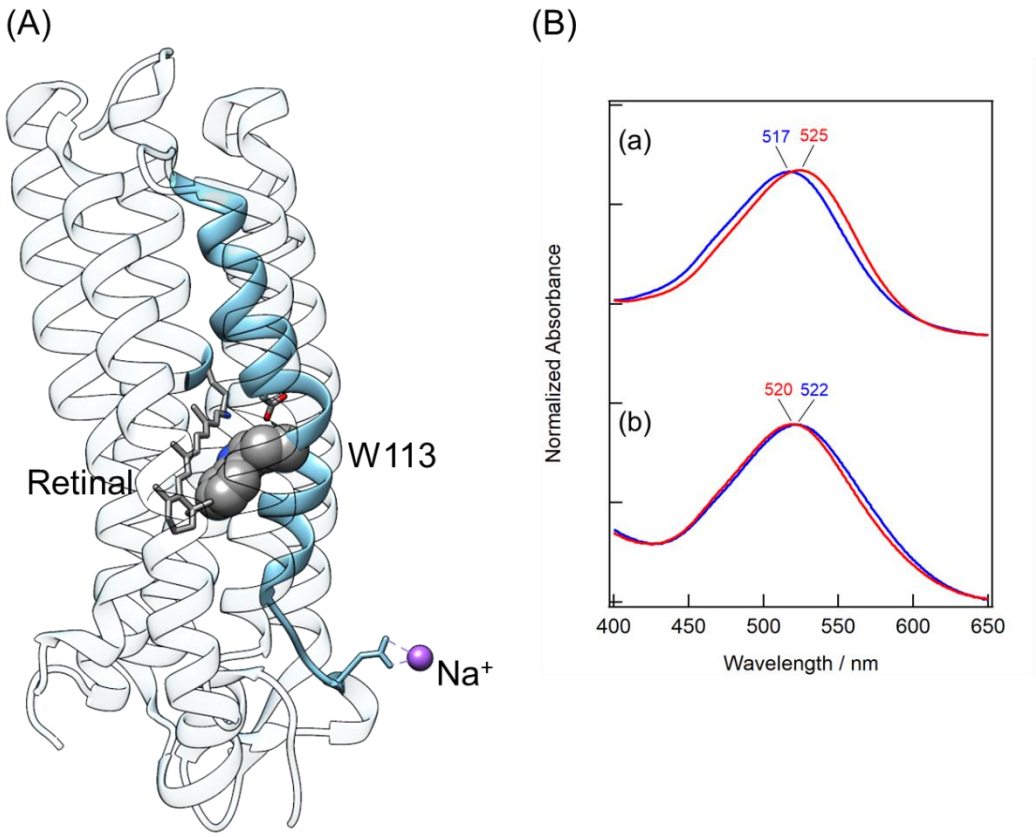

Figure S3-4 (A) Crystal structure of KR2 (PDB: 4XTN). The skyblue helix represents the helix C (Asp102-Leu127). The sphere molecule is Trp113 located in the helix C. It indicates that the movement of helix C by binding potassium ion at the ion binding site affects structure not only the Schiff base. (B) The absorption spectra of WT (a) and W113F mutant (b) mutant. Red and blue trances show the absorption spectra in the presence of 100 mM Na^+ and potassium ion, respectively. In WT (a), the absorption band showed 8 nm blue shift by replacing sodium ion with potassium ion. In contrast, W113F mutant showed 2 nm red shift by replacing them. These results imply that Trp113 is an important residue that greatly influence the conjugated π electron of the retinal chromophore, depending on the ion size.

3.8 References

[1] Engelhard, C., Chizhov, I., Siebert, F., and Engelhard, M. (2018) Microbial Halorhodopsins: Light-Driven Chloride Pumps, *Chem. Rev. 118*, 10629-10645.

[2] Kandori, H., Inoue, K., and Tsunoda, S. P. (2018) Light-Driven Sodium-Pumping Rhodopsin: A New Concept of Active Transport, *Chem. Rev. 118*, 10646-10658.

[3] Lanyi, J. K. (2004) Bacteriorhodopsin, *Annu. Rev. Physiol. 66*, 665-688.

[4] Govorunova, E. G., Sineshchekov, O. A., Li, H., and Spudich, J. L. (2017) Microbial Rhodopsins: Diversity, Mechanisms, and Optogenetic Applications, *Annu. Rev. Biochem 86*, 845-872.

[5] Schneider, F., Grimm, C., and Hegemann, P. (2015) Biophysics of Channelrhodopsin, *Annu. Rev. Biophys. 44*, 167-186.

[6] Spudich, J. L., and Luecke, H. (2002) Sensory Rhodopsin II: Functional Insights from Structure, *Curr. Opin. Struct. Biol. 12*, 540-546.

[7] Hoff, W. D., Jung, K. H., and Spudich, J. L. (1997) Molecular Mechanism of Photosignaling by Archaeal Sensory Rhodopsins, *Annu. Rev. Biophys. Biomol. Struct. 26*, 223-258.

[8] Luck, M., Mathes, T., Bruun, S., Fudim, R., Hagedorn, R., Tran Nguyen, T. M., Kateriya, S., Kennis, J. T., Hildebrandt, P., and Hegemann, P. (2012) A Photochromic Histidine Kinase Rhodopsin (HKR1) that is Bimodally Switched by Ultraviolet and Blue Light, *J. Biol. Chem. 287*, 40083-40090.

[9] Scheib, U., Stehfest, K., Gee, C. E., Körschen, H. G., Fudim, R., Oertner, T. G., and Hegemann, P. (2015) The Rhodopsin–guanylyl Cyclase of the Aquatic Fungus *Blastocladiella Emersonii* Enables Fast Optical Control of cGMP Signaling, *Science Signaling 8*, rs8-rs8.

[10] Yoshida, K., Tsunoda, S. P., Brown, L. S., and Kandori, H. (2017) A Unique Choanoflagellate Enzyme Rhodopsin Exhibits Light-Dependent Cyclic Nucleotide Phosphodiesterase Activity, *J. Biol. Chem. 292*, 7531-7541.

[11] Ernst, O. P., Lodowski, D. T., Elstner, M., Hegemann, P., Brown, L. S., and Kandori, H. (2014) Microbial and Animal Rhodopsins: Structures, Functions, and Molecular Mechanisms, *Chem. Rev. 114*, 126-163.

[12] Inoue, K., Ono, H., Abe-Yoshizumi, R., Yoshizawa, S., Ito, H., Kogure, K., and Kandori, H. (2013) A Light-driven Sodium Ion Pump in Marine Bacteria, *Nat. Commun. 4*, 1678.

[13] Inoue, K., Nomura, Y., and Kandori, H. (2016) Asymmetric Functional Conversion of Eubacterial Light-Driven Ion Pumps, *J. Biol. Chem. 291*, 9883-9893.

[14] Mamedov, A. M., Bertsova, Y. V., Anashkin, V. A., Mamedov, M. D., Baykov, A. A., and Bogachev, A. V. (2018) Identification of the Key Determinant of the Transport Promiscuity in Na^+-Translocating Rhodopsins, *Biochem. Biophys. Res. Commun. 499*, 600-604.

[15] Tahara, S., Takeuchi, S., Abe-Yoshizumi, R., Inoue, K., Ohtani, H., Kandori, H., and Tahara, T. (2018) Origin of the Reactive and Nonreactive Excited States in the Primary Reaction of Rhodopsins: pH Dependence of Femtosecond Absorption of Light-Driven Sodium Ion Pump Rhodopsin KR2, *J. Phys. Chem. B 122*, 4784-4792.

[16] Chen, H. F., Inoue, K., Ono, H., Abe-Yoshizumi, R., Wada, A., and Kandori, H. (2018) Time-resolved FTIR Study of Light-Driven Sodium Pump Rhodopsins, *Phys. Chem. Chem. Phys. 20*, 17694-17704.

[17] Ono, H., Inoue, K., Abe-Yoshizumi, R., and Kandori, H. (2014) FTIR Spectroscopy of a Light-Driven Compatible Sodium Ion-Proton Pumping Rhodopsin at 77 K, *J. Phys. Chem. B 118*, 4784-4792.

[18] Kajimoto, K., Kikukawa, T., Nakashima, H., Yamaryo, H., Saito, Y., Fujisawa, T., Demura, M., and Unno, M. (2017) Transient Resonance Raman Spectroscopy of a Light-Driven Sodium-Ion-Pump Rhodopsin from Indibacter alkaliphilus, *J. Phys. Chem. B 121*, 4431-4437.

[19] da Silva, G. F., Goblirsch, B. R., Tsai, A. L., and Spudich, J. L. (2015) Cation-Specific Conformations in a Dual-Function Ion-Pumping Microbial Rhodopsin, *Biochemistry 54*, 3950-3959.

[20] Kaur, J., Kriebel, C. N., Eberhardt, P., Jakdetchai, O., Leeder, A. J., Weber, I., Brown, L. J., Brown, R. C. D., Becker-Baldus, J., Bamann, C., Wachtveitl, J., and Glaubitz, C. (2018) Solid-state NMR Analysis of the Sodium Pump *Krokinobacter* Rhodopsin 2 and Its H30A Mutant, *J. Struct. Biol. 206*, 55-65.

[21] Shigeta, A., Ito, S., Kaneko, R., Tomida, S., Inoue, K., Kandori, H., and Kawamura, I. (2018) Long-Distance Perturbation on Schiff Base-Counterion Interactions by His30 and the Extracellular Na^+-Binding Site in *Krokinobacter* Rhodopsin 2, *Phys. Chem. Chem. Phys. 20*, 8450-8455.

[22] Suomivuori, C. M., Gamiz-Hernandez, A. P., Sundholm, D., and Kaila, V. R. I. (2017) Energetics and Dynamics of a Light-Driven Sodium-Pumping Rhodopsin, *Proc. Natl. Acad. Sci. U. S. A. 114*, 7043-7048.

[23] Kato, H. E., Inoue, K., Abe-Yoshizumi, R., Kato, Y., Ono, H., Konno, M., Hososhima, S., Ishizuka, T., Hoque, M. R., Kunitomo, H., Ito, J., Yoshizawa, S., Yamashita, K., Takemoto, M., Nishizawa, T., Taniguchi, R., Kogure, K., Maturana, A. D., Iino, Y., Yawo, H., Ishitani, R., Kandori, H., and Nureki, O. (2015) Structural Basis for Na^+ Transport Mechanism by a Light-Driven Na^+ Pump, *Nature 521*, 48-53.

[24] Gushchin, I., Shevchenko, V., Polovinkin, V., Kovalev, K., Alekseev, A., Round, E., Borshchevskiy, V., Balandin, T., Popov, A., Gensch, T., Fahlke, C., Bamann, C., Willbold, D., Buldt, G., Bamberg, E., and Gordeliy, V. (2015) Crystal Structure of a Light-Driven

Sodium Pump, *Nat. Struct. Mol. Biol. 22*, 390-395.

[25] Hontani, Y., Inoue, K., Kloz, M., Kato, Y., Kandori, H., and Kennis, J. T. (2016) The Photochemistry of Sodium Ion Pump Rhodopsin Observed by Watermarked Femto- to Submillisecond Stimulated Raman Spectroscopy, *Phys. Chem. Chem. Phys. 18*, 24729-24736.

[26] Ito, S., Iwaki, M., Sugita, S., Abe-Yoshizumi, R., Iwata, T., Inoue, K., and Kandori, H. (2018) Unique Hydrogen Bonds in Membrane Protein Monitored by Whole Mid-IR ATR Spectroscopy in Aqueous Solution, *J. Phys. Chem. B 122*, 165-170.

[27] Smith, S. O., Myers, A. B., Pardoen, J. A., Winkel, C., Mulder, P. P., Lugtenburg, J., and Mathies, R. (1984) Determination of Retinal Schiff Base Configuration in Bacteriorhodopsin, *Proc. Natl. Acad. Sci. U. S. A. 81*, 2055-2059.

[28] Maeda, A., Ogurusu, T., Yoshizawa, T., and Kitagawa, T. (1985) Resonance Raman Study on Binding of Chloride to the Chromophore of Halorhodopsin, *Biochemistry 24*, 2517-2521.

[29] Gellini, C., Luttenberg, B., Sydor, J., Engelhard, M., and Hildebrandt, P. (2000) Resonance Raman Spectroscopy of Sensory Rhodopsin II from *Natronobacterium pharaonis*, *FEBS Lett. 472*, 263-266.

[30] Niho, A., Yoshizawa, S., Tsukamoto, T., Kurihara, M., Tahara, S., Nakajima, Y., Mizuno, M., Kuramochi, H., Tahara, T., Mizutani, Y., and Sudo, Y. (2017) Demonstration of a Light-Driven SO_4^{2-} Transporter and Its Spectroscopic Characteristics, *J. Am. Chem. Soc. 139*, 4376-4389.

[31] Shionoya, T., Mizuno, M., Tsukamoto, T., Ikeda, K., Seki, H., Kojima, K., Shibata, M., Kawamura, I., Sudo, Y., and Mizutani, Y. (2018) High Thermal Stability of Oligomeric Assemblies of Thermophilic Rhodopsin in a Lipid Environment, *J. Phys. Chem. B 122*, 6945-6953.

[32] Mizuno, M., Nakajima, A., Kandori, H., and Mizutani, Y. (2018) Structural Evolution of a Retinal Chromophore in the Photocycle of Halorhodopsin from *Natronobacterium pharaonis*, *J. Phys. Chem. A 122*, 2411-2423.

[33] Otomo, A., Mizuno, M., Singh, M., Shihoya, W., Inoue, K., Nureki, O., Beja, O., Kandori, H., and Mizutani, Y. (2018) Resonance Raman Investigation of the Chromophore Structure of Heliorhodopsins, *J. Phys. Chem. Lett. 9*, 6431-6436.

[34] Shibata, M., Inoue, K., Ikeda, K., Konno, M., Singh, M., Kataoka, C., Abe-Yoshizumi, R., Kandori, H., and Uchihashi, T. (2018) Oligomeric States of Microbial Rhodopsins Determined by High-Speed Atomic Force Microscopy and Circular Dichroic Spectroscopy, *Sci. Rep. 8*, 8262.

[35] Tsukamoto, T., Kikukawa, T., Kurata, T., Jung, K. H., Kamo, N., and Demura, M. (2013) Salt Bridge in the Conserved His-Asp Cluster in Gloeobacter Rhodopsin Contributes to

Trimer Formation, *FEBS Lett. 587*, 322-327.

[36] Smith, S. O., Braiman, M. S., Myers, A. B., Pardoen, J. A., Courtin, J. M. L., Winkel, C., Lugtenburg, J., and Mathies, R. A. (1987) Vibrational Analysis of the All-*trans*-retinal Chromophore in Light-Adapted Bacteriorhodopsin, *J. Am. Chem. Soc. 109*, 3108-3125.

[37] Smith, S. O., Pardoen, J. A., Lugtenburg, J., and Mathies, R. A. (1987) Vibrational Analysis of the 13-*cis*-Retinal Chromophore in Dark-Adapted Bacteriorhodopsin, *J. Phys. Chem. 91*, 804-819.

[38] Aton, B., Doukas, A. G., Callender, R. H., Becher, B., and Ebrey, T. G. (1977) Resonance Raman Studies of the Purple Membrane, *Biochemistry 16*, 2995-2999.

[39] Baasov, T., Friedman, N., and Sheves, M. (1987) Factors Affecting the C = N Stretching in Protonated Retinal Schiff Base: A Model Study for Bacteriorhodopsin and Visual Pigments, *Biochemistry 26*, 3210-3217.

[40] Eyring, G., Curry, B., Broek, A., Lugtenburg, J., and Mathies, R. (1982) Assignment and Interpretation of Hydrogen Out-of-plane Vibrations in the Resonance Raman Spectra of Rhodopsin and Bathorhodopsin, *Biochemistry 21*, 384-393.

[41] Ran, T., Ozorowski, G., Gao, Y., Sineshchekov, O. A., Wang, W., Spudich, J. L., and Luecke, H. (2013) Cross-Protomer Interaction with the Photoactive Site in Oligomeric Proteorhodopsin Complexes, *Acta Crystallogr. D Biol. Crystallogr. 69*, 1965-1980.

[42] Kato, Y., Inoue, K., and Kandori, H. (2015) Kinetic Analysis of H^+-Na^+ Selectivity in a Light-Driven Na^+-Pumping Rhodopsin, *J. Phys. Chem. Lett. 6*, 5111-5115.

[43] Hussain, S., Kinnebrew, M., Schonenbach, N. S., Aye, E., and Han, S. (2015) Functional Consequences of the Oligomeric Assembly of Proteorhodopsin, *J. Mol. Biol. 427*, 1278-1290.

[44] Dencher, N. A., and Heyn, M. P. (1978) Formation and Properties of Bacteriorhodopsin Monomers in the Non-Ionic Detergents Octyl-β-$_D$-glucoside and Triton X-100, *FEBS Lett. 96*, 322-326.

[45] Nishimura, N., Mizuno, M., Kandori, H., and Mizutani, Y. (2019) Distortion and a Strong Hydrogen Bond in the Retinal Chromophore Enable Sodium-Ion Transport by the Sodium-Ion Pump KR2, *J. Phys. Chem. B 123*, 3430-3440.

CHAPTER 4. Dynamics of Protein Moiety Induced by the Chromophore Isomerization of KR2

4.1. Abstract

Krokinobacter rhodopsin 2 (KR2) is the first discovered light-driven sodium ion pump rhodopsin. The photoisomerization of the retinal chromophore induces protein structural changes for the transport of sodium ion through some photointermediates. In KR2, the uptake and release of sodium ion occur in the rise and decay of the O intermediate based on the kinetics study of the retinal chromophore. However, the protein structural change in the O intermediate has been less understood. Here we show that the Trp215 and Tyr222 are located at helix F undergo the structural change in the O intermediate using time-resolved ultraviolet resonance Raman (UVRR) spectroscopy. We found that the decrease of the hydrophobicity and alternation of the orientation of Trp215 side chain. Furthermore, we found that the dihedral angle of Tyr222 between the hydroxyl group and the benzene ring changes in the O intermediate. Our results suggest that these structural changes are accompanied by the forming of the transient channel, which connects the protein inside to the cytoplasmic or extracellular side. We have shown in the present study that time-resolved UVRR spectroscopy is useful to elucidate the mechanism of ion transport by rhodopsins.

4.2. Introduction

Light-driven ion pump is one of the major function in microbial rhodopsins.[1-3] The active transport of a specific ion generates an electrochemical potential for ATP synthesis and is achieved by a series of the protein structural change, called photocycle, induced by the photoisomerization of the retinal chromophore from all-*trans* to 13-*cis*. It is important for the elucidation of the ion transport mechanism by rhodopsins to reveal the protein structural change during the transport an ion. With the recent progress in metagenomics analysis, many rhodopsins have been discovered that transport various types of ions,[4-6] indicating the comprehensive understanding of the mechanism for ion transport in various rhodopsins is needed.

Krokinobacter rhodopsin 2 (KR2) is the first discovered light-driven sodium ion pump rhodopsin.[4] Prior to the discovery of KR2, rhodopsin was thought not to transport cations other than a proton, so the sodium-ion transport mechanism by KR2 has affected much attention. Spectroscopic and crystallographic studies revealed that the unphotolyzed KR2 has no sodium ion binding site inside the protein.[4, 7, 8] It means that in order to transport sodium ion, the uptake and release of sodium ion should be carried out during the photocycle. The time-resolved absorption spectroscopy revealed that KR2 shows some photointermediates called K, L, M, and O intermediate having a distinct absorption maximum wavelength as shown in Figure 4-1.[4] Tahara et al. demonstrated that the generation of the K intermediate occurs at 500 fs, which is faster than that of bacteriorhodopsin.[9] Recent time-resolved resonance Raman and IR spectroscopy revealed that the K and L intermediate possess a protonated Schiff base and subsequently deprotonation occurs at the M intermediate.[10-12] The L and M intermediate are equilibrium for each other.[4, 13] In the O intermediate, the Schiff base is reprotonated and back to the unphotolyzed state with thermal-isomerization of the retinal chromophore.

In KR2, it is believed that the transient sodium ion binding site composed of Asp251 is

created in the O intermediate.[4, 14, 15] Kato et al. demonstrated that the appearance of the O intermediate is significantly affected by the sodium ion concentrations, indicating the uptake and release of sodium ion occur in the rise and decay of the O population, respectively.[16] Because the electrostatic repulsion between sodium ion and the protonated Schiff base must be avoided,[7] the proton transfer and uptake of sodium ion should be correlated. The sodium ion is then hydrated and excreted out of the protein. As we have seen above, the sodium ion transport pathway is well investigated based on the structural changes around the retinal chromophore. However, in contrast to the retinal chromophore, the structural changes in the protein moiety have been less understood.

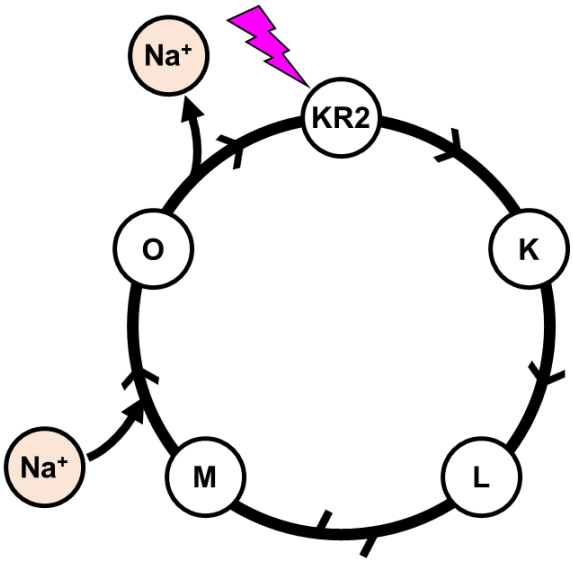

Figure 4-1. Photocycle scheme of KR2. KR2 shows some photointermediates, K, L, M, and O, which is the name of retinal chromophore in each photointermediate.

Here, we conducted time-resolved ultraviolet resonance Raman (UVRR) spectroscopy in the millisecond time scale to investigate the protein structural changes during the sodium-ion transport. The 233-nm excitation enables us to selectively observe resonantly enhanced Raman mode of tryptophan (Trp) and tyrosine (Tyr) residues in the protein.[17] The observed RR spectra demonstrated that the hydrophobic interaction of Trp residues decreases and the orientation of the side chain of Tyr residues changes in the O intermediate. By using the mutants which Trp215 and Tyr222 are replaced with phenylalanine, we could extract the spectral changes seen in wild-type (WT) KR2. These results indicate that the transient channels, which connects the protein inside to the cytoplasmic side and to the extracellular side are created during the M-to-O and O-to-KR2 transitions, respectively. The fact that Trp215 and Tyr222 are located on the same helix (helix F) implies that the helix F movement may play an important role in creating transient channels in order to transport sodium ion.

4.3. Material and Methods

Sample Preparation

Wild-type KR2, W215F, and Y222F mutants with a 6 × His-tag at the C terminus were expressed in *Escherichia* coli C41 (DE3) strain and purified as described in Chapter 2.1 and 3. Briefly, the His-tagged recombinant KR2 was purified using Co^{2+}-affinity column (GE Healthcare, HiTrap Talon) and an anion exchange column (GE Healthcare, HiTrap Q HP). The purity of the recombinant KR2 was confirmed by SDS-PAGE. A protein concentration of 20 μM of KR2 suspended in 50 mM Tris-HCl (pH 8.0) buffer containing 0.1% DDM, 10 mM NaCl, and 300 mM Na_2SO_4 was used for transient absorption spectroscopy measurements and UV resonance Raman measurements.

Measurement of Ion Transport Activity in *E. coli.*

Light-driven ion transport assay in *E. coli.* was conducted, see Chapter 2. Briefly, 4 mL of the KR2-expressed *E. coli* (C41) culture medium were collected into the 15 mL tube. They were washed three times with 10 mM NaCl, 300 mM Na_2SO_4, and 5% (w/v) sucrose solution and then suspended in the same solution. The 7.5 mL of cell suspension was illuminated using Xe lump (Asahi Spectra Co., Ltd. MAX-303) through a band-pass filter (Opto Sigma, Y48) and cold filter (Opto Sigma, CLDF-50S) at 20°C for 2.5 minutes. The light-induced pH changes were monitored with a pH meter (Horiba, F-72). After illuminating Xe lump, the sample was incubated in darkness for 10 minutes until the pH fluctuation stabilizes. Then 2.5 μL of 30 mM CCCP dissolved in dimethyl sulfoxide was added and measurements were repeated under the same conditions.

Absorption Spectroscopy

The methodology of absorption spectroscopy was described in Chapter 2. Briefly, absorption spectra were obtained in the region of 200-700 nm at room temperature using a

spectrophotometer (SHIMADZU, UV-3150). Samples were solutions of about 20 μM KR2 suspended in 50 mM Tris-HCl (pH 8.0) buffer containing 0.1% DDM, 10 mM NaCl, and 300 mM Na_2SO_4, which is used as an internal intensity standard. The quartz cuvette with an optical path length of 2 mm residues as the sample cell.

Transient Absorption Spectroscopy

The details of the transient absorption apparatus were described in Chapter 2. In this study, to obtain the time-resolved absorption spectra, 532 nm pulse beam (0.5 or 10 Hz, 7 ns) and continuous white light were utilized as a pump and probe light, respectively. The pump and probe lights were focused on the sample cell and data were collected by the multichannel spectrophotometer with an image intensifier (Hamamatsu Photonics, PMA-12 C1002901). Here, about 20 μM of KR2 was circulated by the peristaltic pump (ATTO, Bio-Minipump AC-2120). The sample volume was about 15 mL. For the sample cell, a rectangular-shaped quartz cell having a cross-sectional area of 4 mm^2 (1 mm × 4 mm) was used. The flow rate and the repetition frequency was 9.55 mL/min and 10 Hz for obtaining < 1 ms time region, and 0.162 mL/min and 0.5 Hz for obtaining > 1 ms time region.

Resonance Raman Spectroscopy

To obtain the RR spectra of the retinal chromophore, visible RR spectroscopy was carried out. The setup and condition were almost the same as shown in Chapter 3. In brief, the 532-nm probe light from a single frequency CW DPSS laser (Cobolt, 04-01 Samba) was used to excite the protein sample. For RR measurement, 20 μM of the sample in 50 mM Tris-HCl (pH 8.0) buffer containing 0.1% DDM and 100 mM NaCl was in a 10 mmϕ glass NMR tube used as a spinning cell. The spinning speed and the laser power were set to 750 rpm and 80 μW, respectively. The 90° Raman scattering was collected and focused onto the entrance slit of a single spectrograph (HORIBA Jobin Ybon, iHR320). A short-cut dielectric filter (Asahi Spectra,

LV0550) was used to eliminate Rayleigh scattering and reflection of the probe light from the cell surface. The dispersed light was detected with a liquid-nitrogen-cooled CCD camera (PyLon: 400BeX-VISAR, Roper Scientific). The spectrometer was calibrated using the Raman bands of acetone, toluene, and cyclohexane with a calibration error of ± 1 cm^{-1}.

For time-resolved UVRR measurements, 20 μM of KR2 suspended in 50 mM Tris-HCl (pH 8.0) buffer containing 0.1% DDM, 10 mM NaCl, and 300 mM Na_2SO_4 was used. The methodology was shown in Chapter 2. Here, the 233-nm probe pulse (40 ns, 1 kHz) and the 532-nm continuous light used as a pump beam were combined. The laser power at the sample position was 0.6 μJ and 300 mW for the probe pulse and the pump beam, respectively. The 135° Raman backscattered light from the sample was detected with a liquid N_2-cooled CCD camera (Roper Scientific, Spec-10: 400B/LN-SN-U) equipped with a single spectrograph (HORIBA Jobin Yvon, iHR550) with a 2400-grooves/mm, 400-nm blazed grating. To effectively remove the Rayleigh scattering light, the prism prefilter was constructed before the spectrograph. The UV pulse and the 532-nm CW laser light were focused onto the rectangular-shaped quartz cell having a cross-sectional area of 4 mm^2 (1 mm × 4 mm). The sample solution was circulated by a peristaltic pump. The flow rate was controlled by adjusting the rate of the peristaltic pump and set to about 150 mL/min. The time-resolved UVRR spectra were recorded by changing the distance the irradiated position between the probe pulse and pump beam. In this system, the time-resolution was about 330 μs. For calculating the difference spectrum, the Raman intensity of the ~980 cm^{-1} band of sulfate ion was used as the internal intensity standard.

4.4. Results

Time-Resolved UVRR Spectra of WT KR2.

Figure 4-2 shows a UVRR spectrum recorded only with irradiation of the 233-nm of probe light multiplied by a factor of 0.1 (blue trace) and the pump-induced difference spectra (red traces). On the basis of the result of transient absorption spectra, the recorded RR spectra from 0.1 ms to 5 ms covered to the rise and decay of the O intermediate.[4, 10] In the probe-only spectrum, the bands mainly arise from Trp (W1, W3, W5, W7, W16, W17, and W18) and Tyr (Y1, Y7a, Y8a, and Y9a). The difference spectra were calculated with the SO_4^{2-} band at ~980 cm^{-1} as the internal intensity standard. In the difference spectra, intensity changes for the W7 (~1359 cm^{-1}), W16 (~1010 cm^{-1}), and W18 (~762 cm^{-1}) bands and the frequency shift for the W3 (~1552 cm^{-1}) and Y9a (~1174 cm^{-1}) bands were observed.

The hydrophobic environment around Trp residue induces the red shift of B_b band, which is the π-π^* electronic transition.[18] In the 233-nm exited RR spectra, the increase of hydrophobicity around Trp residues brings the intensity increase of the W16 and W18 bands.[19-21] Therefore, the intensity decrease of these bands in the obtained difference spectra was ascribed to decrease of hydrophobic interaction of Trp residues. The doublet W7 band is known to be sensitive to environmental hydrophobicity.[19, 22] The hydrophobic environment induces the increase of the intensity ratio of I_{1360}/I_{1340}.[19] In the difference spectra, the negative band in the high-frequency region was observed, indicating the decrease of the hydrophobic interaction around Trp residues. This result is consistent with the intensity change of W16 and W18 bands. The difference spectra exhibit the negative band at 1550 cm^{-1}, is ascribed to the high-frequency shift of the W3 band.[20, 23, 24] This band is known to reflect the dihedral angle of the Trp side chain. These results suggested that, in the O intermediate, the orientation of Trp residues altered in addition to the decrease of the hydrophobic interaction. A pair of negative peaks at 1152 cm^{-1} and

1181 cm^{-1} and a positive peak at 1168 cm^{-1} were exhibited in the Y9a mode region of the difference spectra.[25] As the peak position of Y9a of the unphotolyzed KR2 was 1174 cm^{-1}, the derivative-like feature observed in the difference spectra indicates the low-frequency shift and the alternation of the bandwidth of the Y9a band in the O intermediate. The frequency of the Y9a mode is used for a marker of the orientation of the hydrogen atom in its side chain.[25] The observed low-frequency shift of the Y9a band implies that the angle between the hydroxyl group and the benzene ring is increased in the O intermediate. In addition to the low-frequency shift, the bandwidth of the Y9a band changed, suggesting that not a single but multiple Tyr residues showed the structural change.

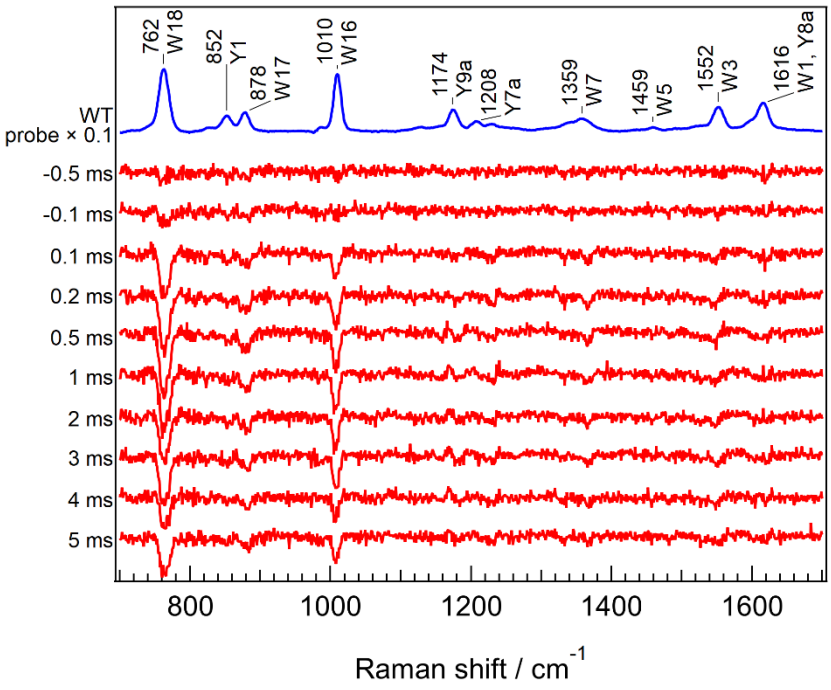

Figure 4-2. The unphotolyzed UVRR spectrum (blue) multiplied by a factor of 0.1 and the time-resolved UVRR spectra (red) of WT KR2. Probe and pump wavelengths were 233 and 532 nm, respectively. The bands arise from Trp and Tyr residues as denoted labels W and Y, respectively. The difference spectra were calculated by subtracting the unphotolyzed spectrum from the pump-probe spectrum by using the SO_4^{2-} band at ~980 cm^{-1} as an internal intensity standard. The accumulation time of each spectrum was 12 min.

As KR2 contains seven Trp residues and fifteen Tyr residues,[4] identification of the residues responsible for the spectral changes to discuss the structural changes in KR2. In this study, we focused on Trp215 and Tyr222, which are close to the retinal chromophore as shown in Figure 4-3. Since Trp215 and Tyr222 are located at the cytoplasmic side and the extracellular side, respectively, their structure may respond to the uptake or release of sodium ion. We prepared the W215F and Y222F mutants, in which Trp215 and Tyr222 were substituted with phenylalanine (Phe). At the excitation wavelength of 233 nm, the vibrational modes of Phe residue are hardly enhanced,[26] so that this substitution enables us the extraction of the spectral changes derived from Trp215 and Tyr222.

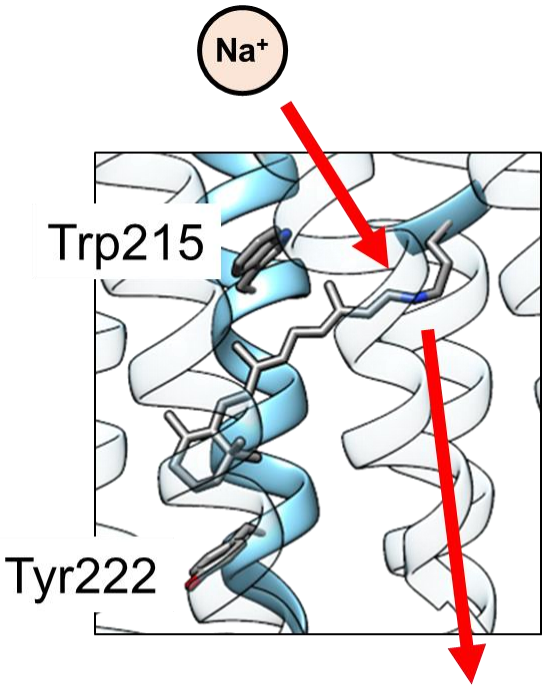

Figure 4-3. Structure of the retinal-binding pocket region. The red arrow represents the sodium ion transport pathway. Trp215 and Tyr222 are located nearby the retinal chromophore. PDB code: 4XTN.

Characterization of W215F and Y222F Mutants.

The light-driven sodium ion pump activity of W215F and Y222F mutants was measured using the ion transport assay. The W215F and Y222F mutants expressed *E. coli* showed the increase of pH by light irradiation, which was enhanced by adding CCCP (Figure 4-4A). These behaviors were almost the same as those of WT KR2, indicating that both W215F and Y222F mutants have light-induced sodium ion pump activity. The spectroscopic analysis of the purified mutants was carried out. The absorption spectra of W215F and Y222F mutants were shown in Figure 4-4B. The absorption peak at ~525 nm was observed among WT and two mutants. This absorption peak is due to the retinal chromophore bound to the protein moiety with forming a Schiff base. In W215F mutant, the extra absorption peak at 380 nm was observed. This peak is often observed when rhodopsin possesses the incorrectly bound retinal chromophore. It suggested that the purified W215F mutant contains incorrectly folded protein. The absorbance ratio between $A_{280\,nm}$ and $A_{retinal}$ (R_{abs}) is often used for the estimation of protein purity. The R_{abs} of W215F mutant was larger than that of WT KR2 and Y222F mutant, also indicating the low purity of W215F mutant. On the other hand, resonance Raman spectra of the retinal chromophore with the 532-nm excitation demonstrated that the structure of the retinal chromophore of these mutants was hardly affected by the mutation (Figure 4-4C).

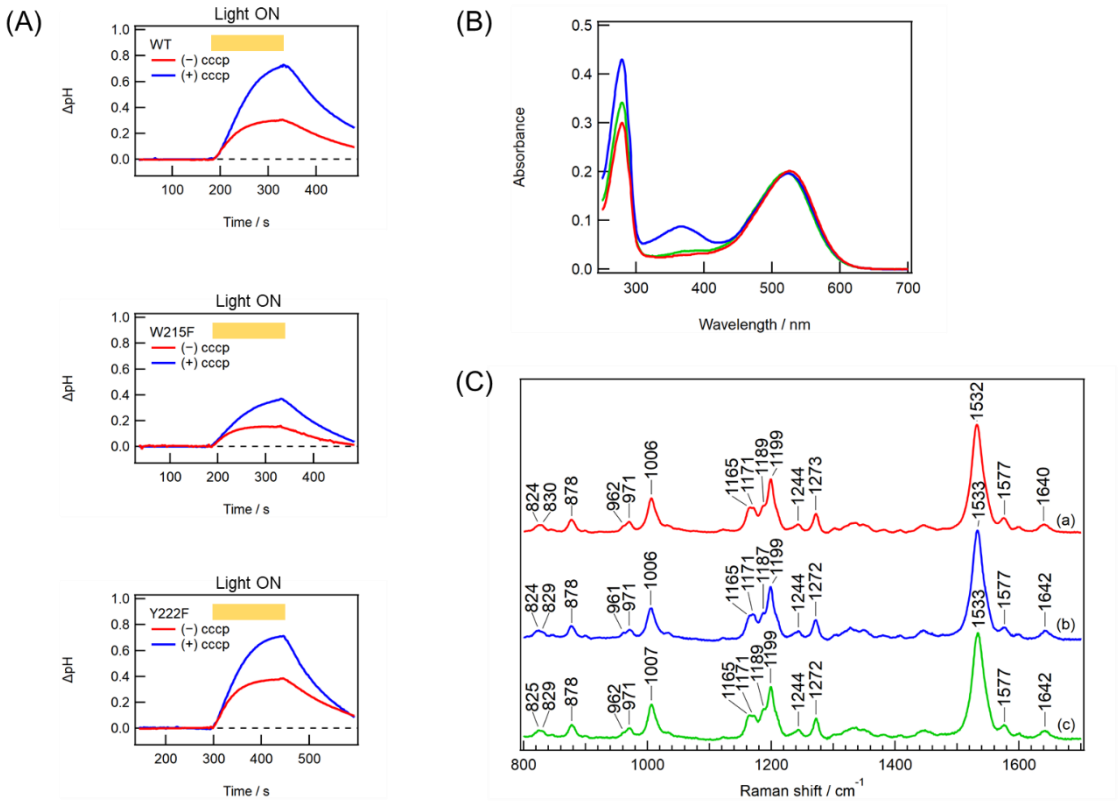

Figure 4-4. (A) Ion-transport assay. The pH changes induced by light irradiation in WT KR2 and KR2 mutants expressed *E. coli* were observed. *E. coli* cells were suspended no buffer solution (300 mM Na_2SO_4, 10 mM NaCl and 5% sucrose). Red and blue traces are the results in the absence and presence of CCCP. Yellow bar is the light irradiated time (3 min). The pH increased by the light irradiation and enhanced upon adding CCCP. They are typical behaviors when rhodopsin works as a light-driven sodium ion pump. (B) Absorption spectra of purified WT KR2 (red), W215F (blue), and Y222F (green). The samples were suspended in a buffer (50 mM Tris-HCl, pH 8.0) with 300 mM Na_2SO_4, 10 mM NaCl and 0.1%DDM. (C) Resonance Raman spectra of the retinal chromophore of WT KR2 (red), W215F (blue), and Y222F (green) with exciting 532-nm probe light. The sample concentration was about 20 μM with the same buffer composition of the absorption spectra measurement. The accumulation time for obtaining each trace was 20 min. The spectrum of the buffer and the emission background were subtracted.

Although it should be noted that the sample of the W215F mutant was low in purity, we found that the sodium-ion transport activity and chromophore structure were not significantly affected by the introduction of mutation. Then, we measured the transient absorption spectra of these mutants in order to investigate the kinetics of each photointermediate in photocycle. Figure 4-5A shows the difference absorbance spectra at each delay time in the range between 350 – 700 nm. Although the photocycle of WT KR2 and Y222F mutant almost completed at 50 ms, that of W215F mutant did not complete even at 900 ms. Figure 4-5B shows the time traces of the difference absorbance at 525 or 520 nm (red), 475 nm (black), 420 or 410 nm (blue), and 605 or 600 nm (green), which correspond to the absorption peak wavelengths of unphotolyzed state, L, M, and O intermediates, respectively.[4] The plot data of the O intermediate was fitted well with three exponential equations. The earlier component is ascribed to the decay of the K intermediate and others are the rise and decay of the O intermediate. The time course of the rise and decay of the O intermediate of WT KR2, W215F, and Y222F mutants were shown in Table 4-1. These results indicate that in the time-resolved UVRR spectra measured with a delay time of 0.1 to 5 ms, the presence of the O intermediate was dominant for not only WT KR2 but also for both mutants.

Table 4-1. Time constants of rise and decay of the O intermediate

	rise / ms	decay / ms
WT KR2	0.39 ± 0.03	6.3 ± 0.2
W215F	0.40 ± 0.06	99.1 ± 12.2
Y222F	0.54 ± 0.08	8.1 ± 0.08

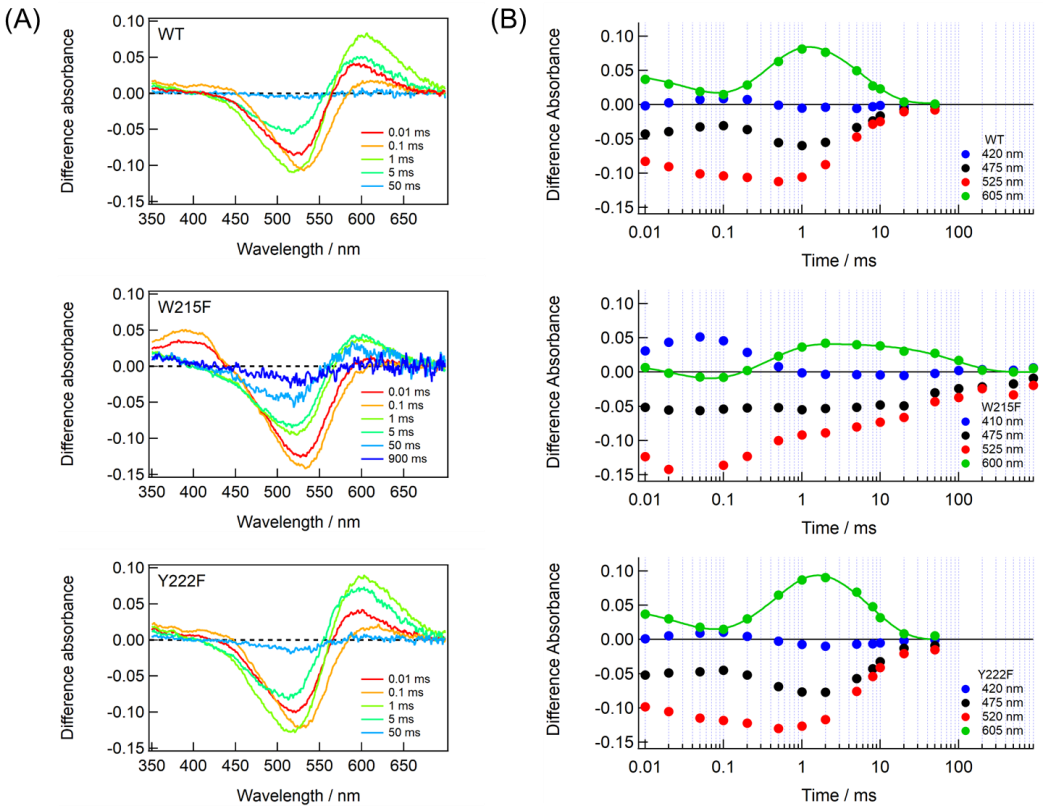

Figure 4-5 (A) Transient absorption spectra measured by time-resolved flash photolysis with 532 nm pulse laser. The repetition frequency was 10 and 0.5 Hz for obtaining data within and after 1 ms, respectively. The samples were suspended in a buffer (50 mM Tris-HCl, pH 8.0) with 300 mM Na_2SO_4, 10 mM NaCl and 0.1%DDM. (B) Time traces of the difference absorbance at 525 or 520 nm (red), 475 nm (black), 420 or 410 nm (blue), and 605 or 600 nm (green). Green lines indicate fitting curve using three exponential equations.

Time-Resolved UVRR Spectra of W215F and Y222F Mutants.

Time-resolved UVRR spectra of W215F and Y222F mutants shown in Figure 4-6 were measured with the same condition of WT KR2. In W215F mutant, the intensity decrease at 761 cm^{-1} was observed similar to WT KR2. However, the maximum amplitude of this negative band in W215F mutant was obviously smaller than that of WT KR2. Furthermore, in W215F mutant, there were no particular intensity changes in W16 band, unlike WT KR2. These results strongly indicated that one of the Trp residues which contribute to the decrease of the W16 and W18 band intensities in the O intermediate is Trp215. In contrast to WT KR2, in the region of the W7 mode, no negative peak in the high-frequency region was observed, and a positive peak was observed in the low-frequency region. Therefore, the intensity ratio of I_{1360}/I_{1340} of W215F mutant in the O intermediate was larger than that of WT KR2. Thus, in the O intermediate, the hydrophobicity around the Trp215 decreases. In the W3 mode region, there were no prominent peaks in the difference spectra, unlike in WT KR2. We concluded that in the O intermediate, the Trp215 alters its orientation and is exposed to the hydrophilic environment. On the other hand, the shape of the difference spectra in the Y9a mode region was almost the same that seen in WT KR2.

Time-resolved difference spectra of Y222F mutant showed that there were no obvious differences of Raman band from Trp residues, expectedly. The spectral pattern in the region of the Y9a mode slightly differed between WT KR2 and Y222F mutant. In order to make a comparison at a high S/N ratio, UVRR spectra at a delay time where the O intermediate becomes most dominant (1 ms for WT KR2, 2 ms for Y222F mutant) were measured with a long accumulation time. The obtained difference spectra both of WT KR2 at 1 ms and Y222F mutant at 2 ms were shown in Figure S4-1. The positive peak observed at 1168 cm^{-1} in WT KR2 showed a small downshift in Y222F mutant. These results suggest that Tyr222 is one of the Tyr residues which showed the structural changes during the sodium-ion transport in WT KR2.

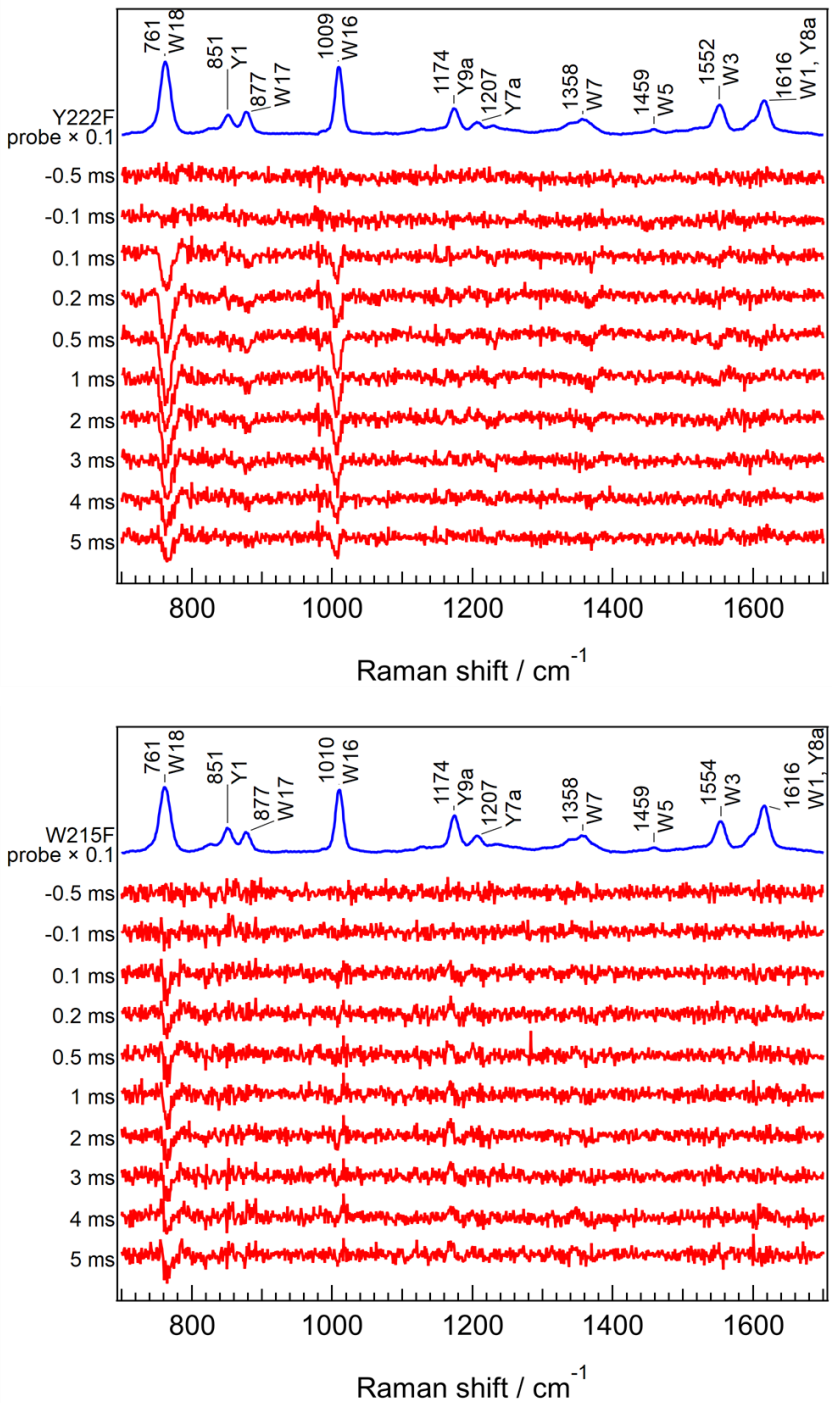

Figure 4-6. The unphotolyzed UVRR spectrum (blue) multiplied by a factor of 0.1 and the time-resolved UVRR spectra (red) of W215F (A) and Y222F (B) Probe and pump wavelengths were 233 and 532 nm, respectively. The bands arise from Trp and Tyr residues as denoted labels W and Y, respectively. The difference spectra were calculated by subtracting the unphotolyzed spectrum from the pump-probe spectrum by using the SO_4^{2-} band at ~980 cm^{-1} as an internal intensity standard. The accumulation time of each spectrum was 12 min.

4.5. Discussion

Structural Changes of Trp Residues.

The time-resolved UVRR spectra of WT KR2 show some structural features that may be related to sodium-ion transport. The W16, W18, and W7 modes are used as a marker of the hydrophobic interaction in Trp residues.[18-21] The obtained difference spectra demonstrated that the intensity decrease of W16 and W18 bands and the decrease of the doublet intensity ratio (I_{1360} / I_{1340}) of W7 band. These results indicate that the decrease of the hydrophobicity around some Trp residues. In addition to the change in the hydrophobic interaction, the orientation of the Trp side chain also changed. From the transient absorption spectroscopy, the time constant of the rise and decay of the O intermediate is 390 μs and 6.3 ms, respectively (Table 4-1). Therefore, the observed time-resolved UVRR spectra recorded at 0.1 – 5 ms reflect the temporal change of M→O→KR2. However, the 330-μs of time resolution in our system restrict the extraction of the kinetics upon the formation of the O intermediate (Figure S4-2).

The delay time at which the intensity of the W16 and W18 band is the smallest was 0.5 ms. This is clearly earlier than the time (about 1 ms from Figure 4-5(B)) at which the proportion of O intermediates is maximal. These results indicate that the hydrophobic interaction of certain Trp residues minimized prior to the formation of the O intermediate. The formation of the O intermediate (or M decay) relates to the uptake of sodium ion from the cytoplasmic side, indicating the creating a transient channel which connects the cytoplasmic side to the retinal Schiff base. This channel probably induces the decrease of the hydrophobicity inside the protein. The W215F mutant enables us to extract the spectral changes seen in WT KR2, and Trp215 is one of the candidate residues which shows the decrease of the hydrophobic interaction and the change in its orientation (Figure 4-6(A)). Since Trp215 is closer to the cytoplasmic side than the retinal chromophore (Figure 4-2), during the transition from the M to the O intermediate, a half

channel connecting the cytoplasmic side and the retinal Schiff base may be formed. In order to determine whether this channel has already been formed in M intermediate, the improve time resolution is needed.

The fact that the negative peaks in the W16 and W18 modes region remains even at 5 ms and they are seen in W215F mutant suggests the formation of the channel connecting the extracellular side and the retinal chromophore. A prime candidate residue is Trp113 located at closer to the extracellular side than the retinal chromophore. Importantly, the obtained difference spectra in W215F mutant showed no or a few spectral changes in the W16 mode region. The intensity ratio of I_{w16}/I_{w18} increases when the indole ring of Trp residue forms cation-π interaction.[27, 28] In KR2, the transient sodium ion binding site composed of Asp251 before the release of sodium ion is created.[3, 14] Since the location of Trp113 is close to Asp251, the cation-π interaction between the bound sodium ion and Trp113 might be formed. In order to verify this hypothesis, improve an S/N ratio for time-resolved UVRR measurement and other mutants study should be carried out.

Structural Changes of Tyr Residues.

One of the major spectral change of Tyr residues is the frequency shift in the Y9a mode region, indicating that the dihedral angle between the hydroxyl group and the benzene ring of the side chain changes in the O intermediate.[25] As KR2 has fifteen Tyr residues, it is difficult to estimate which Tyr shows the spectral change. Time-resolved UVRR spectra with a long accumulation time at the timing where the population of the O intermediate becomes maximum demonstrated that Tyr222 contributes the spectral change in the Y9a mode region (Figure S4-1). Thus, the conformational change around the Tyr222 occurs during the formation of the O intermediate. One possibility is that Tyr222 forms a hydrogen bond and acts as the proton donor because the Y9a mode is sensitive to the C-O-H angle. Although the intensity of the Y9a mode

reflects the strength of the hydrogen bond, we could not argue any intensity changes in the difference spectra as the observed difference spectra may contain the contributions from some Try residues.

Alternative Channel Creating by Helix F Movement.

On the basis of the spectral changes of Trp and Tyr residues, it is suggested that Trp215 plays an important role in forming the transient channel and the structural change in Tyr222 occurs simultaneously. They exist in the same helix (helix F) so that the transient channel forming probably accompany the movement of helix F as shown in Figure 4-7. Giordano et al. reported that the rotating and tilting of helix F upon sodium ion transport in KR2 using electronic paramagnetic resonance spectroscopy.[29] They proposed that the rearrangement of helix F is accompanied to the creating of the half-channel between the retinal Schiff base and cytoplasm. Their results are consistent with our interpretation of the time-resolved UVRR spectra.

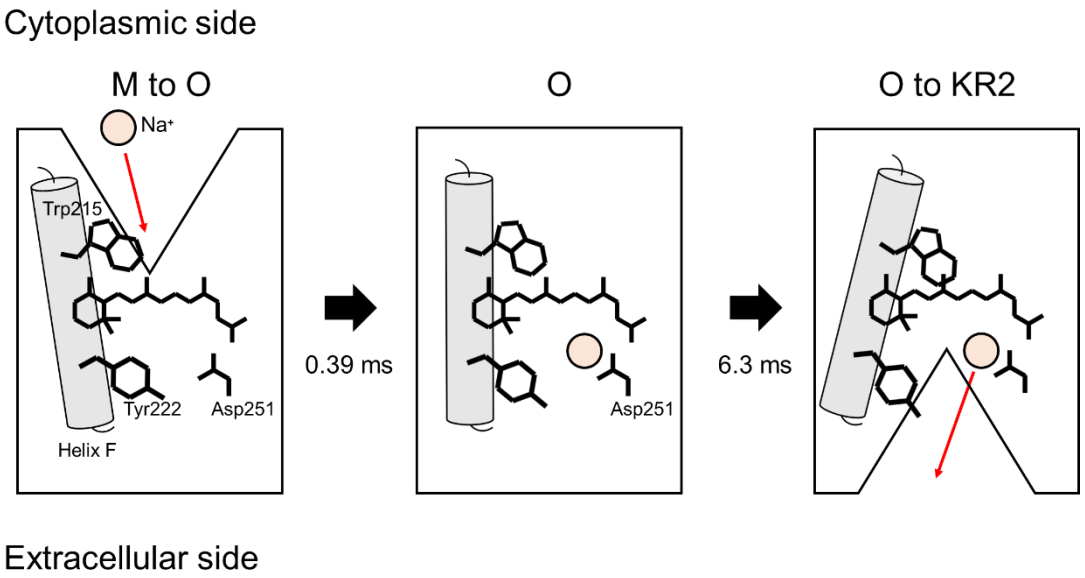

Figure 4-7. Schematic view of the model of the structural change in helix F during the rise and decay of the O intermediate. At M-to-O transition, the transient channel opens to the cytoplasmic side, induces the decrease of the hydrophobicity around Trp215. In the O intermediate, the transient sodium ion binding site is formed by Asp251. Finally, the transient channel opens to the extracellular side in order to hydrate the sodium ion and release it. In a series of the processes, the structural change of F helix, such as tilting and/or twisting occurs.

Additionally, in bacteriorhodopsin (BR), the helix F tilting is suggested in order to create the channel to enter the water molecules. Hashimoto et al. demonstrated that the Trp182 and Trp189, which correspond to Trp215 and Tyr222 in KR2, respectively, play a crucial role in creating the transient channel using time-resolved UVRR spectroscopy.[30, 31] The spectral features relating to the decrease of the hydrophobicity around Trp residues were similar to our data. The conformational change in helix F in BR was also shown in the crystallographic structure.[32] Their electron density map represented that Trp182 conflicts with the 13-methyl retinal group in the M intermediate may induce the helical tilts necessary for proton-pumping function. A recent time-resolved serial crystallography demonstrated the large movement of helix F of BR in the millisecond time region.[33] A similar structural change in helix F is reported in sensory rhodopsin II, functions as a phototaxis sensor.[34] Since Trp215 and Tyr222 in KR2 are well conserved among many microbial rhodopsins as aromatic amino acid residues, e.g. Trp182 and Trp189 in BR, it is probable that such structural changes in the helix F are a common mechanism for microbial rhodopsins.

4.6. Conclusion

The time-resolved UVRR spectra of Trp and Tyr residues revealed that the structural changes of KR2 in the O intermediate, which play a crucial role in the uptake and release of sodium ion. By using the W215F and Y222F mutants, we can extract the spectral components in the difference spectra seen in WT KR2. The time-resolved spectra demonstrated that the decrease of the hydrophobicity around Trp215, indicating that the transient channel is creased upon the M-to-O transition. Furthermore, the orientation of the hydroxyl group of Tyr222 side chain alters in the O intermediate. Trp215 and Tyr222 are in the helix F and located at the cytoplasmic side and extracellular side viewed from the retinal chromophore, respectively. On the basis of these spectral features, we proposed the model that the structural change involves the helix F movement which relates to the transition the cytoplasmic side open state to the extracellular side open state to transport sodium ion unidirectionally. This study demonstrates that time-resolved UVRR spectroscopy is a powerful tool for investigating the ion transport mechanism in the light-driven ion pump rhodopsins. By applying this technique to other rhodopsins, the comprehensive understanding of how rhodopsins can transport diverse ion species despite sharing the similar structure and a common trigger of the photochemical reaction.

4.7. Supporting Information

Time-Resolved UVRR Spectra of WT KR2 and Y222F Mutant in the Y9a Mode Region.

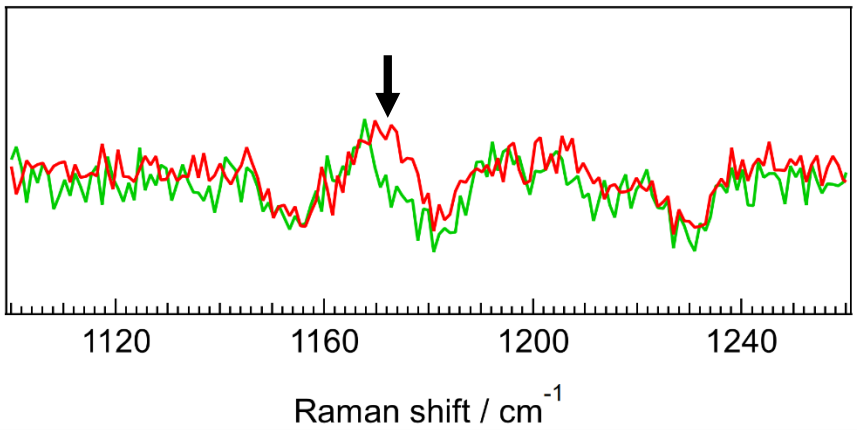

Figure S4-1. The time-resolved difference spectra of WT KR2 (red) and Y222F (green) recorded at 1 and 2 ms, respectively, in the Y9a mode region (1110 – 1250 cm^{-1}). The accumulation time was 48 min. In Y222F, the positive peak at 1172 cm^{-1} (black arrow) observed in WT KR2 was diminished.

Temporal Profiles of Relative Intensity Change of W16 and W18 Bands.

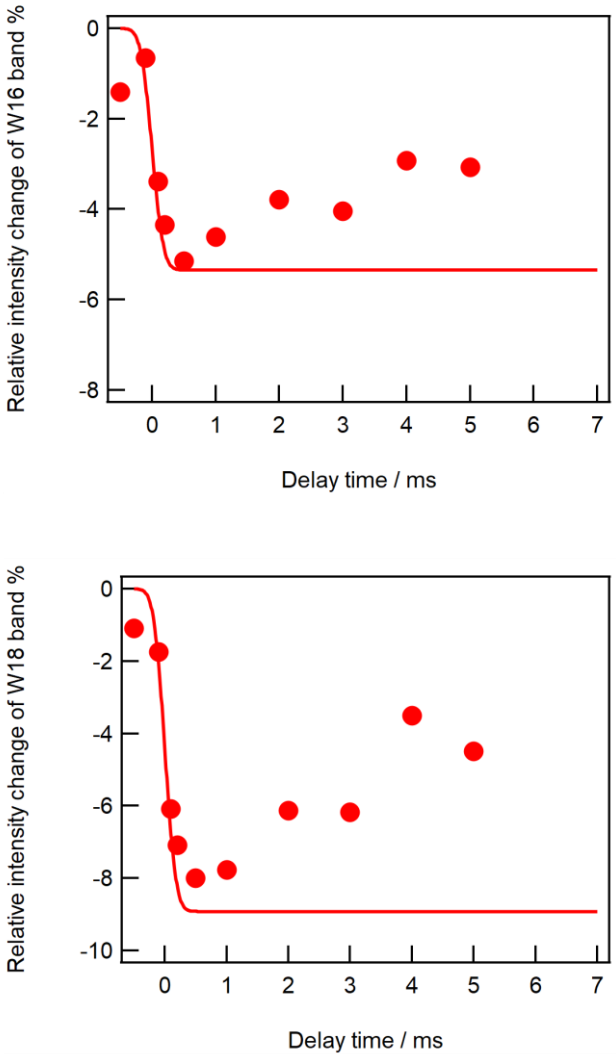

Figure S4-2. The relative intensity changes of W16 and W18 of WT KR2 were plotted against time. To take account of the instrumental response, the step function convoluted with a Gaussian (fwhm = 330 μs) is represented by a solid curve. Since the plots at 0.1 and 0.2 ms were overlapped with the convoluted function, we cannot distinguish whether these earlier data within the instrumental response or not.

4.8. References

[1] Ernst, O. P., Lodowski, D. T., Elstner, M., Hegemann, P., Brown, L. S., and Kandori, H. (2014) Microbial and Animal Rhodopsins: Structures, Functions, and Molecular Mechanisms, *Chem. Rev. 114*, 126-163.

[2] Engelhard, C., Chizhov, I., Siebert, F., and Engelhard, M. (2018) Microbial Halorhodopsins: Light-Driven Chloride Pumps, *Chem. Rev. 118*, 10629-10645.

[3] Kandori, H., Inoue, K., and Tsunoda, S. P. (2018) Light-Driven Sodium-Pumping Rhodopsin: A New Concept of Active Transport, *Chem. Rev. 118*, 10646-10658.

[4] Inoue, K., Ono, H., Abe-Yoshizumi, R., Yoshizawa, S., Ito, H., Kogure, K., and Kandori, H. (2013) A Light-Driven Sodium Ion Pump in Marine Bacteria, *Nat. Commun. 4*, 1678.

[5] Niho, A., Yoshizawa, S., Tsukamoto, T., Kurihara, M., Tahara, S., Nakajima, Y., Mizuno, M., Kuramochi, H., Tahara, T., Mizutani, Y., and Sudo, Y. (2017) Demonstration of a Light-Driven SO_4^{2-} Transporter and Its Spectroscopic Characteristics, *J. Am. Chem. Soc. 139*, 4376-4389.

[6] Inoue, K., Ito, S., Kato, Y., Nomura, Y., Shibata, M., Uchihashi, T., Tsunoda, S. P., and Kandori, H. (2016) A Natural Light-Driven Inward Proton Pump, *Nat. Commun. 7*, 13415.

[7] Kato, H. E., Inoue, K., Abe-Yoshizumi, R., Kato, Y., Ono, H., Konno, M., Hososhima, S., Ishizuka, T., Hoque, M. R., Kunitomo, H., Ito, J., Yoshizawa, S., Yamashita, K., Takemoto, M., Nishizawa, T., Taniguchi, R., Kogure, K., Maturana, A. D., Iino, Y., Yawo, H., Ishitani, R., Kandori, H., and Nureki, O. (2015) Structural Basis for Na^+ Transport Mechanism by a Light-Driven Na^+ Pump, *Nature 521*, 48-53.

[8] Gushchin, I., Shevchenko, V., Polovinkin, V., Kovalev, K., Alekseev, A., Round, E., Borshchevskiy, V., Balandin, T., Popov, A., Gensch, T., Fahlke, C., Bamann, C., Willbold, D., Buldt, G., Bamberg, E., and Gordeliy, V. (2015) Crystal Structure of a Light-Driven Sodium Pump, *Nat. Struct. Mol. Biol. 22*, 390-395.

[9] Tahara, S., Takeuchi, S., Abe-Yoshizumi, R., Inoue, K., Ohtani, H., Kandori, H., and Tahara, T. (2015) Ultrafast Photoreaction Dynamics of a Light-Driven Sodium-Ion-Pumping Retinal Protein from *Krokinobacter eikastus* Revealed by Femtosecond Time-Resolved Absorption Spectroscopy, *J. Phys. Chem. Lett. 6*, 4481-4486.

[10] Asido, M., Eberhardt, P., Kriebel, C. N., Braun, M., Glaubitz, C., and Wachtveitl, J. (2019) Time-Resolved IR Spectroscopy Reveals Mechanistic Details of Ion Transport in the Sodium Pump *Krokinobacter eikastus* Rhodopsin 2, *Phys. Chem. Chem. Phys. 21*, 4461-4471.

[11] Chen, H. F., Inoue, K., Ono, H., Abe-Yoshizumi, R., Wada, A., and Kandori, H. (2018) Time-Resolved FTIR Study of Light-Driven Sodium Pump Rhodopsins, *Phys. Chem. Chem. Phys. 20*, 17694-17704.

[12] Nishimura, N., Mizuno, M., Kandori, H., and Mizutani, Y. (2019) Distortion and a Strong Hydrogen Bond in the Retinal Chromophore Enable Sodium-Ion Transport by the Sodium-Ion Pump KR2, *J. Phys. Chem. B 123*, 3430-3440.

[13] Hontani, Y., Inoue, K., Kloz, M., Kato, Y., Kandori, H., and Kennis, J. T. (2016) The Photochemistry of Sodium Ion Pump Rhodopsin Observed by Watermarked Femto- to Submillisecond Stimulated Raman Spectroscopy, *Phys. Chem. Chem. Phys. 18*, 24729-24736.

[14] Gushchin, I., Shevchenko, V., Polovinkin, V., Borshchevskiy, V., Buslaev, P., Bamberg, E., and Gordeliy, V. (2016) Structure of the Light-Driven Sodium Pump KR2 and Its Implications for Optogenetics, *The FEBS Journal 283*, 1232-1238.

[15] Bogachev, A. V., Bertsova, Y. V., Verkhovskaya, M. L., Mamedov, M. D., and Skulachev, V. P. (2016) Real-Time Kinetics of Electrogenic Na^+ Transport by Rhodopsin from the Marine Flavobacterium Dokdonia sp. PRO95, *Sci. Rep. 6*, 21397.

[16] Kato, Y., Inoue, K., and Kandori, H. (2015) Kinetic Analysis of H^+-Na^+ Selectivity in a Light-Driven Na^+-Pumping Rhodopsin, *J. Phys. Chem. Lett. 6*, 5111-5115.

[17] Oladepo, S. A., Xiong, K., Hong, Z., Asher, S. A., Handen, J., and Lednev, I. K. (2012) UV Resonance Raman Investigations of Peptide and Protein Structure and Dynamics, *Chem. Rev. 112*, 2604-2628.

[18] Sweeney, J. A., and Asher, S. A. (1990) Tryptophan UV Resonance Raman Excitation Profiles, *J. Phys. Chem. 94*, 4784-4791.

[19] Chi, Z., and Asher, S. A. (1998) UV Raman Determination of the Environment and Solvent Exposure of Tyr and Trp Residues, *J. Phys. Chem. B 102*, 9595-9602.

[20] Takeuchi, H. (2011) UV Raman Markers for Structural Analysis of Aromatic Side Chains in Proteins, *Anal. Sci. 27*, 1077-1086.

[21] Matsuno, M., and Takeuchi, H. (1998) Effects of Hydrogen Bonding and Hydrophobic Interactions on the Ultraviolet Resonance Raman Intensities of Indole Ring Vibrations, *Bull. Chem. Soc. Jpn. 71*, 851-857.

[22] Harada, I., Yamagishi, T., Uchida, K., and Takeuchi, H. (1990) Ultraviolet Resonance Raman Spectra of Bacteriorhodopsin in the Light-Adapted and Dark-Adapted States, *J. Am. Chem. Soc. 112*, 2443-2445.

[23] Juszczak, L. J., and Desamero, R. Z. B. (2009) Extension of the Tryptophan $\chi^{2,1}$ Dihedral Angle−W3 Band Frequency Relationship to a Full Rotation: Correlations and Caveats, *Biochemistry 48*, 2777-2787.

[24] Miura, T., Takeuchi, H., and Harada, I. (1989) Tryptophan Raman Bands Sensitive to Hydrogen Bonding and Side-Chain Conformation, *J. Raman Spectrosc. 20*, 667-671.

[25] Takeuchi, H., Watanabe, N., Satoh, Y., and Harada, I. (1989) Effects of Hydrogen Bonding

on the Tyrosine Raman Bands in the 1300–1150 cm^{-1} Region, *J. Raman Spectrosc. 20*, 233-237.

[26] Rava, R. P., and Spiro, T. G. (1985) Resonance Enhancement in the Ultraviolet Raman Spectra of Aromatic Amino Acids, *J. Phys. Chem. 89*, 1856-1861.

[27] Schlamadinger, D. E., Gable, J. E., and Kim, J. E. (2009) Hydrogen Bonding and Solvent Polarity Markers in the UV Resonance Raman Spectrum of Tryptophan: Application to Membrane Proteins, *J. Phys. Chem. B 113*, 14769-14778.

[28] Okada, A., Miura, T., and Takeuchi, H. (2001) Protonation of Histidine and Histidine−Tryptophan Interaction in the Activation of the M2 Ion Channel from Influenza A Virus, *Biochemistry 40*, 6053-6060.

[29] da Silva, G. F., Goblirsch, B. R., Tsai, A. L., and Spudich, J. L. (2015) Cation-Specific Conformations in a Dual-Function Ion-Pumping Microbial Rhodopsin, *Biochemistry 54*, 3950-3959.

[30] Hashimoto, S., Obata, K., Takeuchi, H., Needleman, R., and Lanyi, J. K. (1997) Ultraviolet Resonance Raman Spectra of Trp-182 and Trp-189 in Bacteriorhodopsin: Novel Information on the Structure of Trp-182 and Its Steric Interaction with Retinal, *Biochemistry 36*, 11583-11590.

[31] Hashimoto, S., Sasaki, M., Takeuchi, H., Needleman, R., and Lanyi, J. K. (2002) Changes in Hydrogen Bonding and Environment of Tryptophan Residues on Helix F of Bacteriorhodopsin during the Photocycle: A Time-Resolved Ultraviolet Resonance Raman Study, *Biochemistry 41*, 6495-6503.

[32] Luecke, H., Schobert, B., Cartailler, J.-P., Richter, H.-T., Rosengarth, A., Needleman, R., and Lanyi, J. K. (2000) Coupling Photoisomerization of Retinal to Directional Transport in Bacteriorhodopsin11Edited by D. C. Rees, *J. Mol. Biol. 300*, 1237-1255.

[33] Weinert, T., Skopintsev, P., James, D., Dworkowski, F., Panepucci, E., Kekilli, D., Furrer, A., Brünle, S., Mous, S., Ozerov, D., Nogly, P., Wang, M., and Standfuss, J. (2019) Proton Uptake Mechanism in Bacteriorhodopsin Captured by Serial Synchrotron Crystallography, *Science 365*, 61.

[34] Sasaki, J., Tsai, A.-l., and Spudich, J. L. (2011) Opposite Displacement of Helix F in Attractant and Repellent Signaling by Sensory Rhodopsin-Htr Complexes, *J. Biol. Chem. 286*, 18868-18877.

CHAPTER 5. Resonance Raman Investigation on the Chromophore Structure of Heliorhodopsins

5.1. Abstract

Heliorhodopsins (HeRs) are a new category of retinal-bound proteins recently discovered through functional metagenomics analysis that exhibit obvious differences from type-1 microbial rhodopsins. We conducted the first detailed structural characterization of the retinal chromophore in HeRs using resonance Raman spectroscopy. The observed spectra clearly show that the Schiff base of the chromophore is protonated and forms a strong hydrogen bond to a species other than a water molecule, highly likely a counterion residue. The vibrational mode of the Schiff base of HeRs exhibits similarities with that of photosensory microbial rhodopsins, that is consistent with the previous proposal that HeRs function as photosensors. We also revealed unusual spectral features of the in-plane chain vibrations of the chromophore, suggesting an unprecedented geometry of the Schiff base caused by a difference in the retinal pocket structure of HeRs. These data demonstrate the structural characteristics of the photoreceptive site in this novel type of rhodopsin family.

5.2. Introduction

Rhodopsins are currently classified into the two distinct types, microbial rhodopsins (type-1) and animal rhodopsins (type-2).[1] Very recently, a new family of rhodopsin different from type-1 and type-2 was discovered using metagenomics analysis.[2] The proteins, named heliorhodopsins, are similar to the microbial rhodopsins, has the all-*trans* retinal as a chromophore inside a heptahelical transmembrane motif. On the other hand, HeRs have a distinctly different amino acid sequence from any type of rhodopsins and their orientation in the cell membrane is opposite the that of other types rhodopsins. The isomerization characteristics were similar to other rhodopsins, despite the fact that the amino acids around the chromophore were largely different.[3] The function of HeRs is little understood. Although HeRs show the photocycle with longer than 1 second, they did not pump any ions. The existing of the long-lived photointermediate implies that HeRs may function as a photosensor, however, the transducer of HeRs has not been determined.

The study of HeR has just begun, and in this context, it is important to compare the chromophore structure, which plays a key role in rhodopsin's function, of HeR with that of microbial rhodopsins because of two reasons. (1) Microbial rhodopsins show various functions, such as ion pumps,[4-6] ion channels,[7] photosensor,[8, 9] or light-activated enzymes.[10-12] (2) There are lots of studies for the elucidation of the chromophore structure. Here we used resonance Raman (RR) spectroscopy to study HeRs and observed unique spectral features of the retinal chromophore in the proteins. The observed features show both similarities and differences in the chromophore structure of HeRs compared to type-1 microbial rhodopsins. This is the first detailed structural characterization study of the photoreceptive site in this novel rhodopsin family.

5.3. Materials and Methods

Sample Preparation

Gene of HeR 48C12 was closed from the metagenome analysis and subcloned into a pET-9d(+)vector with N-terminal 6 x His-tag as reported previously.[2] Gene of HeR from *Thermoplasmatales archaeon* was synthesized with N-terminal 6 x His-tag. Proteins for resonance Raman spectroscopy were heterologously expressed by *E. coli*, and purified as described previously.[2, 13] *E. coli* cell culture (4 L) expressing each HeR was prepared, where protein expression was induced by 1.0 mM isopropyl β-D-thiogalactopyranoside (IPTG) in the presence of 10 μM all-trans-retinal (Sigma-Aldrich). The cells were disrupted by a French press (Ohtake) and membrane fraction was collected by ultracentrifugation (125,000g, 1h). The proteins were solubilized by 2.0% *n*-dodecyl-β-$_D$-maltoside (DDM) (Anatrace) in the presence of 300 mM NaCl, 5 mM imidazole and 50 mM MES (pH 6.5). After loading on Co^{2+}-NTA affinity resin, the sample was washed extensively with buffer (50 mM MES, pH 6.5) containing 300 mM NaCl, 50 mM imidazole and 0.1% w/v DDM to remove non-specifically bound proteins. The His-tagged proteins were then eluted with elution buffer (0.1% DDM, 300 mM NaCl, 50 mM MES, pH 6.0 and 500 mM imidazole). The fractions collected were dialyzed against a solution containing 300 mM NaCl, 0.05% DDM and 20 mM Tris (pH 7.0), and centrifuged by use of Amicon (15,000 MW).

Resonance Raman Spectroscopy

For resonance Raman (RR) measurements, the sample solutions containing 20 μM heliorhodopsins (HeR) in 50 mM Tris-HCl buffer at pH 8.0 with 10 mM NaCl, 300 mM Na_2SO_4, and 0.05% DDM were used. The H_2O buffer was exchanged with D_2O buffer or mixed buffer (H_2O/D_2O = 1:1). The apparatus of the resonance Raman measurements was described in Chapter 2. The photocycle of HeR takes so long time that it is required to avoid the accumulation of the

long-lived photointermediates during photoirradiation for obtaining the RR spectra of the unphotolyzed state. To avoid the accumulation, we circulated the sample solution through a 1.5-mmϕ quartz flow cell with the flow rate of 15 mL/min. We found that the probe power of 80 μW at the sample position was weak enough to avoid the contamination based on the linearity of the RR intensities of HeR with respect to the probe power and the absence of the additional bands due to the photolyzed protein as shown in Figure S5-1, S5-2, and S5-3. Accumulation time per spectrum was 60 min. The spectral dispersion was about 0.7–0.9 cm^{-1}/pixel on the CCD camera. Raman shifts were calibrated Raman bands of 2-propanol, ethanol, and acetone. The calibration error was within 1 cm^{-1}.

5.4. Results and Discussion

Two HeRs, HeR 48C12 and HeR *Thermoplasmatales archaeon* SG8-52-1, were excited at 532 nm and their resonance Raman spectra are presented in Figure 5-1A and 5-1B, respectively. The red and blue traces in each panel show spectra observed in H_2O and D_2O buffer, respectively. Comparison of these RR spectra to those of *Halobacterium salinarum* bacteriorhodopsin (HsBR)[14] allowed us to assign the observed RR bands. An intense doublet band at 1523 and 1542 cm^{-1} in the spectrum of HeR 48C12 measured in H_2O buffer arises from the in-phase C=C stretching [ν(C=C)] vibrations of the chromophore. Out-of-phase ν(C=C) bands are observed at 1572 and 1597 cm^{-1}. A band at 1648 cm^{-1} is assigned to the C=N stretching [ν(C=N)] mode of the Schiff base. A band observed at 1451 cm^{-1} is due to methyl deformation modes. In-plane rocking modes are observed at 1270-1350 cm^{-1}, C-H rocking [δ(C–H)] bands at 1272, 1301, and 1332 cm^{-1}, and an N-H rocking [δ(N–H)] band at 1348 cm^{-1}. Bands at 1170, 1184, 1198, and 1247 cm^{-1} are due to C–C stretch [ν(C–C)] modes of the retinal chromophore. A methyl rocking band is observed at 1005 cm^{-1}. Weak bands at 800-900 cm^{-1} are assignable to hydrogen out-of-plane (HOOP) wagging modes.

HeR 48C12 in H_2O exhibits the ν(C=N) band at 1648 cm^{-1}, which is downshifted to 1631 cm^{-1} in D_2O buffer. The 1341-cm^{-1} δ(N–H) band disappears and a new band appears at 987 cm^{-1} in D_2O buffer and is assigned as the N–D rocking [δ(N–D)] band. The downshifts of the ν(C=N) and δ(N–H) bands in D_2O buffer show that the Schiff base of the HeR 48C12 chromophore is protonated, confirming a previous assignment of the protonation state.[2] HeR *T. archaeon* shows similar deuteration effects on the ν(C=N) and δ(N–H) bands, indicating that its Schiff base is also protonated. This PSB structure is shared with the unphotolyzed state of type-1 microbial rhodopsins.

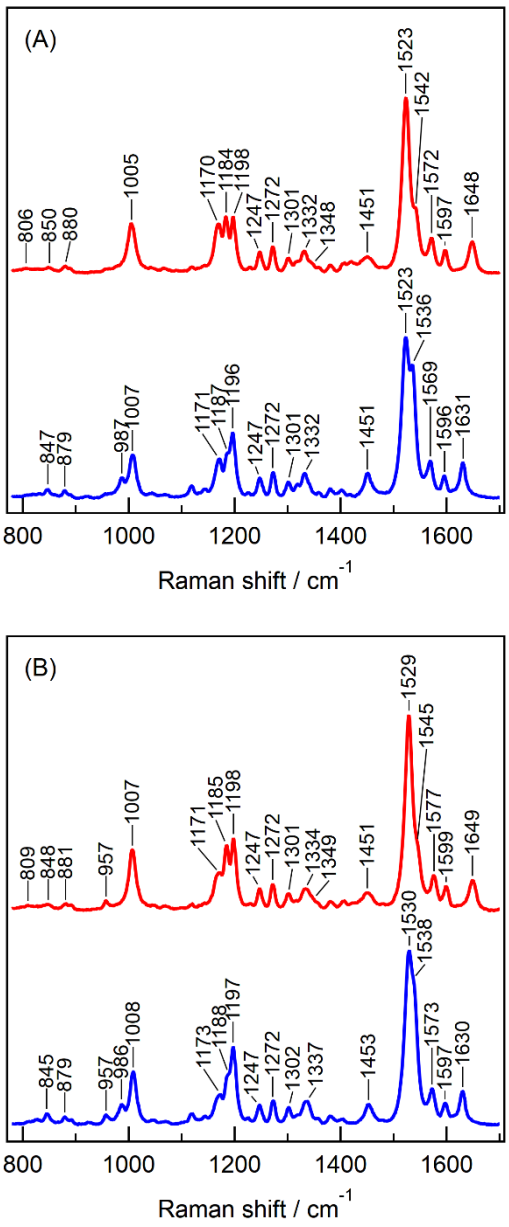

Figure 5-1. Resonance Raman spectra of HeR 48C12 (A) and HeR T. archaeon (B) excited at 532 nm. The red and blue traces in each panel show spectra observed in H2O and D2O buffer, respectively. A solution of 20 μM HeRs in buffer comprising 50 mM Tris-HCl at pH 8.0 with 10 mM NaCl, 300 mM Na2SO4, and 0.05% DDM was used for the measurements. The accumulation time for obtaining each trace was 60 min. The spectrum of the buffer and the emission background were subtracted. Details regarding sample preparation and resonance Raman measurements are described in Supporting information.

The magnitude of the deuteration shift is a sensitive marker of the hydrogen bond strength of the PSB. The PSB with stronger hydrogen bonds exhibits a larger deuteration shift because the ν(C=N) mode couples with the δ(N–H) mode in H_2O buffer and decouples from the δ(N–D) mode in D_2O buffer.[15] The amplitudes of the deuteration shifts of the ν(C=N) band for HeR 48C12 (17 cm^{-1}) and HeR *T. archaeon* (19 cm^{-1}) were similar to those for the proton-pumping rhodopsins HsBR (16 cm^{-1}),[14] blue-light-absorbing proteorhodopsin (21 cm^{-1}),[16] green-light-absorbing proteorhodopsin (23 cm^{-1}),[16] and archaerhodopsin-3 (20 cm^{-1}).[17] In contrast with the proton-pumping rhodopsins, the amplitudes of the deuteration shifts of chloride-pumping rhodopsins are small.[18-22] Large deuteration shifts similar to HeRs were reported for two sensory rhodopsin II (SRII) proteins, from *Halobacterium salinarum* (23 cm^{-1})[23] and from *Natronobacterium pharaonis* (25 and 21 cm^{-1}).[24, 25] We previously hypothesized that HeRs function as photosensor[2] and our present observation of the common feature of a strongly hydrogen-bonded PSB in HeRs and SRII is consistent with this hypothesis.

Another spectral feature of HeRs in common with SRII is the ν(C=N) frequency. As mentioned above, the ν(C=N) mode decouples from the δ(N–D) mode in D_2O and thus the frequency of the ν(C=N) mode in D_2O buffer reflects the character of the C=N bond, independent of the hydrogen bond strength of the Schiff base. The ν(C=N) frequencies of HeRs in D_2O buffer are 1631 and 1630 cm^{-1}, which are higher than those observed for ion pumps[14, 16-22] and comparable with those observed for SRII from *Halobacterium salinarum* (1634 cm^{-1})[23] and SRII from *Natronobacterium pharaonis* (1625 and 1631 cm^{-1}).[25] This similarity in frequency suggests that both the structure of the retinal chromophore and its environment are similar in HeRs and SRIIs.

The bandwidth of the ν(C=N) band was examined to investigate the hydrogen bonding partner of the PSB. Figure 5-2 shows expanded views of the ν(C=N) region for samples in H_2O

buffer (trace a), 1:1 H_2O/D_2O mixed buffer (trace b), and D_2O buffer (trace c). Panels A and B show spectra for HeR 48C12 and HeR *T. archaeon*, respectively. We fitted the observed ν(C=N) bands using Lorentzian functions. We showed residuals in the bandwidth analysis in Figure S5-4 in Supporting Information. There are no unequal error variances between the observed and fitted values, demonstrating that the observed ν(C=N) bands are well described by Lorentzian functions. For HeR 48C12, the fitting analysis showed that the width of the ν(C=N) band is slightly broadened following D_2O/H_2O exchange, from 13.6±0.2 to 14.9±0.2 cm^{-1}. In the mixed buffer, the widths of the ν(C=N) band for the H- and D-bound Schiff base were 13.6±0.6 and 14.0±0.7 cm^{-1}, respectively. A difference in width of 3.8 cm^{-1} between the ν(C=N) RR bands of HsBR in H_2O and D_2O buffer was previously reported[26] and attributed to resonance vibrational energy transfer between the ν(C=N) mode of the PSB and the bending mode of an H_2O molecule hydrogen-bonded to the PSB. The observed broadening for HeR 48C12 (1.3 cm^{-1}) is smaller than that for HsBR, implying that the energy transfer rate is low. Therefore, a water molecule is not a partner in the strong hydrogen bond of the PSB and only weakly interacts with the PSB. For HeR *T. archaeon*, the ν(C=N) band in H_2O buffer (14.8±0.3 cm^{-1}) was broader than in D_2O buffer (12.5±0.4 cm^{-1}). This broadening is not due to resonance vibrational energy transfer because the widths in H_2O (14.8±0.3 cm^{-1}) and D_2O buffer (12.5±0.4 cm^{-1}) are equal to those for the H- (14.4±0.8 cm^{-1}) and D-bound Schiff base (13.4±0.7 cm^{-1}) in the mixed buffer, respectively, within experimental error. Accordingly, the widths of the ν(C=N) RR bands provide clear experimental evidence that the PSB of HeRs forms a strong hydrogen bond to a species other than a water molecule. Glu107 was previously assigned as the counterion for the PSB in HeR 48C12.[2] Given the sequence similarity of the two proteins, Glu108 is a possible counterion in HeR *T. archaeon* and is the most probable strong hydrogen-bonding partner in both HeR 48C12 and HeR *T. archaeon*.

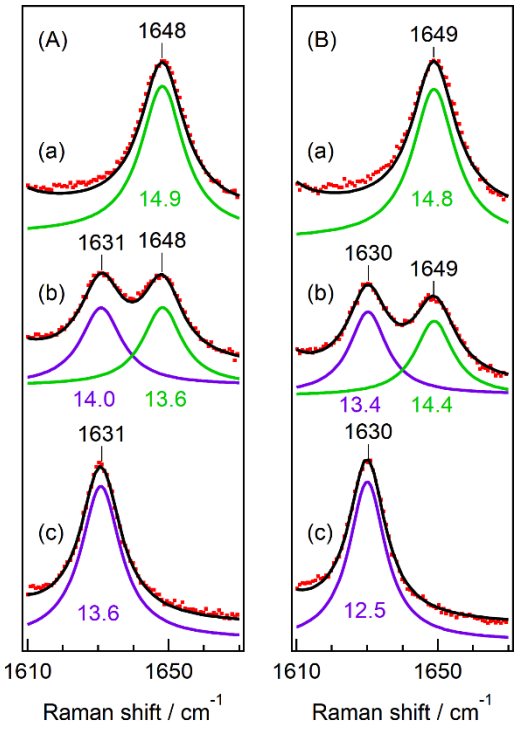

Figure 5-2. Expanded views of RR spectra in the ν(C=N) band region (1610−1670 cm^{-1}) of HeR 48C12 (A) and HeR *T. archaeon* (B). Traces a−c in each panel represent RR spectra of samples in H_2O buffer, mixed buffer (H_2O/D_2O = 1:1), and D_2O buffer, respectively. The accumulation time for obtaining each trace was 60 min. The spectral contribution of the buffer and the emission background were subtracted. The black curves are the best fit of the sum of Lorentzian functions. The green and purple curves show the fitting results of the Lorentzian curves representing the ν(C=N) bands for the H- and D-bound Schiff bases, respectively. The fitting parameters of the peak positions and the bandwidths (full width at half-maximum) are given in the figure.

We observed unusual spectral features for the in-plane chain vibrational modes of the HeRs, with one of the most pronounced differences with type-1 microbial rhodopsins being the profile of the most intense band of the ν(C=C) modes. The ν(C=C) band in the spectrum of HeR 48C12 in H_2O buffer showed a doublet feature at 1523 and 1542 cm^{-1}, which is not observed for the in-phase ν(C=C) bands of type-1 microbial rhodopsins. We confirmed that there was no spectral contamination of the photointermediates in the traces shown in Figure 5-1 by carefully examining the dependence of the RR intensities (Figure S5-1 and S5-2 in Supporting Information) and the spectral patterns (Figure S5-3 in Supporting Information) on the probe power. Other in-plane chain vibrations are the ν(C–C) modes, observed at 1170, 1184, 1198, and 1247 cm^{-1} for HeR 48C12. The relative intensities of the 1170-, 1184-, 1198-cm^{-1} bands are different from those of type-1 microbial rhodopsins with the all-trans form of the retinal chromophore.[14, 27] The ν(C–C) bands are regarded as fingerprints because their frequencies and relative intensities are sensitive to the geometry of the retinal chromophore.[28] The differences in the relative intensities of the ν(C–C) bands of HeR 48C12 and type-1 microbial rhodopsins suggest a difference in the geometry of the chromophore, although the configuration of the retinal chromophore of HeR 48C12 was determined by HPLC analysis to be all-trans. For HeR *T. archaeon*, the most intense ν(C=C) band was observed at 1529 cm^{-1} with a shoulder band at 1545 cm^{-1}. Triplet bands for ν(C–C) modes, similar to that of HeR 48C12, were observed at 1171, 1185 and 1198 cm^{-1}. Accordingly, the unphotolyzed states of the HeRs exhibited an intensity pattern of in-plane chain vibrational modes distinct from those of the unphotolyzed state of type-1 microbial rhodopsins.

It is unlikely that the doublet observed for the most intense bands is due to two conformations in HeRs on the basis of the following reasons although we cannot completely rule out such a possibility. First, the appearance of the two out-of-phase ν(C=C) bands at 1572 and 1597 cm^{-1} for HeR 48C12 and those at 1577 and 1599 cm^{-1} for HeR *T. archaeon* are common

with unphotolyzed forms of type-1 microbial rhodopsins.[14] They did not show a doublet feature and sharp as shown in Figure 5-1. Second, if the doublet observed for the most intense bands is due to two conformations, it is estimated that their absorption maximum wavelength is 50-70 nm different from each other on the basis of a linear correlation between the ν(C=C) frequencies and absorption maximum wavelengths of rhodopsins (vide infra). Absorption bands separated by 60-70 nm can be readily detected but multiple bands were not observed in the absorption spectrum of HeR 48C12.[2] Third, time evolutions of transient absorption change were well described assuming there is a single conformation in HeR.[2] Forth, it was shown that most of the retinal (>97%) bound to HeR 48C12 adopts an all-trans configuration in the unphotolyzed state by HPLC analysis for the extracted retinal oxime.[2]

There is a negative linear correlation between the ν(C=C) frequencies and absorption maximum wavelengths.[29] This is because the HOMO-LUMO energy gap becomes smaller and the bond order of the C=C bond decreases as π-conjugation becomes more delocalized. Figure 5-3 shows a plot of the RR ν(C=C) frequency against the absorption maximum wavelength for sixteen datasets for nine retinal proteins. The black line represents the best-fit linear function for the sixteen datasets and the solid circles represent the frequencies and wavelengths for the HeRs. The data point (number 2) for HeR 48C12 deviates markedly from the line.

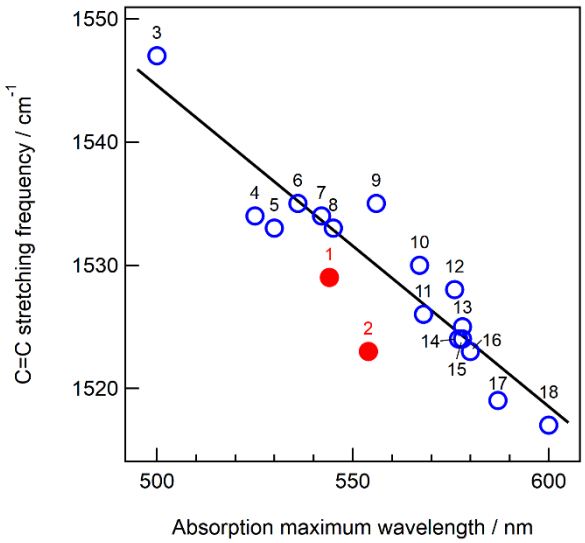

Figure 5-3. Plot of the RR C=C stretching frequency against the absorption maximum wavelength for HeRs reported in this study (red circles 1: HeR *T. archaeon* and 2: HeR 48C12) and sixteen datasets for nine retinal proteins previously reported (blue circles; 3: *Natronomonas pharaonis* SRII,[24] 4: *Indibacter alkaliphilus* sodium-ion-pump rhodopsin,[30] 5: thermophilic rhodopsin,[31] 6: Cl^- bound *Synechocystis* halorhodopsin (SyHR),[32] 7: anion-depleted SyHR,[32] 8: proteorhodopsin,[33] 9: SO_4^{2-} bound SyHR,[32] 10: NO_3^- bound *Halobacterium salinarum* halorhodopsin (HsHR),[19] 11: HsBR,[34] 12: Cl^- bound HsHR,[19] 13, 14: Cl^- bound *Natronobacterium pharaonis* halorhodopsin (NpHR),[21, 22] 15: Br^- bound NpHR,[22] 16: I^- bound NpHR,[22] 17: *Halobacterium salinarum* sensory rhodopsin I,[35] and 18: anion-depleted NpHR[21]). The black line is the best-fit linear function for the sixteen datasets.

The observed unusual splitting of the ν(C=C) band also suggests that the normal mode character of the band is altered in HeRs. The intrinsic RR intensities of the individual modes of the polyene chain sum together to provide an intense band in an in-phase combination of ν(C=C) modes while an out-of-phase combination of the ν(C=C) component results in cancellation in the intensity.[36, 37] Thus, the observed doublet feature implies a change in normal mode character, in which the RR intensities of the in-phase ν(C=C) mode are shared with other ν(C=C) modes. Such a change in normal mode character results in a frequency change of the in-phase ν(C=C) mode without a large change of absorption maximum wavelength. Accordingly, the deviation of the data point for HeR 48C12 is attributable to the difference of the normal mode characteristics of the observed ν(C=C) bands for HeRs from those of type-1 microbial rhodopsins.

A noticeable shift in the ν(C=C) band at 1542 cm^{-1} upon deuteration of the PSB was observed for HeR 48C12 and at 1545 cm^{-1} for HeR *T. archaeon*. The deuteration shifts of the ν(C=C) bands indicate significant coupling of the ν(C=C) and δ(N–H) modes in the HeR chromophores whereas this coupling is so small for the chromophore in the all-trans form of type-1 microbial rhodopsins that no such deuteration shift of the ν(C=C) bands is observed.[14, 38] It is highly likely that this coupling in HeR chromophores to the δ(N–H) mode is responsible for the unusual splitting of the ν(C=C) bands and changes in the normal modes of HeRs. A unique feature of the HeRs is that their chromophore has a structure that supports significant coupling between the ν(C=C) and δ(N–H) modes.

The altered vibrational features of the ν(C=C) and ν(C–C) bands suggest that the geometry of the HeR chromophore differs from that of type-1 microbial rhodopsins. The differences in these vibrational characteristics are not due to torsional distortion of the polyene chain of the chromophore. The RR intensities of the HOOP modes provide a probe of

chromophore structure,[39] with the HOOP modes being typically weak in the RR spectrum of a planar chromophore and strongly enhanced following torsional deformation. The absence of intense HOOP modes in HeRs indicates that the chromophore is not significantly twisted and thus the differences in the vibrational characteristics are not due to torsional distortion of the retinal chromophore.

We observed that the relative intensity of the 1198-cm^{-1} band, assigned to the C_{14}–C_{15} stretching mode,[14] was altered upon deuteration of the PSB in the two HeRs (Figure 5-1) due to the coupling between the δ(N–D) and ν(C–C) modes. The fingerprint ν(C–C) region of the light-adapted form of HsBR is insensitive to deuteration of the Schiff base nitrogen.[14] In particular, no change was observed in the frequency of the C_{14}–C_{15} stretching mode of HsBR. A normal mode analysis by Smith et al. showed that N-deuteration does not result in a C_{14}–C_{15} frequency shift if the C=N bond is in the anti-configuration.[27] Consequently, the observed couplings of the δ(N–H) or δ(N–D) mode to the ν(C=C) and ν(C–C) modes suggest an unprecedented geometry for the Schiff base in the HeR chromophores. Several residues are highly conserved around the retinal chromophore of type-1 microbial rhodopsins that are not conserved in the HeRs.[2, 13] The unprecedented geometry is most likely caused by the difference in the structure of the retinal pocket in HeRs. This difference in chromophore geometry may be responsible for the slow re-isomerization of late intermediate(s) in the photocycle previously discussed in association with a possible photosensory function of HeRs.[2]

5.5. Conclusion

In summary, we characterized the RR spectra of HeR 48C12 and HeR *T. archaeon*. This is the first detailed structural investigation to explore the PSB of the chromophore. Our results demonstrate that a strong hydrogen bond likely forms to a counterion residue in the HeRs. Furthermore, the vibrational coupling of the ν(C=C) and δ(N–H) modes indicate a structural difference in the polyene chains between the HeRs and type-1 microbial rhodopsins in terms of Schiff base geometry. Taken together, these findings further our understanding of the structure-function relationship governing the activity of this newly discovered category of rhodopsins.

5.6. Supporting Information

Dependence of the Probe Power on the RR Intensities of HeRs in the H_2O Buffer.

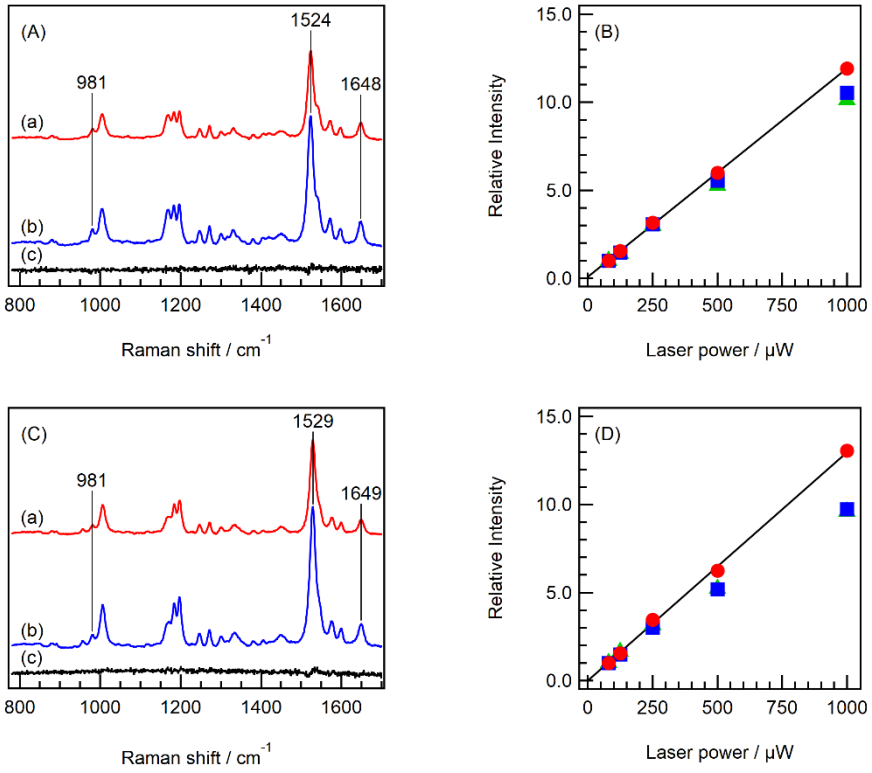

Figure S5-1. Dependence of the probe power on the RR intensities of HeRs in the H2O buffer. (A and B) HeR 48C12, (C and D) HeR T. archaeon. Panels A and C display obtained RR spectra with different laser power. In each panel, traces a and b show the spectra measured with the probe power of 80 and 125 μW, respectively. Trace c shows difference spectrum obtained by (trace a) – k × (trace b) (k = 0.68 for panel A and 0.67 for panel C). The intensities of trace c were magnified by three times. Panels B and D display relative intensities of the RR bands of HeR with respect to the probe power; green triangles, blue squares, and red circles indicate the relative intensities of the ν(C=C) (1524 cm–1) and the ν(C=N) (1648 cm–1) bands of the retinal chromophore and that due to the sulfate ion (981 cm–1) added as an internal intensity standard, respectively. The intensity for each Raman band in panels B and D was normalized with the intensity measured with the probe power of 80 μW. The black line represents linear fits for the intensities of the sulfate band. The linearity of the RR intensities against the probe power was observed in the probe power below 125 μW. Accordingly, the probe power of 80 μW was weak enough to avoid the contamination of spectral contributions of the photolyzed species.

Dependence of the Probe Power on the RR Intensities of HeRs in the D_2O Buffer.

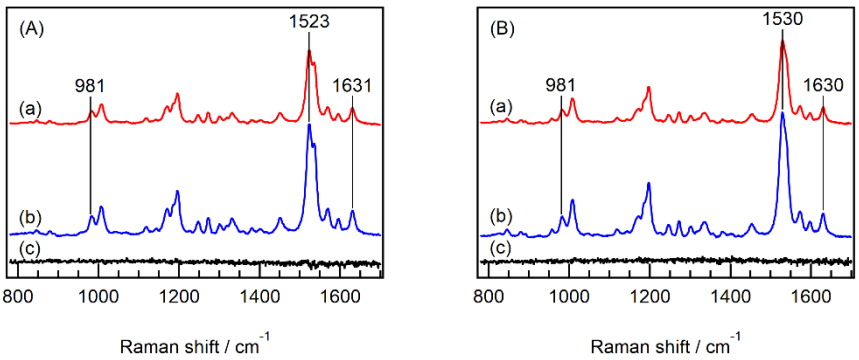

Figure S5-2. Dependence of the probe power on the RR spectra of HeRs in the D2O buffer. (A) HeR 48C12, (B) HeR T. archaeon. They display obtained RR spectra with different laser power. In each panel, traces a and b show the spectra measured with the probe power of 80 and 125 μW, respectively. Trace c shows difference spectrum obtained by (trace a) – k × (trace b) (k = 0.67 both for panels A and B). The intensities of trace c were magnified by three times. In the D2O buffer, the N-D rocking band appears at ~980 cm–1, which overlaps the band of the sulfate ion at 981 cm–1. The overlap makes it difficult to determine the band intensities of the sulfate ion and to examine the linearity of the RR intensities against the probe power as we did in Figure S5-1. Even without the examination of the linearity, absence of prominent bands in the difference spectrum for each sample shows that the intensity ratios between traces a and b are uniform among the observed RR bands. Accordingly, the probe power of 80 μW was weak enough to avoid the contamination of spectral contributions of the photolyzed species.

Dependence of the Probe Power on the RR Spectral Pattern of HeRs.

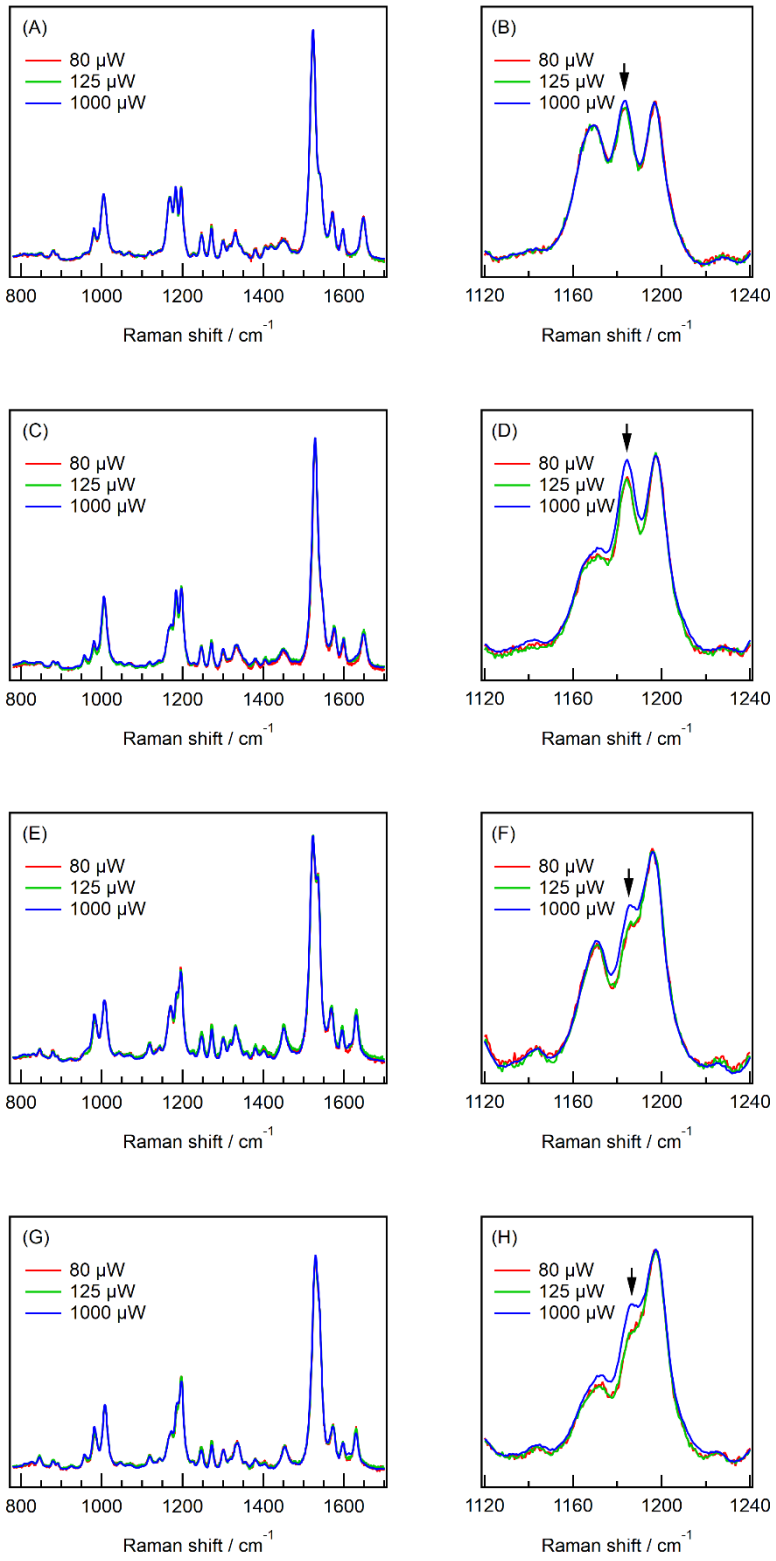

Figure S5-3. Dependence of the probe power on the RR spectral pattern of HeRs. (A and B) HeR 48C12 in the H2O buffer, (C and D) HeR T. archaeon in the H2O buffer, (E and F) HeR 48C12 in the D2O buffer, and (G and H) HeR T. archaeon in the D2O buffer. Left and right panels display the overviews of the RR spectra and the expanded views of the ν(C–C) band region. The probe power for obtaining each spectrum is shown in the upper-left corner. The intensities of the spectra in each panel were normalized based on the intensity of the most intense ν(C=C) band. In right panels, the spectra measured with 125-μW probe power are identical to those measured with 80-μW probe power for all samples. It should be noted that the spectra measured with 1000-μW power indicate additional bands due to the photolyzed protein (black arrows). These data again corroborate the judgment that the probe power of 80 μW was weak enough to avoid the contamination of the undesirable photolyzed species.

Residuals in the Bandwidth Analysis of the Observed ν(C=N) Bands of HeRs.

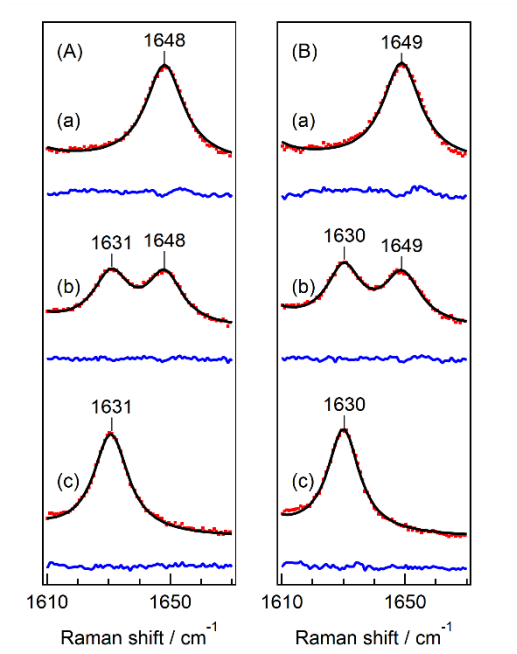

Figure S5-4. Expanded views of RR spectra in the ν(C=N) band region (1610−1670 cm–1) of HeR 48C12 (A) and HeR T. archaeon (B). Traces a−c in each panel represent RR spectra of samples in H2O buffer, mixed buffer (H2O/D2O = 1:1), and D2O buffer, respectively. The accumulation time for obtaining each trace was 60 min. The spectral contribution of the buffer and the emission background were subtracted. The black curves are the best fit of the sum of Lorentzian functions. The blue curves show residuals of the fitting. There are no unequal error variances between the observed and fitted values, demonstrating that the observed ν(C=N) bands are well described by Lorentzian functions.

5.7. Copyright Permission

This chapter has been written based on the published paper [A. Otomo, M. Mizuno, M. Singh, W. Shihoya, K. Inoue, O. Nureki, O. Béjà, H. Kandori, and Y. Mizutani "Resonance Raman Investigation of the Chromophore Structure of Heliprhodopsins" *J. Phys. Chem. Lett.*, American Chemical Society, **2018**, 9, 6431-6436]. The copyright permission to reprint this paper was obtained from ACS publication via Copyright Clearance Center.

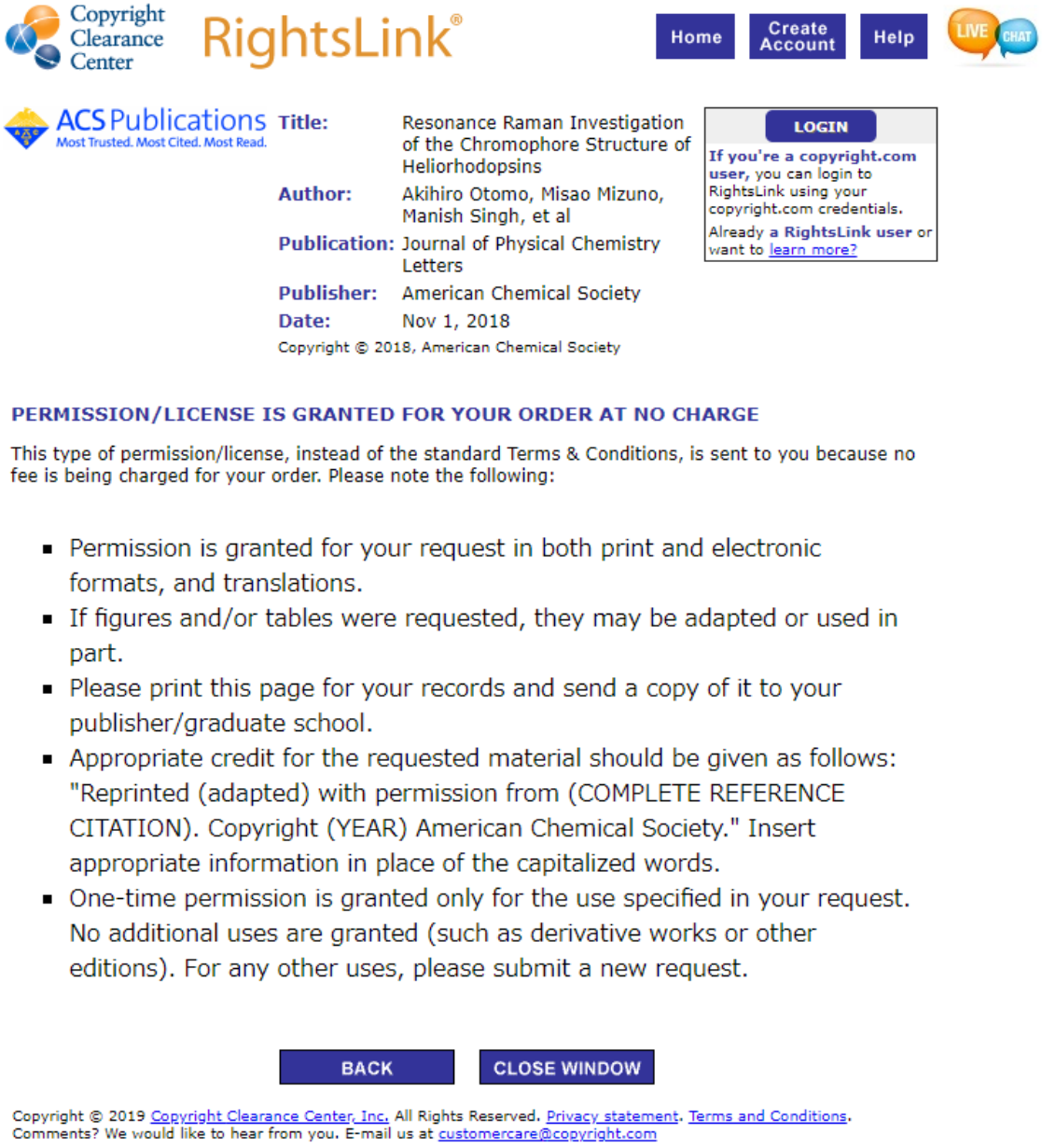

Copyright Clearance Center RightsLink®

Home | Create Account | Help | LIVE CHAT

ACS Publications
Most Trusted. Most Cited. Most Read.

Title:	Resonance Raman Investigation of the Chromophore Structure of Heliorhodopsins
Author:	Akihiro Otomo, Misao Mizuno, Manish Singh, et al
Publication:	Journal of Physical Chemistry Letters
Publisher:	American Chemical Society
Date:	Nov 1, 2018

Copyright © 2018, American Chemical Society

LOGIN

If you're a copyright.com user, you can login to RightsLink using your copyright.com credentials.

Already a RightsLink user or want to learn more?

PERMISSION/LICENSE IS GRANTED FOR YOUR ORDER AT NO CHARGE

This type of permission/license, instead of the standard Terms & Conditions, is sent to you because no fee is being charged for your order. Please note the following:

- Permission is granted for your request in both print and electronic formats, and translations.
- If figures and/or tables were requested, they may be adapted or used in part.
- Please print this page for your records and send a copy of it to your publisher/graduate school.
- Appropriate credit for the requested material should be given as follows: "Reprinted (adapted) with permission from (COMPLETE REFERENCE CITATION). Copyright (YEAR) American Chemical Society." Insert appropriate information in place of the capitalized words.
- One-time permission is granted only for the use specified in your request. No additional uses are granted (such as derivative works or other editions). For any other uses, please submit a new request.

BACK | CLOSE WINDOW

Copyright © 2019 Copyright Clearance Center, Inc. All Rights Reserved. Privacy statement. Terms and Conditions.
Comments? We would like to hear from you. E-mail us at customercare@copyright.com

5.8. References

[1] Spudich, J. L., Yang, C. S., Jung, K. H., and Spudich, E. N. (2000) Retinylidene Proteins: Structures and Functions from Archaea to Humans, *Annu. Rev. Cell Dev. Biol. 16*, 365-392.

[2] Pushkarev, A., Inoue, K., Larom, S., Flores-Uribe, J., Singh, M., Konno, M., Tomida, S., Ito, S., Nakamura, R., Tsunoda, S. P., Philosof, A., Sharon, I., Yutin, N., Koonin, E. V., Kandori, H., and Beja, O. (2018) A Distinct Abundant Group of Microbial Rhodopsins Discovered Using Functional Metagenomics, *Nature 558*, 595-599.

[3] Tahara, S., Singh, M., Kuramochi, H., Shihoya, W., Inoue, K., Nureki, O., Béjà, O., Mizutani, Y., Kandori, H., and Tahara, T. (2019) Ultrafast Dynamics of Heliorhodopsins, *J. Phys. Chem. B 123*, 2507-2512.

[4] Engelhard, C., Chizhov, I., Siebert, F., and Engelhard, M. (2018) Microbial Halorhodopsins: Light-Driven Chloride Pumps, *Chem. Rev.*, in press.

[5] Kandori, H., Inoue, K., and Tsunoda, S. P. (2018) Light-Driven Sodium-Pumping Rhodopsin: A New Concept of Active Transport, *Chem. Rev.*, in press.

[6] Lanyi, J. K. (2004) Bacteriorhodopsin, *Annu. Rev. Physiol. 66*, 665-688.

[7] Schneider, F., Grimm, C., and Hegemann, P. (2015) Biophysics of Channelrhodopsin, *Annu. Rev. Biophys. 44*, 167-186.

[8] Spudich, J. L., and Luecke, H. (2002) Sensory Rhodopsin II: Functional Insights from Structure, *Curr. Opin. Struct. Biol. 12*, 540-546.

[9] Wouter D. Hoff, Jung, K.-H., and Spudich, J. L. (1997) Molecular Mechanism of Photosignaling by Archaeal Sensory Rhodopsins, *Annu. Rev. Biophys. Biomol. Struct. 26*, 223-258.

[10] Luck, M., Mathes, T., Bruun, S., Fudim, R., Hagedorn, R., Nguyen, T. M. T., Kateriya, S., Kennis, J. T. M., Hildebrandt, P., and Hegemann, P. (2012) A Photochromic Histidine Kinase Rhodopsin (HKR1) that is Bimodally Switched by UV and Blue Light, *J. Biol. Chem. 287*, 40083-40090.

[11] Scheib, U., Stehfest, K., Gee, C. E., Körschen, H. G., Fudim, R., Oertner, T. G., and Hegemann, P. (2015) The Rhodopsin–Guanylyl Cyclase of the Aquatic Fungus *Blastocladiella emersonii* Enables Fast Optical Control of cGMP Signaling, *Sci. Signal. 8*, rs8-rs8.

[12] Yoshida, K., Tsunoda, S. P., Brown, L. S., and Kandori, H. (2017) A Unique Choanoflagellate Enzyme Rhodopsin with Cyclic Nucleotide Phosphodiesterase Activity, *J. Biol. Chem. 292*, 7531-7541.

[13] Singh, M., Inoue, K., Pushkarev, A., Béjà, O., and Kandori, H. (2018) Mutation Study of Heliorhodopsin 48C12, *Biochemistry 57*, 5041-5049.

[14] Smith, S. O., Braiman, M. S., Myers, A. B., Pardoen, J. A., Courtin, J. M. L., Winkel, C., Lugtenburg, J., and Mathies, R. A. (1987) Vibrational Analysis of the All-T*rans*-Retinal Chromophore in Light-Adapted Bacteriorhodopsin, *J. Am. Chem. Soc. 109*, 3108-3125.

[15] Baasov, T., Friedman, N., and Sheves, M. (1987) Factors Affecting the C=N Stretching in Protonated Retinal Schiff Base: A Model Study for Bacteriorhodopsin and Visual Pigments, *Biochemistry 26*, 3210-3217.

[16] Kralj, J. M., Spudich, E. N., Spudich, J. L., and Rothschild, K. J. (2008) Raman Spectroscopy Reveals Direct Chromophore Interactions in the Leu/Gln105 Spectral Tuning Switch of Proteorhodopsins, *J. Phys. Chem. B 112*, 11770-11776.

[17] Saint Clair, E. C., Ogren, J. I., Mamaev, S., Russano, D., Kralj, J. M., and Rothschild, K. J. (2012) Near-IR Resonance Raman Spectroscopy of Archaerhodopsin 3: Effects of Transmembrane Potential, *J. Phys. Chem. B 116*, 14592-14601.

[18] Alshuth, T., Stockburger, M., Hegemann, P., and Oesterhelt, D. (1985) Structure of the Retinal Chromophore in Halorhodopsin, *FEBS Lett. 179*, 55-59.

[19] Maeda, A., Ogurusu, T., Yoshizawa, T., and Kitagawa, T. (1985) Resonance Raman Study on Binding of Chloride to the Chromophore of Halorhodopsin, *Biochemistry 24*, 2517-2521.

[20] Diller, R., Stockburger, M., Oesterhelt, D., and Tittor, J. (1987) Resonance Raman Study of Intermediates of the Halorhodopsin Photocycle, *FEBS Lett. 217*, 297-304.

[21] Gerscher, S., Mylrajan, M., Hildebrandt, P., Baron, M.-H., Müller, R., and Engelhard, M. (1997) Chromophore−Anion Interactions in Halorhodopsin from *Natronobacterium pharaonis* Probed by Time-Resolved Resonance Raman Spectroscopy, *Biochemistry 36*, 11012-11020.

[22] Mizuno, M., Nakajima, A., Kandori, H., and Mizutani, Y. (2018) Structural Evolution of a Retinal Chromophore in the Photocycle of Halorhodopsin from *Natronobacterium pharaonis*, *J. Phys. Chem. A 122*, 2411-2423.

[23] Mironova, O. S., Efremov, R. G., Person, B., Heberle, J., Budyak, I. L., Buldt, G., and Schlesinger, R. (2005) Functional Characterization of Sensory Rhodopsin II from *Halobacterium salinarum* Expressed in *Escherichia coli*, *FEBS Lett. 579*, 3147-3151.

[24] Gellini, C., Lüttenberg, B., Sydor, J., Engelhard, M., and Hildebrandt, P. (2000) Resonance Raman Spectroscopy of Sensory Rhodopsin II from *Natronobacterium pharaonis*, *FEBS Lett. 472*, 263-266.

[25] Tateishi, Y., Abe, T., Tamogami, J., Nakao, Y., Kikukawa, T., Kamo, N., and Unno, M. (2011) Spectroscopic Evidence for the Formation of an N Intermediate During the Photocycle of Sensory Rhodopsin II (Phoborhodopsin) from *Natronobacterium pharaonis*, *Biochemistry 50*, 2135-2143.

[26] Hildebrandt, P., and Stockburger, M. (1984) Role of Water in Bacteriorhodopsin's Chromophore: Resonance Raman Study, *Biochemistry 23*, 5539-5548.

[27] Smith, S. O., Myers, A. B., Pardoen, J. A., Winkel, C., Mulder, P. P. J., Lugtenburg, J., and Mathies, R. (1984) Determination of Retinal Schiff Base Configuration in Bacteriorhodopsin, *Proc. Natl. Acad. Sci. U. S. A. 81*, 2055-2059.

[28] Mathies, R. A., Smith, S. O., and Palings, I. (1988) Determination of Retinal Chromophore Structure in Rhodopsins, In *Biological Application of Raman Spectroscopy* (Spiro, T. G., Ed.), pp 59-108, John Wiley and Sons, New York.

[29] Aton, B., Doukas, A. G., Callender, R. H., Becher, B., and Ebrey, T. G. (1977) Resonance Raman Studies of the Purple Membrane, *Biochemistry 16*, 2995-2999.

[30] Kajimoto, K., Kikukawa, T., Nakashima, H., Yamaryo, H., Saito, Y., Fujisawa, T., Demura, M., and Unno, M. (2017) Transient Resonance Raman Spectroscopy of a Light-Driven Sodium-Ion-Pump Rhodopsin from *Indibacter alkaliphilus*, *J. Phys. Chem. B 121*, 4431-4437.

[31] Shionoya, T., Mizuno, M., Tsukamoto, T., Ikeda, K., Seki, H., Kojima, K., Shibata, M., Kawamura, I., Sudo, Y., and Mizutani, Y. (2018) High Thermal Stability of Oligomeric Assemblies of Thermophilic Rhodopsin in a Lipid Environment, *J. Phys. Chem. B 122*, 6945-6953.

[32] Niho, A., Yoshizawa, S., Tsukamoto, T., Kurihara, M., Tahara, S., Nakajima, Y., Mizuno, M., Kuramochi, H., Tahara, T., Mizutani, Y., and Sudo, Y. (2017) Demonstration of a Light-Driven SO_4^{2-} Transporter and Its Spectroscopic Characteristics, *J. Am. Chem. Soc. 139*, 4376-4389.

[33] Krebs, R. A., Dunmire, D., Partha, R., and Braiman, M. S. (2003) Resonance Raman Characterization of Proteorhodopsin's Chromophore Environment, *J. Phys. Chem. B 107*, 7877-7883.

[34] Smith, S. O., Lugtenburg, J., and Mathies, R. A. (1985) Determination of Retinal Chromophore Structure in Bacteriorhodopsin with Resonance Raman Spectroscopy, *J. Membr. Biol. 85*, 95-109.

[35] Fodor, S. P., Gebhard, R., Lugtenburg, J., Bogomolni, R. A., and Mathies, R. A. (1989) Structure of the Retinal Chromophore in Sensory Rhodopsin I from Resonance Raman Spectroscopy, *J. Biol. Chem. 264*, 18280-18283.

[36] Inagaki, F., Tasumi, M., and Miyazawa, T. (1975) Vibrational Analysis of Polyene Chains. Assignments of the Resonance Raman Lines of Poly (Acetylene) and β-Carotene, *J. Raman Spectrosc. 3*, 335-343.

[37] Saito, S., and Tasumi, M. (1983) Normal-Coordinate Analysis of β-Carotene Isomers and Assignments of the Raman and Infrared Bands, *J. Raman Spectrosc. 14*, 310-321.

[38] Smith, S. O., Pardoen, J. A., Lugtenburg, J., and Mathies, R. A. (1987) Vibrational Analysis of the 13-*Cis*-Retinal Chromophore in Dark-Adapted Bacteriorhodopsin, *J. Phys. Chem. 91*, 804-819.

[39] Eyring, G., Curry, B., Broek, A., Lugtenburg, J., and Mathies, R. (1982) Assignment and Interpretation of Hydrogen Out-of-plane Vibrations in the Resonance Raman Spectra of Rhodopsin and Bathorhodopsin, *Biochemistry 21*, 384-393.

CONCLUSION

In this doctoral thesis, we aimed to elucidate the structural and functional relationship in the abundant photoreceptor protein, rhodopsins. Rhodopsin is classified into three types; microbial rhodopsin, animal rhodopsin, and heliorhodopsin (HeR), which was discovered recently. All of them share a heptahelical transmembrane architecture embedded into the cell membrane and possess a retinal molecule as a chromophore. All rhodopsins function by changing the protein structure driven by the photoisomerization of the retinal chromophore although the functions vary for different types of rhodopsins. This raises questions about how a similar protein structural motif and a common trigger of photoisomerization could generate diverse functions. To address this question, we used resonance Raman (RR) spectroscopy, which enables us to observe selectively enhanced vibrational mode in proteins. Through this thesis, we elucidated the structural factor which determines the function of KR2 (Chapter 3), the mechanism of sodium ion transport in KR2 (Chapter 4), and prediction of the function in HeRs (Chapter 5).

In Chapter 1, the basic structural and functional properties of rhodopsins and principles of Raman spectroscopy were explained. There, we described the reason why we selected KR2 and HeRs as target proteins. In addition to the spectroscopic experiments, we conducted many biochemical techniques to elucidate the structure-function relationship of the rhodopsins. The methodologies were explained in Chapter 2.

Chapter 3 aims to investigate the cation concentration dependence on the retinal structure in KR2. Since KR2 shows a functional conversion in response to co-existing cation species, it is a good model to investigate how rhodopsin determine its function. Our spectral data clearly demonstrated that not only sodium ion but also potassium ion can bind to KR2 and the ion binding induces the structural changes around the retinal chromophore. The ion binding site locates at the subunit interface far from the retinal chromophore, indicating that the long-distance

conformational change occurs by binding an ion. We found that only when sodium ion binds to KR2, this conformational change weakens the hydrogen bond strength of the protonated Schiff base, which plays an important role in the ion transport. Furthermore, we also showed that the oligomeric stability of KR2 significantly decreases at low cation concentration when KR2 is solubilized with DDM whereas it is not affected when nanodisc-reconstituted KR2. These results suggest that it should be paid attention when the membrane protein is solubilized with detergents.

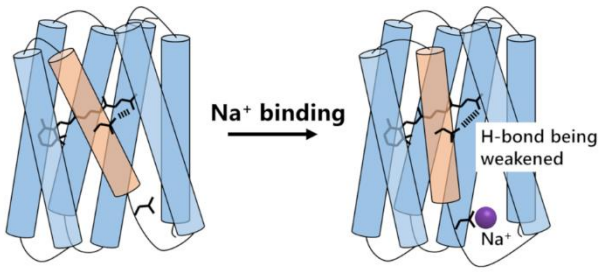

Figure 1. Proposed mechanism for the conformational change between the ion binding site and the retinal Schiff base.

The structural change during sodium ion transport in KR2 was elucidated using time-resolved UVRR spectroscopy, as shown in Chapter 4. We demonstrated that the hydrophobic interaction of Trp residues decreases and the orientation of Tyr residues change in the O intermediate, where sodium ion passes through proteins. By using W215F and Y222F mutants, we could extract the spectral components in the difference spectra seen in WT KR2. They are located in the same helix (helix F) so that the tilting or rotating of helix F induces the transient channel formation, which is required for sodium ion transport. Since the aromatic amino acid residues such as Trp215 and Tyr222 are well conserved among rhodopsins, this movement of helix F is probably a common feature for rhodopsin functions. This study demonstrated the usefulness of the time-resolved UVRR spectroscopy to elucidate the structural change during ion transport in rhodopsins. It should be pointed out that there are few examples of applying time-resolved UVRR spectroscopy to light-induced ion pump rhodopsin. I hope this technique will be

widely used to elucidate the functional mechanism of rhodopsins at the molecular level.

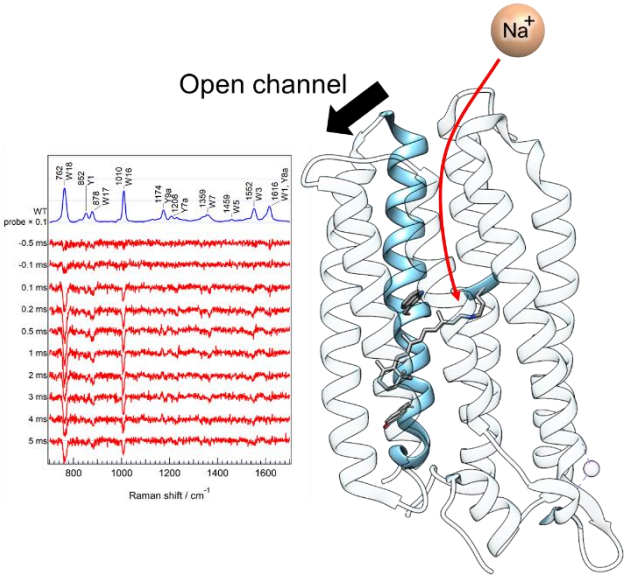

Figure 2. Proposed mechanism for opening the channel by movement of the helix F.

In Chapter 5, the study of HeRs is described. The proteins are discovered very recently and their structure and function are unknown. We characterized the RR spectra of HeRs from two distinct living organisms. Our results demonstrate that the protonated Schiff base likely forms a strong hydrogen bond with not a water molecule but a counterion residue. A unique vibrational coupling between the ν(C=C) and δ(N-H) modes was observed, indicating the Schiff base geometry differs from those of type-1 rhodopsins. On the basis of these spectral features, we proposed that HeRs function as a photosensor. Our hypothesis of protein function from elucidating the molecular structure was of significance.

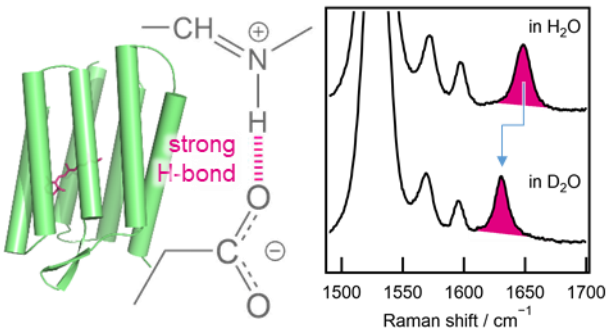

Figure 3. Retinal chromophore structure and its environment of HeRs.

As highlighted above, we tried to elucidate the structure of the retinal chromophore and the protein moiety of rhodopsins using resonance Raman spectroscopy and led it to the functional elucidation. Rhodopsins are attracting attention as a tool for optogenetics as well as the utilization of light energy by living organisms. I believe that this thesis, which has elucidated the detailed protein structure at a molecular level, will greatly contribute to the study of rhodopsins that will be further advanced in the future.

LIST OF PUBLICATIONS

Doctoral Dissertations

A. Otomo, M. Mizuno, K. Inoue, H. Kandori, and Y. Mizutani*

"Allosteric Communication to the Retinal Chromophore upon Ion Binding in a Light-driven Sodium Pumping Rhodopsin"

Biochemistry, American Chemical Society, Under revision.

A. Otomo, M. Mizuno, M. Singh, W. Shihoya, K. Inoue, O. Nureki, O. Béjà, H. Kandori, and Y. Mizutani*

"Resonance Raman Investigation of the Chromophore Structure of Heliorhodopsins"

J. Phys. Chem. Lett., American Chemical Society, **2018**, 9, 6431-6436.

Reference Paper

A. Otomo, H. Ishikawa, M. Mizuno, T. Kimura, M. Kubo, Y. Shiro, S. Aono, and Y. Mizutani*

"A study of the Dynamics of the Heme Pocket and C-helix in CooA upon CO Dissociation Using Time-Resolved Visible and UV Resonance Raman Spectroscopy"

J. Phys. Chem. B, American Chemical Society, **2016**, 120, 7836-7843.

ACKNOWLEDGMENT

I would like to show my greatest appreciation to Prof. Yasuhisa Mizutani for his valuable suggestions, directions, criticism, and encouragement. Without his guidance, this research would not have materialized. The interest and severity of the research he taught me will greatly affect my future life as a researcher.

I owe my deepest gratitude to Associate professor Haruto Ishikawa and Assistant professor Misao Mizuno for their fruitful discussions, constructive comments, and warm encouragement. I would also like to acknowledge all colleagues in Biophysical Chemistry laboratory. In particular, I am indebted to Dr. Shinya Tahara for his helpful discussion and advises about kinetics analysis.

It should be emphasized that a lot of experiments done in this work have required the cooperation of the collaborators. Prof. Hideki Kandori (Graduate School of Engineering, Nagoya Institute of Technology) and Associate professor Keiichi Inoue (The Institute for Solid State Physics, The Univ. of Tokyo) always give me insightful comments and important suggestions. Discussion with them was always exciting and fun. I gratefully thank Dr. Rei Abe-Yoshizumi and Dr. Manish Singh (Graduate School of Engineering, Nagoya Institute of Technology) for providing the samples and generous support about the characterization of each sample.

This work was supported by Grant-in-Aid for JSPS Research Fellow for Young Scientists to A. O. (19J10830).

Big Love & Special Thanks to my family, friends, and everyone who supported me.

August 2019

Akihiro OTOMO